Modeling and Simulation of Microelectromechanical Systems in Multi-Physics Fields

Mohammad I. Younis

Dissertation submitted to the Faculty of the
Virginia Polytechnic Institute and State University
in partial fulfillment of the requirements for the degree of

Doctor of Philosophy
in
Engineering Mechanics

Ali H. Nayfeh, Chairman
Saad A. Ragab
Scott L. Hendricks
Ziyad Masoud
Donald J. Leo

June 28, 2004
Blacksburg, Virginia

Keywords: MEMS, RF Switches, Resonators, Squeeze-Film Damping, Thermoelastic Damping, Electrostatic Actuation, Dynamic Pull-in, Microplates, Microbeams, Finite Element, Singular Perturbation, Primary and Secondary Excitations

Modeling and Simulation of Microelectromechanical Systems in Multi-Physics Fields

Mohammad I. Younis

(ABSTRACT)

The first objective of this dissertation is to present hybrid numerical-analytical approaches and reduced-order models to simulate microelectromechanical systems (MEMS) in multi-physics fields. These include electric actuation (AC and DC), squeeze-film damping, thermoelastic damping, and structural forces. The second objective is to investigate MEMS phenomena, such as squeeze-film damping and dynamic pull-in, and use the latter to design a novel RF-MEMS switch.

In the first part of the dissertation, we introduce a new approach to the modeling and simulation of flexible microstructures under the coupled effects of squeeze-film damping, electrostatic actuation, and mechanical forces. The new approach utilizes the compressible Reynolds equation coupled with the equation governing the plate deflection. The model accounts for the slip condition of the flow at very low pressures. Perturbation methods are used to derive an analytical expression for the pressure distribution in terms of the structural mode shapes. This expression is substituted into the plate equation, which is solved in turn using a finite-element method for the structural mode shapes, the pressure distributions, the natural frequencies, and the quality factors. We apply the new approach to a variety of rectangular and circular plates and present the final expressions for the pressure distributions and quality factors. We extend the approach to microplates actuated by large electrostatic forces. For this case, we present a low-order model, which reduces significantly the cost of simulation. The model utilizes the nonlinear Euler-Bernoulli beam equation, the von Kármán plate equations, and the compressible Reynolds equation.

The second topic of the dissertation is thermoelastic damping. We present a model and analytical expressions for thermoelastic damping in microplates. We solve the heat equation for the thermal flux across the microplate, in terms of the structural mode

shapes, and hence decouple the thermal equation from the plate equation. We utilize a perturbation method to derive an analytical expression for the quality factor of a microplate with general boundary conditions under electrostatic loading and residual stresses in terms of its structural mode shapes. We present results for microplates with various boundary conditions.

In the final part of the dissertation, we present a dynamic analysis and simulation of MEMS resonators and novel RF MEMS switches employing resonant microbeams. We first study microbeams excited near their fundamental natural frequencies (primary-resonance excitation). We investigate the dynamic pull-in instability and formulate safety criteria for the design of MEMS sensors and RF filters. We also utilize this phenomenon to design a low-voltage RF MEMS switch actuated with a combined DC and AC loading. Then, we simulate the dynamics of microbeams excited near half their fundamental natural frequencies (superharmonic excitation) and twice their fundamental natural frequencies (subharmonic excitation). For the superharmonic case, we present results showing the effect of varying the DC bias, the damping, and the AC excitation amplitude on the frequency-response curves. For the subharmonic case, we show that if the magnitude of the AC forcing exceeds the threshold activating the subharmonic resonance, all frequency-response curves will reach pull-in.

Dedication

To my wife Ola and our sons Ibrahim and Muhmoud

Acknowledgments

I would like to take this chance to express my deep thanks and appreciation to my advisor Professor Ali Nayfeh, who supported me greatly and did every possible effort to help and teach me during my MS and PhD education. I am more than thankful for him for his kindness, patience, and endless encouragement. He supported me in every possible way to advance my academic skills to the highest levels. I learned from his great personality many important lessons and values that are in themselves another valuable degree. He showed me an example of how a successful person should be and behave. Indeed, he has been the distinguished teacher, the merciful father, and a great person I was blessed to know. I have been pleased to know him and enjoyed greatly his friendship and companion.

I would like to thank my committee members, Dr. Saad Ragab, Dr. Scott Hendricks, Dr. Ziyad Masoud, and Dr. Donald Leo, for their support and friendship. In particular, I would like to thank Dr. Saad Ragab for his significant help while conducting my research and Dr. Scott Hendricks for his vital support during my MS and PhD study. Both professors are very distinguished teachers and I am greatly thankful to them for educating me the best of education. Many thanks go to Dr. Marwan Khraisheh for encouraging and helping me to get acceptance at Virginia Tech. Without his help, I would not be here. Words of thank go to Dr. Suhil Kiwan and Dr. Mohammad Alkam for their belief in me and for encouraging me to continue my education.

I would like to thank the nice friends from "The Strange Attractor Group" in the Nonlinear Dynamics Lab, whom I was pleased to meet and know. Particularly,

thanks go to Dr. Osama Ashour, Dr. Waleed Faris, Dr. Samir Emam, Dr. Khalid Alahaza, Dr. Pramod Malatkar, Mr. Mohammad Daqaq, Mr. Nader Nayfeh, Mr. Amjed Al-Mousa, Mr. Imran Akhtar, Mr. Konda Cheva, Mr. Gregory Vogl, and Mr. Xiaopeng Zhao. Special thanks go to Dr. Haider Arafat for his significant support during my study and for helping me to understand many unclear points in nonlinear dynamics and perturbations. Also, I specially thank Dr. Eihab Abdel-Rahman, who collaborated with me in parts of this dissertation and who helped me in my research in MEMS. I would like also to thank Mrs. Sally Sharder for her kindness and for organizing the group matters. Many thanks go to my dearest friends Rami Abo Al-Nasser, Mohammad Sha'aban, and Mohammad Abo Zakyah for their support and friendship.

I would like to express my sincere gratitude and deep appreciation to my parents for believing in me and for believing that I deserve a better education. Their patience, sacrifice, and prayers for me to succeed are highly appreciated. Indeed, they were my major source of strength and support. Many thanks also go to my beloved sister Rana and my brother Hani for their ultimate support and encouragement. Finally, I would like to deeply thank my wife Ola for her support, patience, sacrifice, and belief in me. She is the one who paid the greatest sacrifice to make me succeed. Without her continuous help and support, I would not have succeeded and reached where I am now. I am forever grateful for her support and love.

Contents

List of Figures

List of Tables

Chapter 1

Introduction

1.1 Background and Motivation

Recently, the emerging technology of microelectromechanical systems (MEMS) has seen dramatic progress in fabricating and testing new devices, creating innovative applications, and proposing novel technologies. The fact that they can be manufactured using existing manufacturing techniques and infrastructure of the semiconductor industry means that they can be produced at low cost and in large volumes, making their commercialization quite attractive. Their light weight, small size, low-energy consumption, and durability make them even more attractive. There are numerous MEMS devices that have been successfully used in diverse areas of engineering and science. Ink jet printer heads, micropumps, projection display arrays, and airbag acceloremeters are just few examples, where MEMS devices have replaced more conventional devices in their class for fractions of the cost. Currently, MEMS devices are being actively developed for a wide spectrum of applications in various aspects of life (Elwenspoek and Wiegerink, 2001). In medical applications, for example, MEMS are being implemented for hearing and seeing aids, dosage and draining systems, and nerves stimulation. In information technology, MEMS paved the way for brilliant possibilities, such as increasing significantly the information storage and realizing CD-players in the size of a coin.

Unfortunately, simulation tools of MEMS have not kept up pace with this growth

of technology (Senturia et al., 1997). MEMS devices are still being designed by trial and error. A main reason is the fact that the design process of a MEMS device is a multidisciplinary task, which involves inherent coupled-energy domains, such as fluidic, electrostatic, thermal, and mechanical forces. Hence, simulating a MEMS device requires the use of at least two CAD solvers interacting with each other in an iterative manner (Gillbert et al., 1995; Reuther et al., 1996), which is computationally cumbersome. Therfore, these tools are used to simulate the performance of finished devices, rather than to assist their design in preliminary stages of production. Consequently, there are increasing demands toward reducing the complexity of simulations and developing more efficient CAD tools (Senturia et al., 1997; Wachutka, 2002), which can play an effective rule in the development of this technology and realizing reliable devices of optimal performance with minimal cost.

RF MEMS is another fast-growing area that promises breakthrough advances in telecomunications, radar systems, and personal mobiles. RF MEMS refers to (Varadan et al., 2003; Tilmans et al., 2003) the application of MEMS technology to high-frequency circuits (radio frequency (RF), microwave, or millimeter wave). Beside the well-known advantages of microtechnology, RF MEMS offer many attractive features over other conventional RF devices. These include increasing bandwidth, high-frequency operating range, and low-insertion loss. RF MEMS consist of passive components, such as transmission lines and couplers, and active components, such as variable capacitors, tuners, switches, and filters. The interest of this dissertation lies in the second category, namely switches and filters (resonators).

Mechanical resonators have been widely used as transducers in mechanical microsensors since the mid eighties (Elwenspoek and Wiegerink, 2001). As the area of RF MEMS exploded remarkably and the demand for filters with high resonance frequency and quality factor increased rapidly, microelectromechanical resonators were proposed in the mid nineties (Varadan et al., 2003; Tilmans et al., 2003) as a feasible alternative to comb-drive filters and other conventional large-size filters (Clark et al., 1997).

There are a number of actuation methods that can be used to excite resonators,

such as thermal, piezoelectric, electromagnetic, and electrostatic mechanisms. Electrostatic actuation is the most preferable and well-established actuation method in MEMS because of its simplicity and high efficiency (Varadan et al., 2003). In RF filters, a microbeam is deflected by a DC bias and then driven to vibrate by an AC harmonic load. The frequency of the AC force can be tuned near the fundamental natural frequency of the microbeam, in which case the actuation is called primary-resonance excitation. Alternatively, the microbeam can be excited at other frequencies, such as near half the fundamental natural frequency (superharmonic excitation) or twice the fundamental natural frequency (subharmonic excitation). Recent research (Jin and Wang, 1998) has shown experimentally that using a superharmonic excitation for resonant sensors increases the signal-to-crosstalk ratio compared to that of a primary-resonance excitation. In this dissertation, we simulate the behavior of microbeams actuated by any of the above methods of excitation.

RF MEMS switches are a fast-growing area that gained a great deal of attention in recent years. RF MEMS switches overcome the limitations of conventional switches, such as solid-state switches, and present many attractive features, like low-power consumption, high isolation, and low-insertion loss. Similar to resonators, RF switches rely on a mechanical element, which is actuated typically by DC electrostatic forces, to close or break an electric circuit. Major drawback of these devices are the requirement of high driving voltages and the relatively slow response (Varadan et al., 2003; Tilmans et al., 2003). It is highly desirable to bring the actuation voltage to a level compatible or close to that of the circuit devices and to actuate the switch with a very high speed. However, the state-of-the-art of RF MEMS switches is far from achieving these requirements, which forms a barrier towards the development of this technology.

1.2 Common Phenomena in MEMS

In this section, we present a brief introduction to common phenomena in MEMS, which are found nearly in the majority of MEMS devices. Therefore, a thorough understanding of these phenomena is vital for achieving superior design of MEMS

devices. These phenomena form the core topic of this dissertation.

1.2.1 Squeeze-Film Damping

Typical MEMS devices employ a parallel-plate capacitor, in which one plate is actuated electrically and its motion is detected by capacitive changes. In order to increase the efficiency of actuation and improve the sensitivity of detection, the distance between the capacitor plates is minimized and the area of the electrode is maximized. Under such conditions, the so-called squeeze-film damping (Senturia, 2000; Nayfeh and Younis, 2004) is pronounced. This phenomenon occurs as a result of the massive movement of the fluid underneath the plate, which is resisted by the viscosity of the fluid. This gives rise to a pressure distribution underneath the plate, which may act as a spring and/or a damping force. Recent studies showed that the damping force dominates the spring force at low frequencies, whereas the spring force dominates the damping force at high frequencies.

1.2.2 Thermoelastic Damping

Thermoelastic damping has been shown recently to be a possible dominant source of intrinsic damping in MEMS. Thermoelastic damping results from the irreversible heat flow generated by the compression and decompression of an oscillating structure. A structure in bending has one side under tension and the other side under compression at a higher temperature. This variation in temperature causes a thermal gradient inside the material of the structure, which adjusts itself to allow for a thermal equilibrium. However, the energy used in this adjustment cannot be restored (irreversible process) even if the structure returns to its original state of zero-bending stress. Hence, thermoelastic damping is also referred to as internal friction. According to (Randall et al., 1939), internal friction is defined as "the capacity of a solid to transform its ordered energy of vibration into disordered internal energy".

1.2.3 Pull-In Instability

The electric load acting on a capacitor plate is composed of a DC polarization voltage and an AC voltage. The DC component applies an electrostatic force on the plate, thereby deflecting it to a new equilibrium position, while the AC component vibrates the plate around this equilibrium position. The combined electric load has an upper limit beyond which the mechanical restoring force of the plate can no longer resist its opposing force, thereby leading to a continuous increase in the microstructure deflection and, accordingly, an increase in the electric forces in a positive feedback loop. This behavior continues until a physical contact is made with the stationary electrode. This structural instability phenomenon is known as 'pull-in,' (Senturia, 2000) and the critical voltage associated with it is called 'pull-in voltage.'

A key issue in the design of MEMS resonators is to tune the electric load away from the pull-in instability, which leads to collapse of the structure, and hence a failure in the device. On the other hand, this phenomenon forms the basis of operation for RF MEMS switches, in which the mechanical structure is actuated by a voltage load beyond the pull-in voltage to snap the structure with the fastest speed and minimal time.

1.3 Literature Review

In this section, we summarize the main contributions to model and simulate electrically actuated microstructures in the prepense of any of the three basic phenomena of MEMS of Section 1.2. We also discuss the literature work and address the need to improve and extend the state-of-the-art of MEMS modeling and simulation.

1.3.1 Squeeze-Film Damping

There has been extensive research into the behavior of a microplate moving very close to another surface under the effect of squeeze-film damping. Next, we summarize the main contributions.

We begin by summarizing papers, which addressed the need to account for squeeze-

film damping in the modeling of MEMS devices. Newell (1968) studied the effect of damping on miniaturizing cantilever resonators. He divided the pressure range from vacuum to atmospheric pressure into three regimes. In the first regime, the pressure is low (near vacuum) and the damping is dominated by intrinsic damping. In the second regime, the pressure is higher and air damping is dominant, which is due to momentum transfer during collision of the molecules with the moving structure. In this regime, Newell applied the Christian (1966) model, derived by studying the effect of a moving rigid body on changing the linear momentum of the gas molecules. In the third regime, the pressure is high (near atmospheric) and viscous damping is dominant and independent of pressure. In this regime, Newell derived an expression for damping based on the drop in the pressure in a viscous fluid flowing through a parallel-walled duct.

Zook et al. (1992) conducted experiments to measure the quality factors of electrostatic clamped-clamped microbeams encapsulated at low pressure. They calculated the quality factors using both the Christian (1966) model in the molecular regime and the Newell (1968) model in the viscous drag regime. Comparing the calculated quality factors with experimental data, they found large discrepancy. Seidel et al. (1990) designed and modeled a capacitive parallel-plate microaccelerometer using a harmonic oscillator with constant damping coefficient. They found that the theoretically predicted frequency-response curves deviate from those obtained experimentally. They also reported an increase in the resonance frequency with increasing residual pressure in the airgap.

Legtenberg and Tilmans (1994) and Gui et al. (1995) conducted experiments to measure the quality factors of electrostatic clamped-clamped microresonators encapsulated at very low pressure. They calculated the quality factors of the resonators based on the kinetic theory of gases in the molecular regime (Gupta, 1990). They found that the theory overestimates the measured quality factors by more than two orders of magnitude. They attributed the discrepancy to the fact that the theory does not account for the presence of another electrode, which is very close to the resonator.

Next, we summarize contributions, which modeled squeeze-film damping effects in

MEMS devices employing rigid plates. We begin with Starr (1990) who modeled a capacitive parallel-plate accelerometer using a linearized Reynolds equation. He assumed incompressible fluid, thereby neglecting the spring effect. This assumption reduces the Reynolds equation to the Possion equation, which can be solved either analytically for simple shapes or numerically (e.g., finite-element packages) for complicated shapes. As an example, Starr used the finite-element package ANSYS to calculate the pressure distribution underneath a plate with a hole. He also derived an exact expression for the damping force of a circular disk and an approximate expression for the damping force of a rectangular plate. Chu et al. (1996) modeled the dynamic behavior of parallel-plate electrostatic actuators using a lumped spring-mass model. They used the expressions of Starr (1990), modified by replacing the initial airgap width by the variable distance between the plates. They compared the theoretical frequency-response curve of a plate to experimental data and found that the simulated maximum amplitude is approximately ten times the measured amplitude.

The next group of researchers treated the squeeze-film damping problem using the linearized compressible Reynolds equation. Blech (1983) solved analytically the linearized Reynolds equation in the case of oscillating rigid plates of rectangular and circular shapes with trivial pressure boundary conditions and derived analytical expressions for the spring and damping forces. Andrews et al. (1993) conducted experiments on parallel-plate electrostatic microstructures and simulated their dynamic behavior with a spring-mass-damper model. The spring constant was composed of a structural component extracted from the measured resonance frequency at vacuum and a pressure component calculated from the Blech (1983) model. The damping constant was also calculated from the Blech model. They used curve fitting to extract a value for the airgap width. However, they could not obtain a single value for the width that leads to good agreement with the experimental measurements over the entire frequency range, the estimated gap width was 2.1 μm at low frequencies and 1.8 μm at high frequencies.

Veijola et al. (1995) investigated the behavior of a capacitive accelerometer, which employs a proof mass supported by a cantilever beam. They simulated its dynamic behavior with a spring-mass-damper model with a parallel-plate electrostatic force. The

damping coefficient was calculated using the Blech (1983) model and the spring constant was estimated by curve fitting the experimental measurements. They accounted for the slip-flow condition by using an effective viscosity coefficient. They compared their simulations with experimental data and found good agreement. Darling et al. (1998) overcame the limitation of the Blech (1983) model, which was derived only for trivial pressure boundary conditions, by solving the linearized compressible Reynolds equation for arbitrary venting conditions in the case of rigid plates. Their solution scheme is based on Green's function.

The next category of researchers used statistical thermodynamics (Gupta, 1990) to model energy dissipation. Kàdàr et al. (1996) and Li et al. (1999) modified the Christian model (Christian, 1966) by improving the distribution function of the velocity molecules to reflect more the physics of the problem. They compared their theoretical results to the theory and experimental data of Zook et al. (1992) and found that their theory reduces the discrepancy; however the discrepancy was still significant. Bao et al. (2002) used an energy-transfer model to study the effect of a moving structure on changing the kinetic energy of the gas molecules. They derived an equation for the quality factor, similar to that of Christian (1966), but modified by a correction factor, which is proportional to the gap width and the inverse of the plate length. They compared their theoretical results to the theoretical results and experimental data of Zook et al. (1992) and found that their theory improved the agreement with the experimental data; however there was still significant discrepancy.

Next, we summarize models for flexible microstructures. Yang et al. (1997) simulated the dynamic behavior of an electrostatic clamped-clamped microbeam. They used the finite-element package ABAQUS to extract the fundamental free mode shape of the microbeam. They fed this mode shape as a harmonic deflection in the linearized Reynolds equation, modified to account for the slip condition. Then they solved the Reynolds equation over time using finite-difference and Rung-Kutta integration codes. From the results, they extracted effective damping and spring coefficients to be used in a spring-mass-damper model. Then, they calculated the quality factors and the resonance frequencies of two microbeams and compared the results with experiments.

They found good agreement for the resonance frequencies. They improved the model by lowering the modal stiffness in the simulation to match the experimental data. For the quality factors, they found good agreement up to a pressure value of approximately 1 *mbar*; below this value, the model overestimated the quality factor.

Hung and Senturia (1999) developed a macromodel to simulate the dynamics of a clamped-clamped microbeam proposed as a pressure sensor. They used the Galerkin method to discretize the two coupled partial-differential equations: the Euler-beam equation with the electric and squeeze-film forces and the nonlinear Reynolds equation, modified to account for the slip condition. The global basis functions were extracted using data produced from a few runs of a fully meshed and slow finite-difference method. They indicated that the basis functions of the deflected beam are similar to the linear mode shapes of an undeflected microbeam. On the other hand, they noted that the pressure basis functions exhibit a higher spatial distribution towards the middle of the beam. They computed the time that an undeflected microbeam takes to reach pull-in (the pull-in time) using two models: the macromodel and a model that assumes a linear damping. The results of the two models were then compared to experimental data and results obtained from a full slow finite-difference simulation. The model based on linear damping gave poor results, whereas the macromodel gave results in good agreement with the finite-difference results and experimental data.

McCarthy et al. (2002) studied the dynamic behavior of an electrostatic cantilever microswitch. They used a finite-difference scheme to solve two coupled equations: the Euler-beam equation with electrostatic forcing and the compressible Reynolds equation, modified to account for the slip condition. They represented the pressure by the product of an assumed parabolic function along the beam width and an unknown function along the beam length, which is determined in the solution procedure. They integrated the Reynolds equation across the beam width to transform it to a one-dimensional equation. They simulated the transient behavior of the beam, compared it to the experimental results, and found good agreement.

From the aforementioned review, we note the lack of computationally efficient tools to simulate accurately the dynamic behavior of flexible microstructures in coupled-

energy fields. The majority of the models treat the microplate as a rigid structure. The few models that account for flexibility of the microstructures have two major shortcomings. First, they approximate the structural problem while solving the flow problem and vice versa, despite the fact that both problems are coupled. Second, they solve the two-dimensional Reynolds equation coupled with a one-dimensional beam equation, in which case the pressure variation across the beam width is neglected (no wrinkles are allowed across the beam). Therefore, these models might not capture accurately the dynamic characteristics of microstructures and might result in inaccurate predictions of the quality factors. Some models require many iterations between different energy-domain finite-element or finite-difference solvers, making the simulation process cumbersome and time consuming.

Further, no model has been presented, for this class of coupled problems, to calculate the plate mode shapes, their natural frequencies, and quality factors, while sweeping the DC voltages up to the pull-in instability. Such problems are of significant importance for many MEMS applications, such as MEMS-based projection displays and RF microswitches, in which a microstructure is electrostatically actuated beyond the pull-in instability under the effect of squeeze-film damping to diffract or reflect incident light in the case of displays (Senturia, 2000) or for connecting or breaking an electric circuit for the cases of microswitches (Varadan et al., 2003).

1.3.2 Thermoelastic Damping

The first to realize the importance of thermoelastic damping and analyze it rigorously is Zener (1937), who gave an analytical approximation for the quality factors of metallic beams due to thermoelastic damping. Roszhart (1990) showed experimentally that thermoelastic damping can limit the quality factors of devices in the micro scale. He used the Zener (1937) model to calculate the quality factors of solid-state resonators and found good agreement with the measurements. Other experimental works showing thermoelastic damping as a dominant source of energy loss in MEMS are also reported by (Evoy et al., 2000) (Duwel et al., 2003).

In a recent work, Lifshitz and Roukes (2000) solved exactly the problem of ther-

moelastic damping of beams and derived an analytical expression for the quality factors. They calculated the quality factors of various microbeams and found that their model yields results close to that of the Zener (1937) model.

Microplates have been increasingly tested and used in various MEMS application, such as micropumps and pressure sensors. While the models of Lifshitz and Roukes (2000) and Zener (1937) have been proven to yield quantitatively good results for microbeams, their ability to predict thermoelastic damping in microplates remains questionable. This is particularly important in cases, such as fully-clamped plates, where a beam model does not apply. Also the models of (Lifshitz and Roukes, 2000) and (Zener, 1937) cannot predict the quality factors of structural modes, which vary spatially across the plate width, and hence cannot be captured using a beam model.

1.3.3 The Pull-in Phenomenon and the Behavior of Electrically Actuated Microbeams

Many models have been presented to model the pull-in phenomenon and the static and dynamic behavior of electrically actuated microbeams. An extensive review of these models is summarized in (Younis, 2001). Here, we summarize the major contributions. Then, we review studies addressing the behavior of electrically actuated microbeams and the so-called dynamic pull-in, which is one of the foci of this dissertation.

Younis et al. (2002) and Abdel-Rahman et al. (2002) presented a nonlinear model of electrically actuated microbeams, accounting for electrostatic forcing of the air gap capacitor, the restoring force of the microbeam, mid-plane stretching, and an axial load applied to the microbeam. They solved numerically the boundary-value problem describing the static deflection of the microbeam under the DC electrostatic forces using a shooting method. Using a similar procedure, they solved numerically the eigenvalue problem describing the vibration of the microbeam around its statically deflected position for the natural frequencies and mode shapes. Their results show that failure to account for mid-plane stretching in the microbeam restoring force leads to an underestimation of the pull-in instability limit. The results also show that the ratio of the width of the air gap to the microbeam thickness can be tuned to extend

the domain of the linear relationship between the DC polarization voltage and the fundamental natural frequency.

Younis and Nayfeh (2003) expanded on the work of Younis et al. (2002) and Abdel-Rahman et al. (2002) by considering the microbeam response to a general electric load composed of both DC and AC components. They applied a perturbation method, the method of multiple scales, to the general equation of motion of the microbeam and its associated boundary conditions, and obtained an approximation of the response of the microbeam to a primary-resonance excitation. They derived equations that describe the nonlinear resonance frequency, the amplitudes of periodic solutions, and the stability of these solutions. Their results show that increasing the axial force improves the linear characteristics of the resonance frequency while increasing the mid-plane stretching has the reverse effect. Moreover, the DC electrostatic load was found to affect the qualitative and quantitative nature of the frequency-response curves, resulting in either a softening or a hardening behavior. Finally, they investigated the possibility of activating a three-to-one internal resonance between the first and second modes and found that this kind of nonlinear interaction cannot be activated.

Abdel-Rahman and Nayfeh (2003) investigated the response of electrically actuated microbeams to a superharmonic and subharmonic excitations. They used the method of multiple scales to obtain two first-order nonlinear ordinary-differential equations that describe the modulation of the amplitude and phase of the response and its stability. They presented typical frequency-response and force-response curves, exhibiting the coexistence of multivalued solutions. They found that the solution corresponding to a superharmonic excitation consists of three branches, which meet at two saddle-node bifurcation points. On the other hand, the solution corresponding to a subharmonic excitation consists of two branches meeting a branch of trivial solutions at two pitchfork bifurcation points. One of these bifurcation points is supercritical and the other is subcritical. The model of Abdel-Rahman and Nayfeh (2003) applies only for small AC forcing.

Younis et al. (2003) and Abdel-Rahman et al. (2003b) developed a reduced-order model to simulate the static and dynamic behaviors of electrically actuated microbeams

undergoing small or large motions. The model uses few linear undamped mode shapes of a straight microbeam as basis functions in a Galerkin procedure, and hence it reduces the complexity of the simulation and reduces significantly the computational time. Unlike the model of (Younis et al. 2002) and (Abdel-Rahman et al. 2002), the reduced-order model shows high robustness as the pull-in instability is approached. Hence, Younis et al. (2003) and Abdel-Rahman et al. (2003b) utilized the model to study the static behavior of the microbeam more rigorously. They showed that the pull-in voltage corresponds to a saddle-node bifurcation. They calculated the static deflection at each DC voltage and found two solution branches: the larger solution is unstable and the smaller one is stable. As the DC voltage increases, these branches get closer to each other, coalesce, and destroy each other in a saddle-node bifurcation, corresponding to the pull-in voltage. They found that the deflection at pull-in is approximately 57% of the capacitor airgap, which is significantly higher than reported using linear theories, which is $\approx 33\%$. Finally, they used the model to simulate the dynamic behavior of a MEMS switch and calculate its pull-in time.

While the model of (Younis et al. 2003) and (Abdel-Rahman et al. 2003b) allows for a better understanding of the pull-in instability, it is based on static analysis and does not account for the effect of the AC loading. This is particularly important in light of the fact that the behavior of these microelectromechanical systems is nonlinear (Younis et al., 2001; Gui et al., 1998). Therfore, the possibility of a dynamic instability (i.e, 'dynamic pull-in') is very high (Nayfeh and Mook, 1979; Nayfeh and Balachandran, 1995; Nayfeh, 2000), which can dangerously take place below the static pull-in voltage (SPV). Unfortunately, no studies have dealt with the effect of the AC loading on the pull-in limit. However, few studies have addressed the dynamic pull-in phenomenon for other kinds of dynamic loadings. Ananthasuresh et al. (1996) and Krylov and Maimon (2003) reported and analyzed the dynamic pull-in for switches actuated by a step voltage with various ramping rates (Ananthasuresh et al., 1996). Both studies (Ananthasuresh et al., 1996; Krylov and Maimon, 2003) indicate that the dynamic pull-in voltage can be as low as 91% of the SPV. In the presence of squeeze-film damping, the dynamic pull-in voltage is shown to approach the SPV (Krylov and Maimon, 2003).

1.4 Dissertation Objectives and Organizations

The objectives of the dissertation are:

- To model and simulate accurately the dynamics of microplates under the effect of squeeze-film damping and electrostatic forces and predict their quality factors for various gas pressures and DC loading using the compressible Reynolds equation coupled with a plate model.

- To express analytically the pressure distribution underneath a plate in terms of its structural mode shapes using perturbation methods, thereby reducing the dimension of the coupled system and hence the number of global variables required for the simulation.

- To study the global dynamics of MEMS resonators employing microbeams excited by primary-, superharmonic-, and subharmonic-resonance excitations. To calculate the microbeams resonance frequencies and amplitudes of vibration, and track their dynamic behavior up to the pull-in instability. To analyze the dynamic pull-in phenomenon and present guidelines for the design of MEMS resonators. To compare the simulation results of the global approach to these predicted analytically using the perturbation-based models of Younis and Nayfeh (2003) and Abdel-Rahman and Nayfeh (2003).

- To propose a novel RF MEMS switch actuated by a voltage load much lower than the traditionally used voltage. The new actuation method is based on dynamic pull-in. Here, we propose to actuate the switch using a combined DC and AC loading, similar to the actuation method used in MEMS resonators. The AC loading can be tuned by altering its amplitude and frequency to reach the pull-in instability with the lowest driving voltage and fastest response speed.

- To model and simulate thermoelastic damping in microplates and derive analytical expressions for their quality factors.

The organization of the dissertation is as follows. In Chapter 2, we present a general theoretical background of damping in MEMS. We focus on squeeze-film damp-

ing and the Reynolds equation (its assumptions, limitations, and modifications). In Chapter 3, we present a model utilizing the nonlinear Euler-Bernoulli beam equation coupled with a one-dimensional Reynolds equation to calculate the quality factors of electrically actuated microbeams under the effect of squeeze-film damping. We solve the eigenvalue problem, extract the quality factor of a resonator, and compare the results to experimental data. We conclude the chapter by remarking that this model is not adequate to capture the effect of the gas pressure underneath a plate and that a two-dimensional model is needed.

In Chapter 4, we present a model utilizing a linearized plate equation coupled with the compressible Reynolds equation to simulate the dynamic behavior of microplates (rectangular plates and circular discs) of generic boundary conditions under the effect of squeeze-film damping and small DC loading. We apply perturbation methods to the compressible Reynolds equation to express the pressure distribution in terms of the structural mode shape, which is substituted into a plate equation. The resulting equation is solved using a finite-element method for the natural frequencies, the structural mode shapes, the corresponding pressure distribution, and the quality factors. We validate the model by comparing the calculated quality factors to experimental data. In Chapter 5, we present a model to simulate the dynamics of microplates under the effect of squeeze-film damping and large electrostatic forces using the compressible Reynolds equation coupled with the von Kármán plate equations. We utilize the beam model of (Younis et al., 2003) to simulate the static behavior of the microplate under the effect of electrostatic forces. We derive analytical expressions for the pressure distribution in terms of the plate mode shapes around the deflected position, and hence eliminate the pressure as a variable in the solution procedure. We substitute the static deflection and the analytical expression of the pressure into the dynamic von Kármán plate equations and then solve the resulting equations using a finite-element method. We present several results showing the effect of the pressure and the DC electrostatic forcing on the structural mode shapes, the pressure distributions, the natural frequencies, and the quality factors.

In Chapter 6, we study thermoelastic damping in microplates and derive analytical expressions for their quality factors. We solve the heat equation for the thermal flux across the microplate, in terms of the plate deflection, and hence decouple the thermal equation from the plate equation. Then, we utilize a perturbation method, the method of strained parameters (Nayfeh, 1981), to derive an analytical expression for the quality factors of microplates, of general boundary conditions under electrostatic loading and residual stresses, in terms of their structural mode shapes. For the special case of no electrostatic and in-plane loadings, we derive a simple analytical expression for the quality factor.

In Chapter 7, we use the reduced-order model of (Younis et al., 2003) and (Abdel-Rahman et al., 2003b) to simulate the global dynamic behavior of MEMS resonators excited near their natural frequencies (primary-resonance excitation). Then we propose a novel RF MEMS switch. We utilize a shooting technique (Nayfeh and Balachandran, 1995) and long-time integrations of the equations of motion to predict periodic motions. We compare the simulation results of this approach to these predicted analytically using the model of (Younis and Nayfeh, 2003). We also remark about the dynamic pull-in phenomenon. Then we use the global approach to demonstrate the new actuation method for the proposed switch. In Chapter 8, we extend the analysis of Chapter 7 to secondary-resonance excitations. We simulate the dynamics of microbeams excited near half their fundamental natural frequencies (superharmonic excitation) and twice their fundamental natural frequencies (subharmonic excitation). For the superharmonic case, we present results showing the effect of varying the DC bias, the damping, and the AC excitation amplitude on the frequency-response curves. We show that the dynamic pull-in phenomenon can occur in a superharmonic excitation at an electric load much lower than that predicted based on static analysis. For the subharmonic case, we show that if the magnitude of the AC forcing exceeds the threshold activating the subharmonic resonance, all frequency-response curves will reach pull-in. Finally, in Chapter 9, we present summary and conclusions of the dissertation and conclude with recommendations for future work.

Chapter 2

Damping in MEMS

Damping in microelectromechanical systems (MEMS) strongly affects their performance, design, and control. Damping influences the behavior of MEMS in various ways, depending on their design criteria and operating conditions. For instance, in microaccelerometers, high damping (near critical) is desirable to prevent large resonance responses due to external disturbances, which might result in a mechanical or an electrical failure. On the other hand, in resonant sensors, a high quality factor is required for achieving high sensitivity and resolution. Hence, it is essential to understand the damping mechanisms in MEMS devices to optimize their designs.

2.1 Mechanisms of Energy Losses

There are several mechanisms of energy dissipation in MEMS devices (Tilmans et al., 1992). The most common include losses into the surrounding fluid due to acoustic radiation and viscous damping, losses into the structure mounts, and intrinsic damping caused by losses inside the material of the mechanical structure. Each source of energy loss can be described quantitatively in terms of a corresponding quality factor. The overall quality factor Q_{Tot} can be expressed in terms of the individual quality factors

Q_j as

$$\frac{1}{Q_{Tot}} = \sum_j \frac{1}{Q_j} \tag{2.1}$$

Support losses arise from uncanceled shear forces and moments at the end supports, which transfer energy from the vibrating element to the substrate. Support losses can be minimized by building a symmetric resonator so that it vibrates in a balanced way without moving its center of mass (Corman et al., 1997). Support losses can also be minimized by a proper design of the vibrating structure and its mounting mechanism, such as a double-ended tuning fork or a triple beam structure (Tilmans et al., 1992), and to isolate the vibrating element from the mount using a mechanical isolation mechanism. According to Zook et al. (1992), such special designs might introduce complicated modes of motion. Hence, they recommend designing resonators having fundamental natural frequencies much greater than the vibration modes in the supporting structure.

Acoustic radiation results from sound waves generated by the movement of the mechanical element in a direction normal to its surface. This mechanism can be significant if the acoustic wavelength is equal to or less than a typical dimension of the mechanical element, which is uncommon in MEMS. Intrinsic losses in single-crystal materials like silicon are very low and their contribution to the total damping is almost negligible compared to extrinsic losses. Hence, among all damping sources, viscous damping is the most significant source of energy loss in MEMS.

2.1.1 Squeeze-Film Damping

Typical MEMS devices employ a parallel-plate capacitor, in which one plate is actuated electrically and its motion is detected by capacitive changes. Examples of such devices are microaccelerometers, microswitches and microrelays, micropumps, resonant sensors, and gyroscopic sensors. In order to increase the efficiency of actuation and improve the sensitivity of detection, the distance between the capacitor plates is minimized and the area of the electrode is maximized. Under such conditions, the

so-called squeeze-film damping is pronounced. This phenomenon occurs as a result of the massive movement of the fluid underneath the plate, which is resisted by the viscosity of the fluid. This gives rise to a pressure distribution underneath the plate, which may act as a spring and/or a damping force. Recent studies show that the damping force dominates the spring force at low frequencies, whereas the spring force dominates the damping force at high frequencies. Therefore, viscous damping in many MEMS devices corresponds to squeeze-film damping.

2.2 Reynolds Equation

There are at least three approaches in the literature to model squeeze-film damping. The first approach utilizes statistical thermodynamics. It is based on studying the effect of collisions of the moving structure on the individual molecules of the gas, such as their effect in changing the molecules momentum (Christian, 1966) and energy (Bao et al., 2002). The second approach utilizes a simplified form of the Reynolds equation, obtained by assuming incompressible flow (starr, 1990), and hence it neglects the spring effect of the gas pressure. This simplification reduces the equation to a simple Possion equation, which is easier to solve than the original Reynolds equation. The third approach employs the compressible Reynolds equation, which is modified by correction factors to extend its validity over the operating range of MEMS devices. The third approach is more popular because it gives accurate results with high computational efficiency.

2.2.1 Assumptions and Derivation

The derivation of the Reynolds equation is based on a number of assumptions, which are essential to the understanding of its validity and limitations. The following are the most common (Hamrock, 1991; Khonsari and Booser, 2001):

1. The fluid is Newtonian (the shear stress is directly proportional to the velocity).

2. The fluid obeys the ideal gas law.

3. The inertia and body forces are negligible compared to the viscous and pressure forces.

4. The variation of pressure across the fluid film is negligibly small.

5. The flow is laminar.

6. The width of the gap separating the two plates, where the gas is trapped inside, is very small compared to the lateral extent of the plates.

7. The fluid can be treated as continuum and does not slip at the boundaries.

8. The system is isothermal.

Under these assumptions, the Reynolds equation is derived as follows (Hamrock, 1991; Khonsari and Booser, 2001). Without any loss of generality, we consider two parallel rectangular plates (Figure 2.1) separated by a gap of width d. We assume that one plate is moving vertically while the other plate is stationary. The plate has a length ℓ and a width b. A simplified form of the Navier-Stokes equations is obtained by an order-of-magnitude analysis, in which higher-order inertia and gravitation terms are dropped from the original equations. Then, the simplified equations are integrated across the gap width to obtain expressions for the fluid velocities. The results are substituted into the continuity equation to yield a primitive form of the Reynolds equation in terms of the pressure and density. Finally, assuming isothermal conditions and ideal gas law, the density is expressed in terms of the pressure, which in turn substituted into the Reynolds equation to obtain the following standard form of Reynolds equation:

$$\frac{\partial}{\partial x}\left(H^3 P\frac{\partial P}{\partial x}\right)+\frac{\partial}{\partial y}\left(H^3 P\frac{\partial P}{\partial y}\right)=12\eta\left(H\frac{\partial P}{\partial t}+P\frac{\partial H}{\partial t}\right) \tag{2.2}$$

Here, x and y are the positions along the length and width of the plate, respectively, t is time, H is the varying distance between the two plates, P is the total pressure, and η is the viscosity coefficient of the fluid.

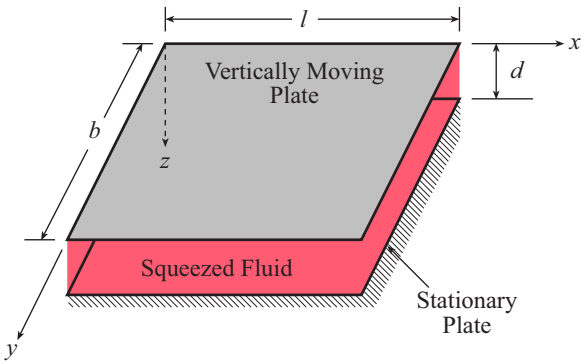

Figure 2.1: Schematic of a parallel-plate capacitor with a squeezed fluid.

2.2.2 Limitations and Correction Factors

In practical MEMS applications, the aforementioned assumptions of the Reynolds equation might not be completely satisfied. In fact, some assumptions are inherently violated in certain designs, making predictions of the Reynolds equation suspect. These violations and their effects have been studied and correction factors have been proposed to enable the use of a modified version of the Reynolds equation. Next, we discuss two violations: the continuum assumption (assumption 7) and the assumption of large dimensions of the plate compared to the width of the gap spacing (assumption 6). Other issues, such as thermoelastic effects (Zook, 1992), the effect of the surface roughness (Veijola et al., 1997; Khonsari and Booser, 2001), and the effect of turbulence flow (Khonsari and Booser, 2001) are less common and will not be addressed here.

Continuum-Fluid Consideration

The main assumption in equation (2.2) is that the gas in the gap can be treated as a continuum. The validity of this assumption depends on the so-called Knudsen number K_n (Khonsari and Booser, 2001), defined as

$$K_n = \frac{\lambda}{H} \tag{2.3}$$

where H is the variable distance between the two plates and λ is the molecular mean free path of the gas, which is the distance that a gas particle travels between collisions. The parameter λ is related to the local value of the pressure P_a as

$$\lambda = \frac{P_0 \lambda_0}{P_a} \tag{2.4}$$

where P_0 and λ_0 are the pressure and molecular mean free path at typical ambient conditions. Based on the Knudsen number, the flow can be divided into four regimes (Li, 2000): continuum flow when $K_n < 0.01$, slip flow when $0.01 < K_n < 0.1$, transitional flow when $0.1 < K_n < 10$, and free molecular flow when $K_n > 10$. In the continuum regime, the fluid is governed by the Navier-Stokes equations (or equivalently the Reynolds equation). Slip flow can be described by modifying the zero-velocity boundary conditions in the derivation of Reynolds equation to account for the slip of the flow at the plates boundaries (Burgdorfer, 1959). The flow in the transitional regime is a more subtle issue that needs special treatment (Beskok and Karniadakis, 1996). In the molecular regime, the intermolecular collisions can be neglected and the fluid is governed by the Boltzmann transportation equation.

Many MEMS devices are designed to operate at very low pressure with a very small gap between the capacitor electrodes. Under such conditions, the Knudsen number is closer to the noncontinuum regimes, making the use of the Reynolds equation suspect. Fortunately, recent extensive research has extended the validity of the Reynolds equation to the noncontinuum regimes, thereby enabling description of the flow using a single model. This is achieved by using the so-called 'effective viscosity coefficient' η_{eff}, which depends directly on the Knudsen number.

Various models have been proposed for η_{eff} since the beginning of the 20th century, when Knudsen presented a correction coefficient based on his research on the gas flow in capillary tubes (Veijola et al., 1995). His coefficient has been used recently by Andrews et al. (1993) and gave good results. Another well-known correction factor was presented by Burgdorfer (1959). He accounted for the slip flow regime by modifying the boundary conditions to take into account, to the first-order approximation, the slip

velocities. His modified Reynolds equation has been widely used, examples are found in (Hung and Senturia, 1999) and (McCarthy et al., 2002). However, the Knudsen model is limited to the range $0 < K_n < 1$ (Khonsari and Booser, 2001). Thanks to the active research in MEMS, many other models have been proposed in the last two decades. Summary of these models and comparison among some of them are given by (Veijola et al., 1995) and (Li and Hughes, 2000). Here we list these models in Table 2.1. Although all models give close results, the model of Veijola et al. (1995) tends to be more accurate because it is valid over a wider range of K_n. Their model is an empirical approximation of the more complicated expression proposed by Fukui and Kaneko (1988) based on the Boltzmann transport equation.

Table 2.1: List of effective viscosity models. The parameter α is the accommodation coefficient (approximately equal one) and Q is a coefficient related to the Poiseuille flow (Yang, 1998).

Author	Year	Effective Viscosity (η_{eff})	Derived from
Knudsen	1906	$\frac{\eta}{1+\frac{K_n(K_n+2.507)}{0.1474(K_n+3.095)}}$	Gas flow in capillary tubes
Burgdorfer	1959	$\frac{\eta}{1+6K_n}$	Navier-Stokes Eqs. + slip flow
Hsia and Domoto	1983	$\frac{\eta}{1+6K_n+6K_n^2}$	Experimental data fitting
Fukui and Kaneko	1988	$\frac{\eta D}{6Q(D)}, \quad D=\frac{\sqrt{\pi}}{2K_n}$	Boltzmann equation
Seidel et al.	1993	$\frac{0.7\eta}{0.7+K_n}$	Experimental data fitting
Mitsuya	1993	$\frac{\eta}{1+6\frac{2-\alpha}{\alpha}K_n+\frac{8}{3}K_n^2}$	Navier-Stokes Eqs.+ slip flow
Veijola et al.	1995	$\frac{\eta}{1+9.638K_n^{1.159}}$	Fukui and Kaneko model
Andrews and Harris	1995	$\frac{\eta}{1+6.8636K_n^{0.9906}}$	Experimental data fitting

Finite Size and Edges Considerations

In some MEMS devices, the ratio of the gap width to the plate length or width is not sufficiently large, which might violate assumption 6 of Section 2.2.1. In such cases, the Reynolds equation in its original form is inaccurate (Schrag and Wachutka, 2001). Other issues like acoustic radiations and non-developed flow at the edges become important. Schrag and Wachutka (2001) compared results of the damping and spring forces obtained using the Reynolds equation with results obtained using the Navier-

Stokes-based finite-element program for different ratios of the plate length and width to the gap width. The results show erroneous predictions of the Reynolds equation for ratios 5 and 10, whereas the results are on good agreement for ratio 100. Veijola et al. (2001) compared results of a modified Reynolds equation including acoustic edge effects with results of the original Reynolds equation. They found that the damping force predicted with the modified model is 1.07 and 2.0 of that predicted with the unmodified Reynolds equation when the length-to-gap ratio was 100 and 7, respectively. A similar observation was also reported by Vemuri et al. (2000), who showed that the percentage error in the original Reynolds equation increases with decreasing plate length.

2.3 Intrinsic Damping

Extrinsic damping mechanisms can be minimized by a proper design of devices and their operating conditions. For example, squeeze-film damping can be minimized by increasing the distance between the capacitor electrodes, perforating one of the electrodes, and encapsulating the device at a very low pressure. Support losses also can be minimized by a proper design of the vibrating structure and its mounting mechanism. Intrinsic mechanisms on the other hand are more difficult to control because they depend primarily on the material and geometric properties of the structures. Intrinsic damping increases significantly with minituirization of devices and can limit the quality factors of microstructures in the micro and sub-micro scales.

Intrinsic damping in MEMS is still a very active research topic. There are many mechanisms that contribute to intrinsic damping, however the exact contribution of each of them is still unclear. Example of these mechanisms are (Duemling, 2002) phonon-phonon scattering; phonon-phonon-electron scattering; and surface losses, such as losses due to thin film, metal layer, oxide layer, and water layer. There is also energy dissipation due to the relaxation phenomenon. This mechanism is characterized by a peak and a relaxation time (this process is also called Debye relaxation). Examples of this category are thermoelastic relaxation, defect relaxation, and grain-boundary relaxation. Recent studies have shown that thermoelastic damping can be a dominant

source of intrinsic damping in MEMS.

2.3.1 Thermoelastic Damping

Thermoelastic damping, also called internal friction, can occur in any material subjected to cyclic stress (Roszhart, 1990). This mechanism becomes a very significant source of energy loss when the period of cyclic stress approaches a structure's thermal constant. In a thermoelastic solid (Lifshitz and Roukes, 2000), the strain and temperature are coupled through the material thermal expansion coefficient. This coupling provides an energy dissipation mechanism, which allows the system to relax to equilibrium. The relaxation is achieved through the irreversible heat flow across the material of structure with different temperature zones. An example is the case of a structure in bending, in which one of its side is under tension, with cooler temperature, and the other side is under compression, with higher temperature.

Chapter 3

A One-Dimensional Model for Electrically Actuated Microstructures under the Effect of Squeeze-Film Damping

In this chapter, we investigate the behavior of electrically actuated microstructures under the effect of squeeze-film damping. Younis (2001) concluded that the nonlinear Euler-Bernoulli beam model can be used to simulate the static and dynamic behavior of a microplate of symmetric boundary conditions and under uniformly distributed electrostatic forces. In this chapter, we extend this model to include the effect of squeeze-film damping using the nonlinear Euler-Bernoulli beam equation coupled with the one-dimensional compressible Reynolds equation. Such a model is very attractive because it is computationally much simpler than a two-dimensional Reynolds equation coupled with a plate equation.

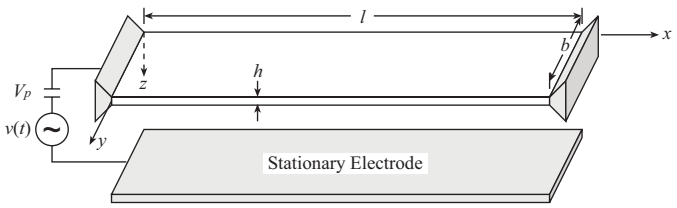

Figure 3.1: A schematic drawing of an electrically actuated microplate.

3.1 Problem Formulation

We consider a microplate, Figure 3.1, actuated by an electric load composed of a DC component (polarization voltage) V_p and an AC component $v_e(t)$ and subject to a net pressure force $\bar{P}(x,t)$ per unit area due to the squeeze-film damping effect. Due to the symmetric nature of the electrostatic loading and the plate boundary conditions, we approximate the plate as a beam and write the equation of motion governing its transverse deflection as

$$EI\frac{\partial^4 w}{\partial x^4}+\rho bh\frac{\partial^2 w}{\partial t^2}=\left[\frac{EA}{2\ell}\int_0^\ell\left(\frac{\partial w}{\partial x}\right)^2 dx+\hat{N}\right]\frac{\partial^2 w}{\partial x^2} - \bar{P}b+\tfrac{1}{2}\epsilon_0\epsilon_r b\frac{\left(V_p+v_e(t)\right)^2}{\left(d-w\right)^2} \tag{3.1}$$

where x is the position along the microbeam length ℓ, $w(x,t)$ is the deflection of the microbeam, t is time, ρ is the material density, h is the microbeam thickness, b is the microbeam width, d is the gap width, A and I are the area and moment of inertia of the cross section, E is Young's modulus, $\hat{N}$ is the applied axial force, ϵ_0 is the dielectric constant of vacuum, and ϵ_r is the relative dielectric constant of the gap medium to an air gap. The last term in equation (3.1) represents the parallel-plate electric force assuming complete overlapping between the area of the microbeam and the stationary electrode. The microbeam is assumed to be clamped at both ends; hence the boundary conditions are

$$w(0,t)=w(\ell,t)=0, \qquad \frac{\partial w(0,t)}{\partial x}=\frac{\partial w(\ell,t)}{\partial x}=0 \tag{3.2}$$

The microbeam deflection under an electric force is composed of a static component due to the DC voltage, denoted by $w_s(x)$, and a dynamic component due to the AC voltage, denoted by $u(x,t)$; that is,

$$w(x,t) = w_s(x) + u(x,t) \tag{3.3}$$

The pressure is generally governed by the two-dimensional Reynolds equation, equation (2.2). Next, we linearize equation (2.2) assuming small-deflection and pressure variations. To this end, we express the variable distance H between the beam and the substrate as

$$H(x,y,t) = d - w_s(x) - u(x,t) \tag{3.4}$$

and write the total pressure P as

$$P(x,y,t) = P_a + \bar{P}(x,y,t) \tag{3.5}$$

where P_a is the static pressure in the gap. Substituting equations (3.3)-(3.5) into equation (2.2) and retaining the linear terms in the outcome, we obtain the linearized compressible Reynolds equation

$$\frac{\partial}{\partial x}\left[(d-w_s)^3 P_a \frac{\partial \bar{P}}{\partial x}\right] + \frac{\partial}{\partial y}\left[(d-w_s)^3 P_a \frac{\partial \bar{P}}{\partial y}\right] = 12\eta_{eff}\left[(d-w_s)\frac{\partial \bar{P}}{\partial t} - P_a \frac{\partial u}{\partial t}\right] \tag{3.6}$$

where η has been replaced by η_{eff}, the effective viscosity of the fluid in the gap, to account for the rarefied gas effect through its dependence on the Knudsen number. Here we use the model of Veijola et al. (1995) for η_{eff}. The pressure boundary conditions are zero flux at the clamped edges of the beam and trivial pressure at the open edges; that is,

$$\bar{P}(x,0,t) = \bar{P}(x,b,t) = 0 \tag{3.7}$$

$$\frac{\partial \bar{P}(0,y,t)}{\partial x} = \frac{\partial \bar{P}(\ell,y,t)}{\partial x} = 0 \tag{3.8}$$

Assuming the pressure variation across the beam width is small (i.e., assuming negligible side leakage from the gap spacing), we let the pressure and its gradient in equation (3.6) be independent of y and obtain the linearized one-dimensional Reynolds equation

$$\frac{\partial}{\partial x}\left[(d-w_s)^3 P_a \frac{\partial \bar{P}}{\partial x}\right] = 12\eta_{eff}\left[(d-w_s)\frac{\partial \bar{P}}{\partial t} - P_a \frac{\partial u}{\partial t}\right] \tag{3.9}$$

and the boundary conditions are given in equation (3.8).

For convenience, we introduce the nondimensional variables (denoted by stars)

$$x^* = \frac{x}{\ell}, \qquad t^* = \frac{t}{T}, \qquad w_s^* = \frac{w_s}{d}, \qquad u^* = \frac{u}{d}, \qquad \bar{P}^* = \frac{\bar{P}}{P_a} \tag{3.10}$$

where $T = \left(\frac{\rho b h \ell^4}{EI}\right)^{\frac{1}{2}}$. Substituting equations (3.10) into equations (3.1), (3.2), (3.8), and (3.9) and dropping the stars, we obtain the following system of coupled nondimensional partial-differential equations:

$$\frac{\partial^4 w}{\partial x^4} + \frac{\partial^2 w}{\partial t^2} = \left[\alpha_1 \Gamma(w,w) + N\right]\frac{\partial^2 w}{\partial x^2} - P_{non}\bar{P} + \alpha_2 \frac{\left[V_p + v_e(t)\right]^2}{(1-w)^2} \tag{3.11a}$$

$$w(0,t) = w(1,t) = 0, \qquad \frac{\partial w(0,t)}{\partial x} = \frac{\partial w(1,t)}{\partial x} = 0 \tag{3.11b}$$

$$\frac{\partial}{\partial x}\left[(1-w_s)^3 \frac{\partial \bar{P}}{\partial x}\right] = \sigma\left[(1-w_s)\frac{\partial \bar{P}}{\partial t} - \frac{\partial u}{\partial t}\right] \tag{3.12a}$$

$$\frac{\partial \bar{P}(0,t)}{\partial x} = \frac{\partial \bar{P}(1,t)}{\partial x} = 0 \tag{3.12b}$$

where

$$\Gamma\left(f_1(x,t), f_2(x,t)\right) = \int_0^1 \frac{\partial f_1}{\partial x}\frac{\partial f_2}{\partial x} dx$$

The nondimensional parameters appearing in equations (3.11) and (3.12) are

$$\alpha_1 = 6\left(\frac{d}{h}\right)^2,\ N = \frac{\hat{N}\ell^2}{EI},\ \alpha_2 = \frac{6\epsilon_0\epsilon_r\ell^4}{Eh^3d^3},\ P_{non} = \frac{P_a b\ell^4}{EId},\ \sigma = \frac{12\eta_{eff}\ell^2}{d^2P_aT} \tag{3.13}$$

The parameter σ is the squeeze number (Senturia, 2000), which represents a measurement of the compressibility of the fluid in the gap. For values of σ near infinity, corresponding to high oscillation frequency, the fluid is trapped in the gap and acts like a spring. For values of σ near zero, corresponding to low oscillation frequency, the fluid is nearly incompressible.

To calculate the static deflection of the microbeam, we set the time derivatives and the forcing terms in equation (3.11a) equal to zero and obtain

$$\frac{d^4w_s}{dx^4} = \left[\alpha_1\Gamma(w_s,w_s)+N\right]\frac{d^2w_s}{dx^2} + \frac{\alpha_2V_p^2}{(1-w_s)^2} \tag{3.14a}$$

It follows from equations (3.11b) and (3.3) that the boundary conditions are

$$w_s = 0 \ \text{ and } \ \frac{dw_s}{dx} = 0 \ \text{ at } \ x = 0 \ \text{ and } \ x = 1 \tag{3.14b}$$

We generate the problem governing the dynamic behavior of the microbeam around the deflected shape by substituting equation (3.3) into equations (3.11a) and (3.11b) and using equations (3.14) to eliminate the terms representing the equilibrium position. To third-order in u, the result is

$$\begin{aligned}\frac{\partial^2u}{\partial t^2} + \frac{\partial^4u}{\partial x^4} &= \left(\alpha_1\Gamma\left(w_s,w_s\right)+N\right)\frac{\partial^2u}{\partial x^2} - P_{non}\bar{P} + 2\alpha_1\Gamma\left(w_s,u\right)\frac{d^2w_s}{dx^2}\\ &+ \frac{2\alpha_2V_p^2}{\left(1-w_s\right)^3}u + \alpha_1\Gamma\left(u,u\right)\frac{d^2w_s}{dx^2} + 2\alpha_1\Gamma\left(w_s,u\right)\frac{\partial^2u}{\partial x^2}\\ &+ \frac{3\alpha_2V_p^2}{\left(1-w_s\right)^4}u^2 + \alpha_1\Gamma\left(u,u\right)\frac{\partial^2u}{\partial x^2} + \frac{4\alpha_2V_p^2}{\left(1-w_s\right)^5}u^3\\ &+ \frac{2\alpha_2V_p}{\left(1-w_s\right)^2}v_e(t) + \frac{4\alpha_2V_p}{\left(1-w_s\right)^3}v_e(t)u + \cdots\end{aligned} \tag{3.15a}$$

$$u(0,t) = u(1,t) = 0, \qquad \frac{\partial u(0,t)}{\partial x} = \frac{\partial u(1,t)}{\partial x} = 0 \tag{3.15b}$$

where the term involving $v_e^2(t)$ is dropped because typically $v_e^2(t) << V_p^2$.

3.1.1 Linear Eigenvalue Problem

To derive the linear damped eigenvalue problem, we drop the nonlinear and forcing terms in Equation (3.15a) and obtain

$$\frac{\partial^4 u}{\partial x^4} - (\alpha_1\Gamma_1 + N)\frac{\partial^2 u}{\partial x^2} - 2\alpha_1\Gamma\left(w_s, u\right)\frac{d^2 w_s}{dx^2} + P_{non}\bar{P} - \frac{2\alpha_2 V_p^2}{\left(1-w_s\right)^3}u = -\frac{\partial^2 u}{\partial t^2} \quad (3.16a)$$

$$u = 0 \text{ and } \frac{\partial u}{\partial x} = 0 \text{ at } x = 0 \text{ and } x = 1 \quad (3.16b)$$

where $\Gamma_1 = \Gamma\left(w_s, w_s\right)$. Next, we let

$$u(x,t) = \phi_n(x)e^{i\omega_n t} \quad (3.17)$$

$$\bar{P}(x,t) = \psi_n(x)e^{i\omega_n t} \quad (3.18)$$

where $\phi_n(x)$ and $\psi_n(x)$ are the nth mode shapes of the beam and the pressure, respectively, and ω_n is the corresponding nondimensional natural frequency. Next, we substitute equations (3.17) and (3.18) into equations (3.12) and (3.16) and obtain

$$\phi_n^{iv} - (\alpha_1\Gamma_1 + N)\phi_n^{''} - 2\alpha_1\Gamma_2 w_s^{''} + P_{non}\psi_n - \frac{2\alpha_2 V_p^2}{\left(1-w_s\right)^3}\phi_n = \omega_n^2\phi_n \quad (3.19a)$$

$$\phi_n = \phi_n^{'} = 0 \qquad \text{at} \qquad x = 0 \text{ and } x = 1 \quad (3.19b)$$

$$\frac{d}{dx}\left[(1-w_s)^3\psi_n^{'}\right] = i\omega_n\sigma\left[(1-w_s)\psi_n - \phi_n\right] \quad (3.20a)$$

$$\psi_n^{'}(0,t) = \psi_n^{'}(1,t) = 0 \quad (3.20b)$$

where $\Gamma_2 = \Gamma\left(w_s, \phi_n\right)$ and the prime denotes the derivative with respect to x. Equations (3.19a)-(3.20b) represent a coupled system of linear ordinary-differential equations, which are solved numerically for the complex eigenvalues and eigenfunctions and the corresponding pressure distribution underneath the microbeam.

3.1.2 Perturbation Analysis

Next, we apply a perturbation method to equations (3.19a)-(3.20b) to derive an analytical expression for the pressure distribution in terms of the structural mode shape. Also, we derive an analytical expression for the quality factor of the microbeam in terms of its mode shape. This expression presents a more accurate way of calculating the quality factor. This is because extracting the quality factor by a direct numerical solution of equations (3.19a)-(3.20b) yields a complex eigenvalue, which has a real part much larger than the imaginary part. Hence, the accuracy of the imaginary part is poor compared to that of the real part.

We note that the right-hand side of equation (3.20a) is multiplied by a large-magnitude coefficient ($i\omega_n\sigma$). Typically, ω_n for a clamped-clamped beam is near 23, whereas σ ranges from unity at very low frequencies and gas pressures to more than hundred at high frequencies and pressures. Hence, dividing equation (3.20a) by $i\omega_n\sigma$ makes the left-hand side of the equation very small. Next, we apply the method of strained parameters (Nayfeh, 1981) and seek a first-order solution to equations (3.19a)-(3.20b) in the form

$$\phi_n = \phi_{n_0} + \epsilon_1\phi_{n_1} \tag{3.21}$$

$$\psi_n = \psi_{n_0} + \epsilon_1\psi_{n_1} \tag{3.22}$$

$$\omega_n = \omega_{n_0} + \epsilon_1\omega_{n_1} \tag{3.23}$$

where $\epsilon_1 = \frac{1}{\sigma\omega_{n_0}}$ Substituting equations (3.21)-(3.23) into equations (3.19a)-(3.20b), and separating coefficients of like power of ϵ_1 we obtain

$\underline{O(\epsilon_1^0)}$

$$\psi_{n_0} = \frac{\phi_{n_0}}{1-w_s} \tag{3.24}$$

$$\begin{aligned}\mathcal{L}(\phi_{n_0},\psi_{n_0}) &= \phi_{n_0}^{iv} - (\alpha_1\Gamma_1 + N)\phi_{n_0}^{''} - 2\alpha_1\Gamma_2(w_s,\phi_{n_0})w_s^{''} + P_{non}\psi_{n_0} - \frac{2\alpha_2 V_p^2}{(1-w_s)^3}\phi_{n_0} \\ &= \omega_{n_0}^2\phi_{n_0}\end{aligned} \tag{3.25}$$

$\underline{O(\epsilon_1)}$

$$\psi_{n_1} = \frac{\phi_{n_1} - i\frac{d}{dx}\left[(1-w_s)^3\psi'_{n_0}\right]}{(1-w_s)} \tag{3.26}$$

$$\mathcal{L}(\phi_{n_1}, \psi_{n_1}) - \omega_{n_0}^2\phi_{n_1} = 2\omega_{n_0}\omega_{n_1} \tag{3.27}$$

The boundary conditions for equations (3.25) and (3.27) are

$$\phi_{n_j} = 0 \text{ and } \phi'_{n_j} = 0 \quad \text{at } x = 0 \text{ and } x = 1, \ j = 1, 2 \tag{3.28}$$

Substituting equation (3.24) into equation (3.25) and equations (3.24) and (3.26) into equation (3.27), we obtain

$$\phi_{n_0}^{iv} - (\alpha_1\Gamma_1 + N)\phi''_{n_0} - 2\alpha_1\Gamma_2(ws, \phi_{n_0})w''_s + P_{non}\frac{\phi_{n_0}}{1-w_s} - \frac{2\alpha_2 V_p^2}{(1-w_s)^3}\phi_{n_0} - \omega_{n_0}^2\phi_{n_0} = 0 \tag{3.29}$$

$$\phi_{n_1}^{iv} - (\alpha_1\Gamma_1 + N)\phi''_{n_1} - 2\alpha_1\Gamma_2(w_s, \phi_{n_1})w''_s + \left[\frac{P_{non}}{(1-w_s)} - \omega_{n_0}^2\right]\phi_{n_1} - \frac{2\alpha_2 V_p^2}{(1-w_s)^3}\phi_{n_1} = \frac{iP_{non}}{(1-w_s)}\frac{d}{dx}\left[(1-w_s)^3\frac{d}{dx}\left(\frac{\phi_{n_0}}{(1-w_s)}\right)\right] + 2\omega_{n_0}\omega_{n_1}\phi_{n_0} \tag{3.30}$$

We note that the homogeneous problem governing ϕ_{n_1} is the same as the problem governing ϕ_{n_0} and because the latter has nontrivial solutions, the nonhomogeneous problem governing ϕ_{n_1} has a solution only if the right-hand side of equation (3.30) is orthogonal to every solution of the adjoint homogeneous problem governing ϕ_{n_1} (solvability condition (Nayfeh, 1981)). Because the problem is self-adjoint, the solvability condition demands that the right-hand side of equation (3.30) be orthogonal to ϕ_{n_0}; that is,

$$2\omega_{n_0}\omega_{n_1}\int_0^1 \phi_{n_0}^2 dx + iP_{non}\int_0^1 \left\{\frac{\phi_{n_0}}{(1-w_s)}\frac{d}{dx}\left[(1-w_s)^3\frac{d}{dx}\left(\frac{\phi_{n_0}}{(1-w_s)}\right)\right]\right\}dx = 0 \tag{3.31}$$

Integrating the second integral in equation (3.31) by parts, using equation (3.28),

and solving for ω_{n_1}, we obtain

$$\omega_{n_1} = \frac{iP_{non}}{2\omega_{n_0}} \int_0^1 \left\{ \left[\frac{d}{dx} \left(\frac{\phi_{n_0}}{(1-w_s)} \right) \right]^2 (1-w_s)^3 \right\} dx \tag{3.32}$$

where ϕ_{n_0} is normalized such that $\int_0^1 \phi_{n_0}^2 dx = 1$. As noted from equation (3.23), equation (3.32) yields the imaginary part of ω_n, and hence the damping of the system.

The quality factor can be related to the imaginary part of the eigenvalue by recalling the relation between the damping coefficient and the quality factor for a spring-damper-mass system; that is,

$$Q = \frac{1}{2\zeta} \tag{3.33}$$

which can also be rewritten as

$$Q = \frac{\text{Re}(\omega_n)}{2\text{Imag}(\omega_n)} \tag{3.34}$$

where Re and Imag denote the real and imaginary parts, respectively.

3.2 Results

In this section, we calculate the natural frequencies and quality factors of an electrically actuated microbeam under various gas pressures. We first solve the boundary-value problems, equations (3.14a, 3.14b), numerically using a shooting method (Younis et al., 2002; Abdel-Rahman et al., 2002) for the static deflection of the microbeam under a DC loading. Then, we use two approaches to calculate the quality factor of the deflected microbeam. In the first approach, we solve equations (3.19a-3.20b) numerically using the shooting method for the complex eigenvalues, from which we calculate the natural frequencies and quality factors. In the second method, we solve equations (3.28) and (3.29) for the microbeam mode shapes and natural frequencies and then use equations (3.32) and (3.34) to calculate the quality factors.

We consider a microbeam, employed as a transducer in a resonant sensor (Tilmans

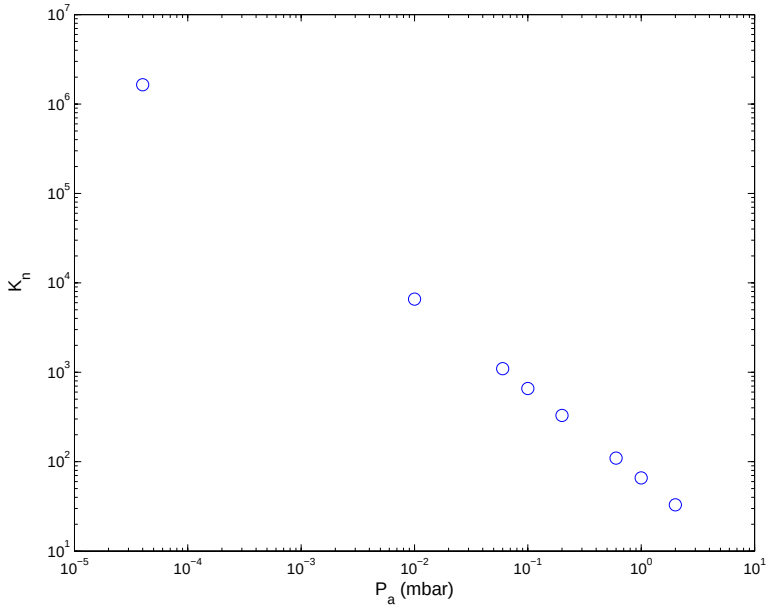

Figure 3.2: Variation of the Knudsen number with the cavity pressure of the experimental data of Legtenberg and Tilmans (1994).

and Legtenberg, 1994), with $\ell = 210\mu m$, $h = 1.5\mu m$, $b = 100\mu m$, $d = 1.18\mu m$, and $E = 166GPa$. The microbeam is subjected to an axial load of 0.0009 $Newton$ and a DC loading of $V_p = 6V$. The resonator is encapsulated at very low pressure. Tilmans and Legtenberg (1994) reported an experimental value of the quality factor near vacuum $Q_{vacuum} = 18500$ at $P_a = 6 \times 10^{-6} mbar$. We use this value with equation (2.1) to account for the structural damping of the microbeam.

In Figure 3.2, we show a plot for the Knudsen number K_n calculated using equations (2.3) and (2.4) versus the cavity pressure P_a of the resonator (Legtenberg and Tilmans, 1994). The figure shows high values of K_n exceeding the continuum limit. Hence, an effective viscosity coefficient should be used in the Reynolds equation. Figure 3.3 shows variation of the squeeze number σ with P_a. We note that the values of σ are relatively small, indicating that, for this range of pressure, the damping effect of the pressure dominates the spring effect.

Figure 3.4 shows the variation of the dimensional fundamental natural frequency f_1 with the cavity pressure P_a. The numerical values of f_1 are in the range of the experi-

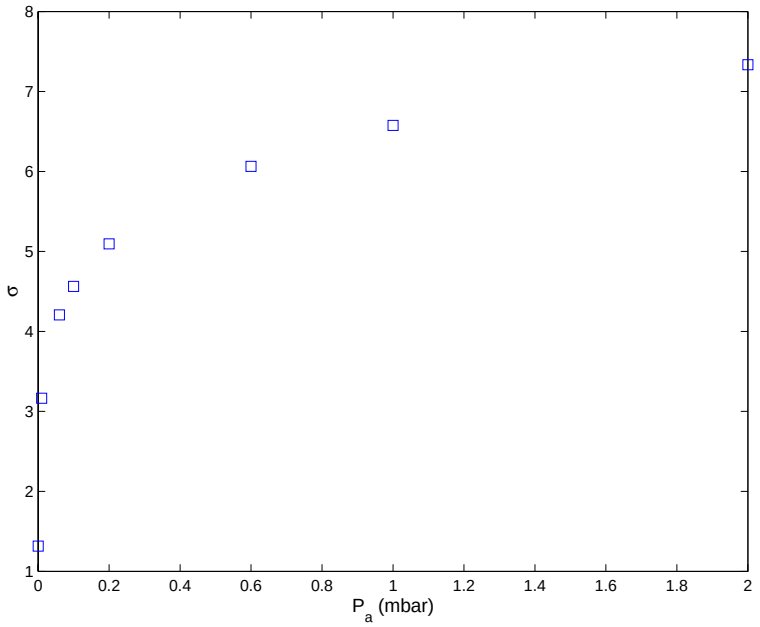

Figure 3.3: Variation of the squeeze number with the cavity pressure of the experimental data of Legtenberg and Tilmans (1994).

mental value reported by (Tilmans and Legtenberg, 1994), which is $f_1 = 322.045$ kHz. We note that f_1 changes very slightly with the pressure, which agrees with the observations of (Gui et al. 1995) and (Andrews et al., 1993) and with the expectations drawn from Figure 3.3.

In Figure 3.5, we compare the calculated quality factors using the direct numerical approach (stars) and the perturbation approach (circles) with the experimental data (triangles) of Legtenberg and Tilmans (1994). We note that both methods give qualitatively good agreement with the experiment. Quantitatively, the perturbation approach shows improvement over the direct numerical approach, however both approaches give poor agreement with the experiment. We attribute this discrepancy to the neglection of the variation of the pressure in the y direction. In another words, neglecting leakage across the width of the beam does not represent properly the physics of the squeeze-film damping phenomenon, in which the air is sucked and pumped underneath the beam from its open sides. Consequently, we conclude that a two-dimensional model is necessary to account properly for the effect of squeeze-film damping.

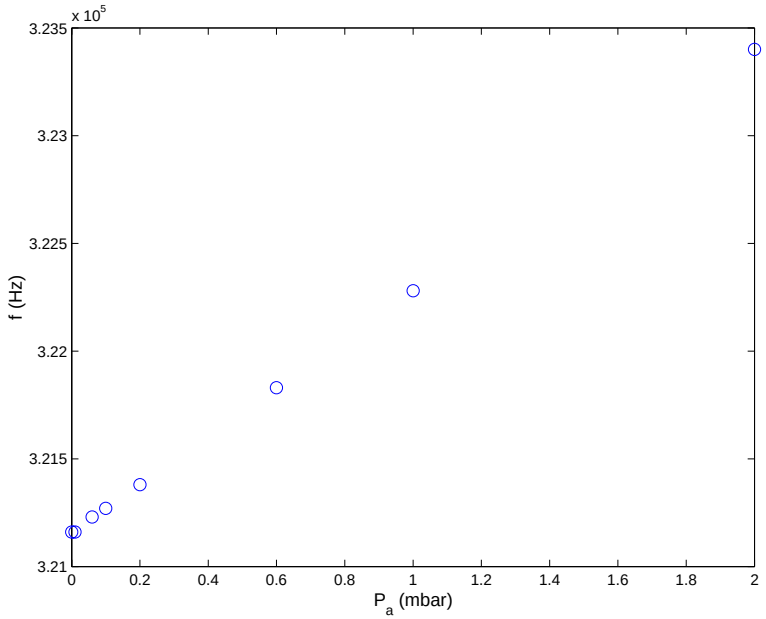

Figure 3.4: Variation of the dimensional fundamental natural frequency of a 210μm length resonator with the cavity pressure.

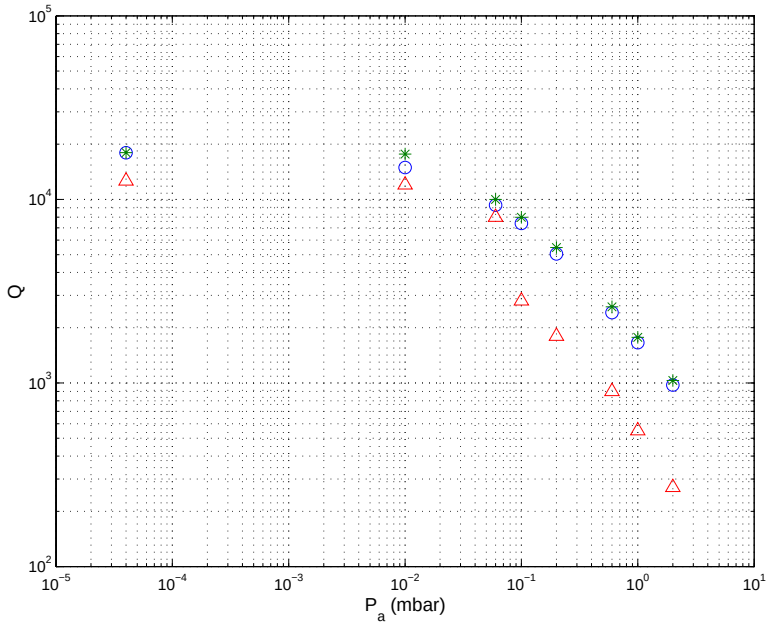

Figure 3.5: A comparison of the calculated quality factors using the direct numerical approach (stars) and using the perturbation approach (circles) with the experimental data (triangles) of Legtenberg and Tilmans (1994).

Chapter 4

A Model of Microplates under the Effect of Squeeze-Film Damping and Small Electrostatic Forces

In this chapter, we present a new approach to the modeling and simulation of flexible microstructures under the effect of squeeze-film damping. The approach utilizes the compressible Reynolds equation coupled with the equation governing the plate deflection. The model accounts for electrostatic forcing of the capacitor airgap, the restoring force of the microplate, and applied in-plane loads. It also accounts for the slip condition of the flow at very low pressures. Perturbation methods are used to derive an analytical expression for the pressure distribution in terms of the structural mode shapes. This expression is substituted into the plate equation, which is solved in turn using a finite-element method for the structural mode shapes, the pressure distributions, the natural frequencies, and the quality factors. We apply the new approach to a variety of rectangular and circular plates and present expressions for the pressure distributions and quality factors. Our theoretically calculated quality factors are in excellent agreement with available experimental data and hence can be used to

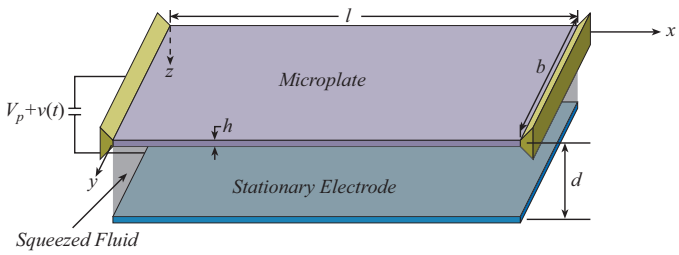

Figure 4.1: Electrically actuated microplate under the effect of squeeze-film damping.

simulate accurately the dynamics of flexible microstructures and predict their quality factors under a wide range of gas pressures.

Because the pressure distribution is related analytically to the deflection, the dimension of the coupled structural-fluidic problem and hence the number of global variables needed to describe the dynamics of the system is reduced considerably. Consequently, the new approach can be significant to the development of computationally efficient CAD tools for MEMS.

4.1 Problem Formulation

We consider a microplate (Figure 4.1) actuated by an electric load composed of a DC component V_p and an AC component $v_e(t)$ and subject to a net pressure force $\bar{P}(x, y, t)$ per unit area due to the gas in the gap. Assuming small strains and displacements, we obtain the following linear equation of motion that governs the transverse deflection of the microplate (Leissa, 1969):

$$D\left(\frac{\partial^4 w}{\partial x^4}+2\frac{\partial^4 w}{\partial x^2\partial y^2}+\frac{\partial^4 w}{\partial y^4}\right)-\hat{N}_1\frac{\partial^2 w}{\partial x^2}+\rho h\frac{\partial^2 w}{\partial t^2}=-\bar{P}+\frac{\epsilon_0\epsilon_r V_p v_e}{d^2}+\frac{\epsilon_0\epsilon_r V_p^2}{d^3}w \tag{4.1}$$

where $w(x, y, t)$ is the transverse deflection of the plate at the position x and y at time t, ρ is the plate material density, d is the initial gap width, $D=\frac{Eh^3}{12(1-\nu^2)}$ is the plate flexural rigidity, h is the microplate thickness, E is Young's modulus, ν is Poisson's ratio, $\hat{N}_1$ is the axial force per unit length in the x direction, ϵ_0 is the dielectric

constant of vacuum, and ϵ_r is the relative dielectric constant of the gap medium to an airgap. The last two terms in equation (4.1) represent an approximation to the parallel-plate electrostatic force assuming a small DC loading and complete overlapping of the microbeam and the stationary electrode. The term involving $v_e^2(t)$ has been dropped because, typically, $v_e \ll V_p$.

The boundary conditions of the plate are

Free edges at $y = 0$ and $y = b$

$$\frac{\partial^2 w}{\partial y^2} + \nu \frac{\partial^2 w}{\partial x^2} = 0 \tag{4.2}$$

$$\frac{\partial^3 w}{\partial y^3} + (2 - \nu) \frac{\partial^3 w}{\partial x^2 \partial y} = 0 \tag{4.3}$$

Clamped edges at $x = 0$ and $x = \ell$

$$w = 0 \tag{4.4}$$

$$\frac{\partial w}{\partial x} = 0 \tag{4.5}$$

The pressure is governed generally by the nonlinear Reynolds equation

$$\frac{\partial}{\partial x}\left(H^3 P \frac{\partial P}{\partial x}\right) + \frac{\partial}{\partial y}\left(H^3 P \frac{\partial P}{\partial y}\right) = 12\eta_{eff}\left(H\frac{\partial P}{\partial t} + P\frac{\partial H}{\partial t}\right) \tag{4.6}$$

where H is the variable distance between the two plates, P is the absolute pressure, and η_{eff} is the effective viscosity of the fluid in the gap, which accounts for the rarefied gas effect through its dependence on the Knudsen number. Here we use the model of Veijola et al. (1995) for η_{eff}. We linearize equation (4.6) around the undeflected microplate and the static pressure P_a in the airgap. To this end, we express H and P as

$$H(x, y, t) = d - w(x, y, t) \tag{4.7}$$

$$P(x, y, t) = P_a + \bar{P}(x, y, t) \tag{4.8}$$

Substituting equations (4.7) and (4.8) into equation (4.6) and linearizing the outcome,

we obtain

$$\frac{\partial^2 \bar{P}}{\partial x^2} + \frac{\partial^2 \bar{P}}{\partial y^2} = 12\frac{\eta_{eff}}{P_a d^3}\left(d\frac{\partial \bar{P}}{\partial t} - P_a\frac{\partial w}{\partial t}\right) \tag{4.9}$$

The pressure boundary conditions for the case in Figure 4.1 are zero flux at the clamped edges of the plate and trivial pressure at the open edges; that is,

$$\bar{P}(x,0,t) = \bar{P}(x,b,t) = 0 \tag{4.10}$$

$$\frac{\partial \bar{P}(0,y,t)}{\partial x} = \frac{\partial \bar{P}(\ell,y,t)}{\partial x} = 0 \tag{4.11}$$

For convenience, we introduce the nondimensional variables (denoted by stars)

$$x^* = \frac{x}{\ell}, \qquad y^* = \frac{y}{\ell}, \qquad t^* = \frac{t}{T}, \qquad w^* = \frac{w}{d}, \qquad \bar{P}^* = \frac{\bar{P}}{P_a} \tag{4.12}$$

where $T = \sqrt{\frac{\rho h \ell^4}{D}}$. Substituting equations (4.12) into equations (4.1-4.5) and (4.9-4.11) and dropping the stars, we obtain the following system of equations:

$$\frac{\partial^4 w}{\partial x^4} + 2\frac{\partial^4 w}{\partial x^2 \partial y^2} + \frac{\partial^4 w}{\partial y^4} - N\frac{\partial^2 w}{\partial x^2} + \frac{\partial^2 w}{\partial t^2} = -P_{non}\bar{P} + \alpha V_p^2 w + \alpha V_p v_e \tag{4.13}$$

$$\frac{\partial^2 \bar{P}}{\partial x^2} + \frac{\partial^2 \bar{P}}{\partial y^2} = \sigma\left(\frac{\partial \bar{P}}{\partial t} - \frac{\partial w}{\partial t}\right) \tag{4.14}$$

where the nondimensional parameters appearing in equations (4.13) and (4.14) are

$$N_1 = \frac{\hat{N}_1 \ell^2}{D},\ P_{non} = \frac{P_a \ell^4}{dD},\ \sigma = \frac{12\eta_{eff}\ell^2}{d^2 P_a T},\ \alpha = \frac{\epsilon_r \epsilon_0 \ell^4}{d^3 D} \tag{4.15}$$

The nondimensional boundary conditions are

At $y = 0$ and $y = b/\ell$

$$\frac{\partial^2 w}{\partial y^2} + \nu\frac{\partial^2 w}{\partial x^2} = 0 \tag{4.16}$$

$$\frac{\partial^3 w}{\partial y^3} + (2-\nu)\frac{\partial^3 w}{\partial x^2 \partial y} = 0 \tag{4.17}$$

$$\bar{P} = 0 \tag{4.18}$$

At $x = 0$ and $x = 1$

$$w = 0 \tag{4.19}$$

$$\frac{\partial w}{\partial x} = 0 \tag{4.20}$$

$$\frac{\partial \bar{P}}{\partial x} = 0 \tag{4.21}$$

4.1.1 Linear Eigenvalue Problem

To derive the linear damped eigenvalue problem, we let

$$w(x, y, t) = \phi_n(x, y) e^{i\omega_n t} \tag{4.22}$$

$$\bar{P}(x, y, t) = \psi_n(x, y) e^{i\omega_n t} \tag{4.23}$$

where $\phi_n(x, y)$ and $\psi_n(x, y)$ are the nth complex mode shapes of the plate and pressure, respectively, and ω_n is the nth complex nondimensional eigenvalue. Next, we substitute equations (4.22) and (4.23) into equations (4.13-4.14) and (4.16-4.21), drop the forcing terms, and obtain

$$\frac{\partial^4 \phi_n}{\partial x^4} + 2\frac{\partial^4 \phi_n}{\partial x^2 \partial y^2} + \frac{\partial^4 \phi_n}{\partial y^4} - N\frac{\partial^2 \phi_n}{\partial x^2} + P_{non}\psi_n - \alpha V_p^2 \phi_n = \omega_n^2 \phi_n \tag{4.24}$$

$$\frac{\partial^2 \psi_n}{\partial x^2} + \frac{\partial^2 \psi_n}{\partial y^2} = i\omega_n \sigma \left(\psi_n - \phi_n\right) \tag{4.25}$$

At $y = 0$ and $y = b/\ell$

$$\frac{\partial^2 \phi_n}{\partial y^2} + \nu \frac{\partial^2 \phi_n}{\partial x^2} = 0 \tag{4.26}$$

$$\frac{\partial^3 \phi_n}{\partial y^3} + (2 - \nu)\frac{\partial^3 \phi_n}{\partial x^2 \partial y} = 0 \tag{4.27}$$

$$\psi_n = 0 \tag{4.28}$$

At $x = 0$ and $x = 1$

$$\phi_n = 0 \tag{4.29}$$

$$\frac{\partial \phi_n}{\partial x} = 0 \tag{4.30}$$

$$\frac{\partial \psi_n}{\partial x} = 0 \tag{4.31}$$

Equations (4.24-4.31) represent a coupled system of linear partial-differential equations and associated boundary conditions, which can be solved numerically for the complex eigenvalues and mode shapes.

4.1.2 Singular-Perturbation Analysis

A numerical solution of equations (4.24-4.31) using either a finite-difference or a finite-element method might be computationally cumbersome, especially for complex structures. Because $|\omega_n|\,\sigma >> 1$ in equation (4.25), we use a perturbation technique to express the pressure in terms of the deflection. Then, we substitute this expression into equation (4.24) and solve it using a finite-element method.

For large $|\omega_n|\,\sigma$, the boundary-value problem represented by equations (4.25), (4.28), and (4.31) is a singular-perturbation problem (Nayfeh, 1981). Such a case occurs when the gradient of a dependent variable undergoes rapid changes over a very narrow region. In this problem, the pressure changes sharply near the free edges. We use the method of matched asymptotic expansions (Nayfeh, 1981) to derive a uniform approximation to the solution of equations (4.25), (4.28), and (4.31). In this method, an outer expansion, which is valid everywhere in the domain except near the boundaries, is matched with inner expansions, which are valid only near the boundaries. Then, a composite expansion valid everywhere is formed using the outer and inner expansions.

We derive the outer expansion by dividing equation (4.25) by $\omega_n\sigma$, in which case the right-hand side of the resulting equation is very small ($O(\epsilon)$, where $\epsilon = \frac{1}{\omega_n\sigma}$) compared to the left-hand side. Hence, the outer solution is given to the first-order

approximation by

$$\psi_n^o = \phi_n \tag{4.32}$$

where the superscript o denotes an outer solution. This solution satisfies the boundary conditions (4.31) because ϕ_n satisfies similar boundary conditions at $x = 0$ and 1. However, because $\psi_n = 0$ at $y = 0$ and b/ℓ, ψ_n does not satisfy the boundary conditions (4.28) and hence equation (4.32) is not valid in narrow layers near $y = 0$ and b/ℓ. Therefore, we need to determine two inner expansions valid near these boundaries.

We begin by deriving an inner expansion ψ_n^i valid in the boundary layer near $y = 0$. We introduce an inner variable $\xi = \frac{y}{\epsilon^\alpha}$, where α is positive and determined in the course of the analysis. Next, we rewrite equation (4.25) in terms of ξ and note that $\alpha = \frac{1}{2}$ corresponds to the distinguished limit, because it yields the least degenerate form of the resulting equation and allows for a proper matching of the outer and inner solutions (Nayfeh, 1981). Accordingly, we obtain

$$\frac{\partial^2 \psi_n^i}{\partial \xi^2} - i\psi_n^i = -i\phi_n(x, 0) \tag{4.33}$$

From equation (4.28), we conclude that

$$\psi_n^i(x, 0) = 0 \tag{4.34}$$

The solution of equation (4.33) that decays away from $y = 0$ can be expressed as

$$\psi_n^i(x, y) = \phi(x, 0) + c_1 e^{-\frac{1+i}{\sqrt{2}}\xi} \tag{4.35}$$

Imposing the boundary condition (4.34), we obtain

$$c_1 = -\phi(x, 0)$$

To derive an inner solution ψ_n^I near $y = b/\ell$, we introduce an inner variable $\eta = \frac{b/\ell - y}{\sqrt{\epsilon}}$,

repeat the same previous steps, and obtain

$$\psi_n^I(x,y) = \phi_n(x,b/\ell) - \phi_n(x,b/\ell)e^{-\frac{1+i}{\sqrt{2}}\eta} \tag{4.36}$$

Combining the outer solution, equation (4.32), with the two inner solutions, equations (4.35) and (4.36), we obtain the following general solution, also called composite expansion (Nayfeh, 1981), which is valid everywhere:

$$\psi_n(x,y) = \phi_n(x,y) - \phi_n(x,b/\ell)e^{-\frac{1+i}{\sqrt{2}}\eta} - \phi_n(x,0)e^{-\frac{1+i}{\sqrt{2}}\xi} \tag{4.37}$$

Rewriting equation (4.37) in terms of x and y, we obtain

$$\psi_n(x,y) = \phi_n(x,y) - \phi_n(x,b/\ell)e^{-\frac{1+i}{\sqrt{2}}\frac{b/\ell-y}{\sqrt{\epsilon}}} - \phi_n(x,0)e^{-\frac{1+i}{\sqrt{2}}\frac{y}{\sqrt{\epsilon}}} + \ldots \tag{4.38}$$

Equation (4.38) gives an approximate analytical expression for the nth complex pressure mode shape in terms of the nth complex plate mode shape and eigenvalue.

4.2 Results

We substitute equation (4.38) into equation (4.24) and obtain

$$\frac{\partial^4\phi_n}{\partial x^4} + 2\frac{\partial^4\phi_n}{\partial x^2\partial y^2} + \frac{\partial^4\phi_n}{\partial y^4} - N\frac{\partial^2\phi_n}{\partial x^2} + P_{non}\Big[\phi_{n_0}(x,y) - \phi_{n_0}(x,b/\ell)e^{-\frac{1+i}{\sqrt{2}}\frac{b/\ell-y}{\sqrt{\epsilon}}} - \phi_{n_0}(x,0)e^{-\frac{1+i}{\sqrt{2}}\frac{y}{\sqrt{\epsilon}}}\Big] - \alpha V_p^2\phi_n = \omega_n^2\phi_n \tag{4.39}$$

Equation (4.39) and the boundary conditions, equations (4.26), (4.27), (4.29), and (4.30) represent a linear distributed-parameter system for the dynamic behavior of the microplate under the coupled effect of squeeze-film damping, the structural forces, and the linear electrostatic forces. We solve this system for the nth complex mode shape and eigenvalue using a finite-element method (Reddy, 1993). We mesh the plate using a nonconforming rectangular element of four nodes with the three unknowns (w, $\frac{\partial w}{\partial x}$, $\frac{\partial w}{\partial y}$) at each node. We use the Hermite functions as basis functions in the finite-element formulation.

The real part of the complex eigenvalue gives the natural frequency of the microplate, whereas the imaginary part yields its damping. The quality factor can be related to the imaginary and real parts of the eigenvalue by recalling the relation between the damping coefficient and the quality factor for a spring-damper-mass system; that is,

$$Q = \frac{\text{Re}(\omega_n)}{2\text{Imag}(\omega_n)} \tag{4.40}$$

where Re and Imag denote the real and imaginary parts, respectively.

Next, we calculate the natural frequencies and quality factors of electrically actuated microplates, employed as transducers in resonant sensors, under various gas pressures. We consider first the resonant microplate of Legtenberg and Tilmans (1994) with $\ell = 310\mu m$, $h = 1.5\mu m$, $b = 100\mu m$, $d = 1.18\mu m$, $E = 166GPa$, axial load per unit length of 0.0009 $Newton$, and $V_p = 2V$. The resonator is encapsulated in a cavity at very low pressure. They reported an experimental value of the quality factor near vacuum $Q_{vacuum} = 18500$ at $P_a = 6 \times 10^{-6} mbar$. We use this value with equation (2.1) to account for the structural damping of the microplate. In the following figures, we use a mesh of 24×8 elements, which yielded acceptable convergence.

In Figure 4.2, we show the calculated nondimensional fundamental natural frequency ω_{1_0} for various values of the encapsulation pressure P_a. We note that ω_{1_0} increases slightly with increasing pressure, an indication of a low spring effect, as expected for this range of pressure.

Figure 4.3 shows a comparison of the calculated quality factor Q (stars) to the experimental data (triangles) of Legtenberg and Tilmans (1994). The agreement is excellent except for one data point at $P_a = 6 \times 10^{-5} mbar$. The reason for this discrepancy is not clear at the present time, especially there is a large drop in the experimental value as P_a increases slightly. More experiments are needed in the interval $10^{-5} mbar \leq P_a \leq 10^{-1} mbar$.

Figures 4.4 and 4.5 show the first mode shape of the microplate and the corresponding pressure distribution, respectively, at $P_a = 1\ mbar$. We calculate the mode

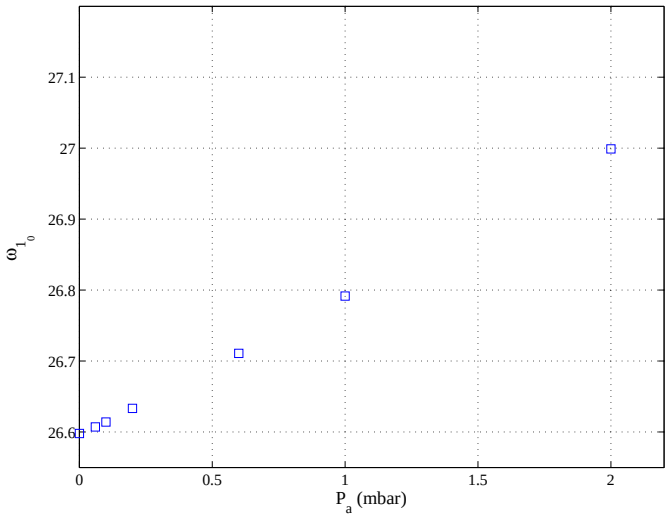

Figure 4.2: Variation of the calculated nondimensional fundamental natural frequency for a microplate of length $310\mu m$ with the encapsulation pressure.

shape by taking the magnitude of the corresponding complex mode shape, which is in this case dominated by its real part.

Next, we consider the resonant microplate of Legtenberg and Tilmans (1994) with length $210\mu m$ and $V_p = 6V$. The reported experimental value of the quality factor near vacuum is $Q_{vacuum} = 18000$ at $P_a = 6 \times 10^{-6} mbar$ (1994). The rest of the specifications are the same as those of the first microbeam of length $310\mu m$. Figure 4.6 shows a comparison of the calculated quality factor Q (stars) to the experimental data (triangles) of Legtenberg and Tilmans (1994). The agreement is also good. Again, more experiments are needed in the range $10^{-4} mbar \leq P_a \leq 10^{-1} mbar$ to better understand the model capability and limitations.

Figures 4.7 and 4.8 show the first five mode shapes of the microplate and their corresponding pressure mode shapes, respectively, at $V_p = 6V$ and $P_a = 1 mbar$. The first five natural frequencies are $\omega_{1_0} = 24.21$, $\omega_{2_0} = 38.26$, $\omega_{3_0} = 63.92$, $\omega_{4_0} = 86.35$, and $\omega_{5_0} = 118.54$. Their corresponding quality factors are $Q = 615.94$, 1487.70, 5094.20, 5773.10, and 10458.0. For the even modes (antisymmetric modes around $y = \frac{b}{2\ell}$), equation (4.38) fails to predict the pressure distribution because the boundary-layer terms cancel each other. To overcome this problem, we use the symmetry of the

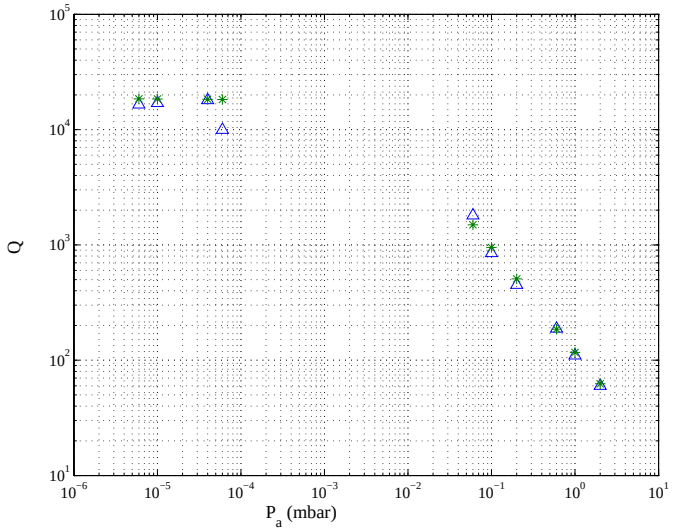

Figure 4.3: Comparison of the calculated quality factor (stars) for a microplate of length $310\mu m$ to the experimental data (triangles) of Legtenberg and Tilmans (1994).

plate about $y = \frac{b}{2\ell}$ and simulate half of the plate. The results are then image-mirrored around the axis of symmetry with a negative sign to take care of the antisymmetry of the mode.

4.3 Other Boundary Conditions

The analysis presented so far is for plates with clamped edges on two opposite sides and free edges on the other sides. Here, we investigate the applicability of the perturbation approach to other boundary conditions.

The perturbation approach depends primarily on the fact that ($\epsilon = \frac{1}{\sigma\omega_{n_0}} << 1$). Some MEMS devices (Xu and Smith, 1995) employ a cantilever plate that oscillates in low pressure. Because the fundamental natural frequencies of cantilevers are relatively small (Leissa, 1969), ϵ is not $<< 1$ in such devices, and hence the current perturbation approach does not apply. The same conclusion holds for torsional micromirrors, which oscillate at very low frequencies, near $1k$Hz (Kubby et al., 1998). On the other hand, plates with one free edge and the other edges clamped have high natural frequencies, and hence the perturbation approach is applicable. In such cases, there is only one

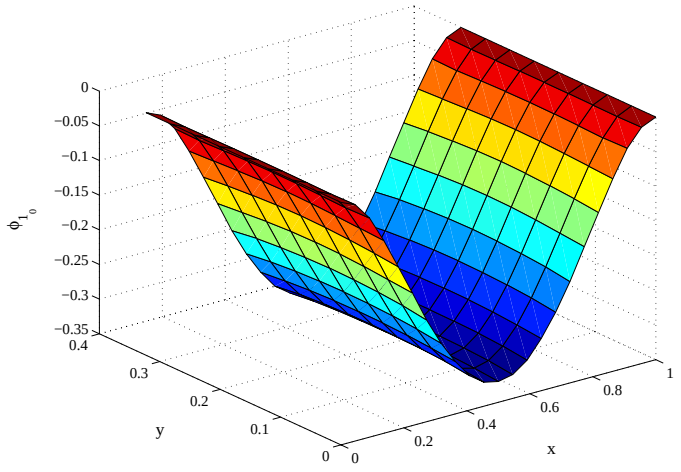

Figure 4.4: The first mode shape of a microplate of length $310\mu m$.

boundary layer at the free edge. For a plate with a free edge at $y = b/\ell$, the pressure distribution can be related to the nth mode shape of the plate by

$$\psi_n(x,y) = \phi_n(x,y) - \phi_n(x,b/\ell)e^{-\frac{1+i}{\sqrt{2}}\frac{b/\ell - y}{\sqrt{\epsilon}}} \tag{4.41}$$

4.3.1 Perturbation Analysis

Fully clamped plates also have very high natural frequencies. Such plates are widely used in various MEMS devices, such as capacitive pressure sensors (Pons et al., 1991). The pressure boundary conditions for a fully clamped plate demand zero flux at all edges; that is,

$$\frac{\partial \psi_n(x,0)}{\partial y} = \frac{\partial \psi_n(x,b/\ell)}{\partial y} = 0 \tag{4.42}$$

$$\frac{\partial \psi_n(0,y)}{\partial x} = \frac{\partial \psi_n(1,y)}{\partial x} = 0 \tag{4.43}$$

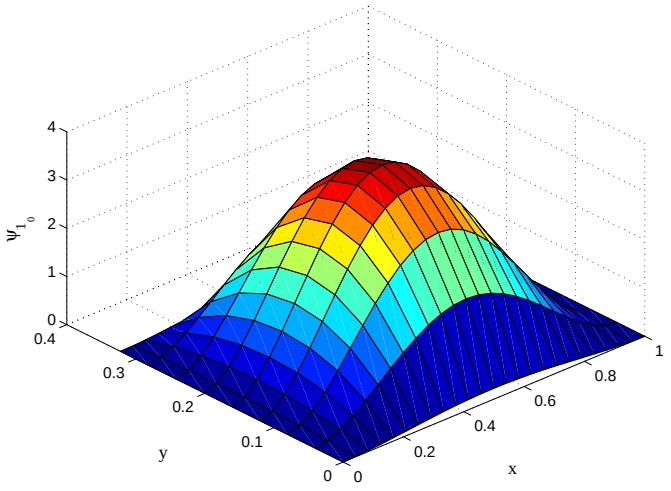

Figure 4.5: The pressure distribution associated with the first mode shape of Figure 4.4.

and the structural boundary conditions are

$$\frac{\partial \phi_n(x,0)}{\partial y} = \frac{\partial \phi_n(x,b/\ell)}{\partial y} = 0 \tag{4.44}$$

$$\frac{\partial \phi_n(0,y)}{\partial x} = \frac{\partial \phi_n(1,y)}{\partial x} = 0 \tag{4.45}$$

$$\phi_n(x,0) = \phi_n(x,b/\ell) = 0 \tag{4.46}$$

$$\phi_n(0,y) = \phi_n(1,y) = 0 \tag{4.47}$$

It follows from equations (4.42-4.45) that there are no boundary layers to first order in this case because the pressure boundary conditions are satisfied to first order by the outer expansion, equation (4.32). Hence, to the first approximation, the pressure has a pure spring-force effect. To derive an expression for the quality factor, we need to carry out the expansion to higher order. To this end, we apply the method of strained parameters (Nayfeh, 1981) and seek a first-order solution to equations (4.24, 4.25) and

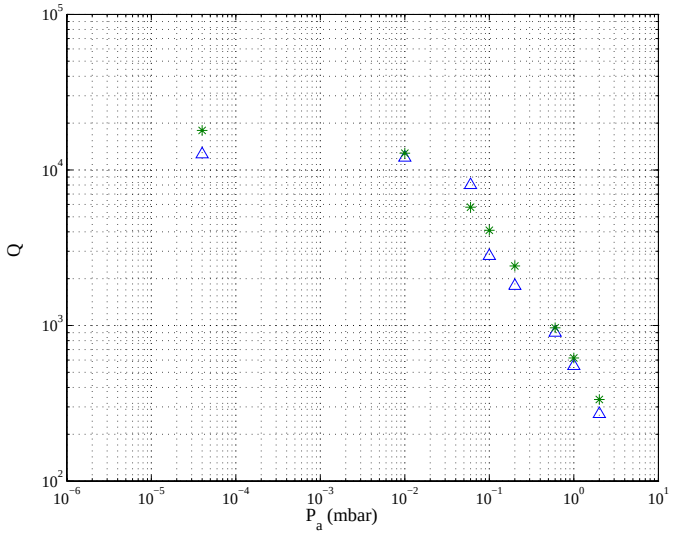

Figure 4.6: Comparison of the calculated quality factor (stars) for a microplate of length $210\mu m$ to the experimental data (triangles) of Legtenberg and Tilmans (1994).

(4.42-4.47) in the form

$$\phi_n = \phi_{n_0} + \epsilon\phi_{n_1} + ... \tag{4.48}$$

$$\psi_n = \psi_{n_0} + \epsilon\psi_{n_1} + ... \tag{4.49}$$

$$\omega_n = \omega_{n_0} + \epsilon\omega_{n_1} + ... \tag{4.50}$$

Substituting equations (4.48-4.50) into equations (4.24, 4.25) and (4.42-4.47) and equating coefficients of like power of ϵ, we obtain

$\underline{O(\epsilon^0)}$

$$\psi_{n_0} = \phi_{n_0} \tag{4.51}$$

$$\begin{aligned}\mathcal{L}(\phi_{n_0}, \psi_{n_0}) &= \frac{\partial^4\phi_{n_0}}{\partial x^4} + 2\frac{\partial^4\phi_{n_0}}{\partial x^2\partial y^2} + \frac{\partial^4\phi_{n_0}}{\partial y^4} - N\frac{\partial^2\phi_{n_0}}{\partial x^2} + P_{non}\psi_{n_0} - \alpha V_p^2\phi_{n_0} \\ &= \omega_{n_0}^2\phi_{n_0}\end{aligned} \tag{4.52}$$

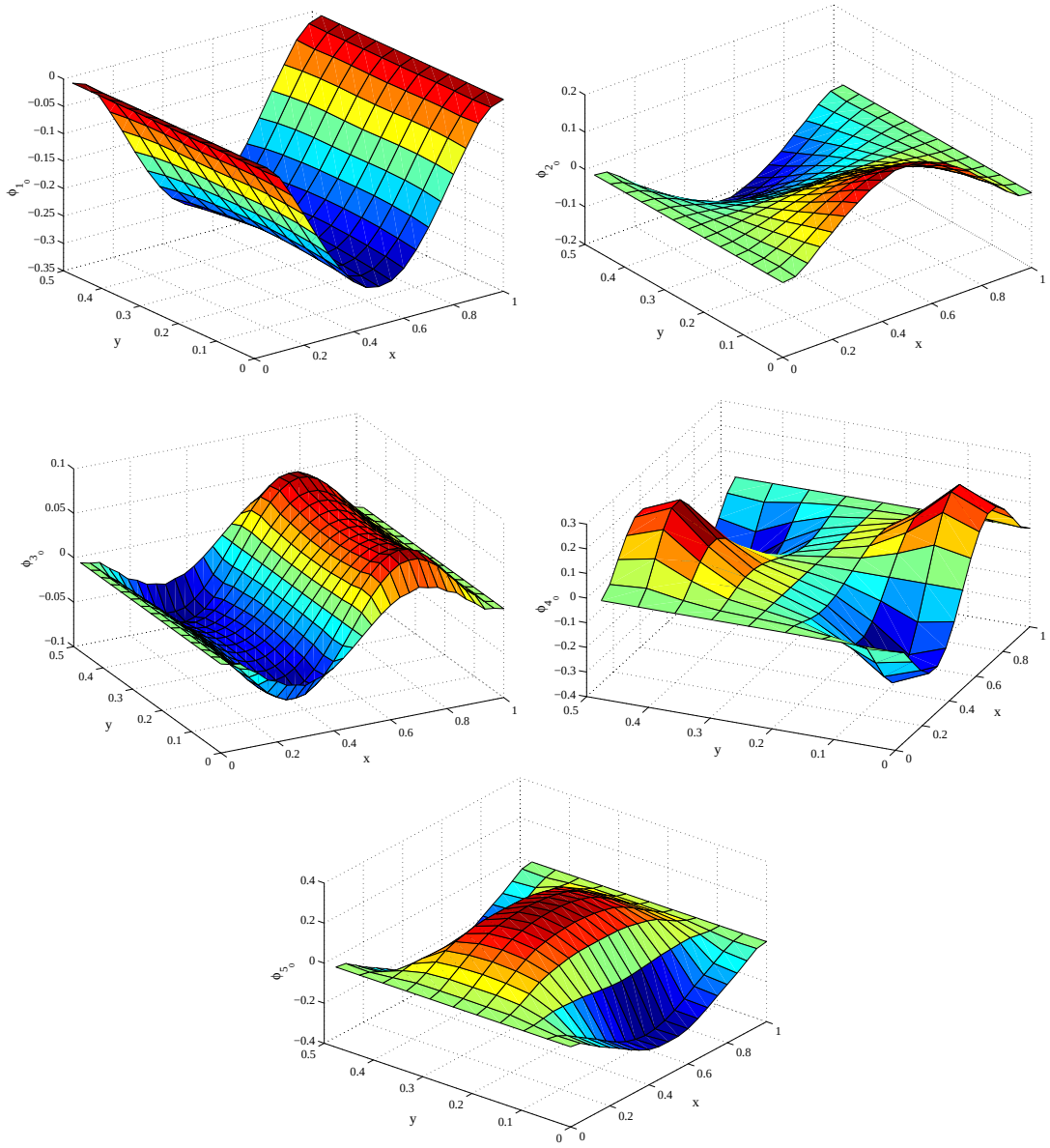

Figure 4.7: The first five mode shapes of a microplate of length $210\mu m$.

$\underline{O(\epsilon^1)}$

$$\psi_{n_1} = -i\left(\frac{\partial^2 \phi_{n_0}}{\partial x^2} + \frac{\partial^2 \phi_{n_0}}{\partial y^2}\right) + \phi_{n_1} \tag{4.53}$$

$$\mathcal{L}(\phi_{n_1}, \psi_{n_1}) - \omega_{n_0}^2 \phi_{n_1} = 2\omega_{n_0}\omega_{n_1}\phi_{n_0} \tag{4.54}$$

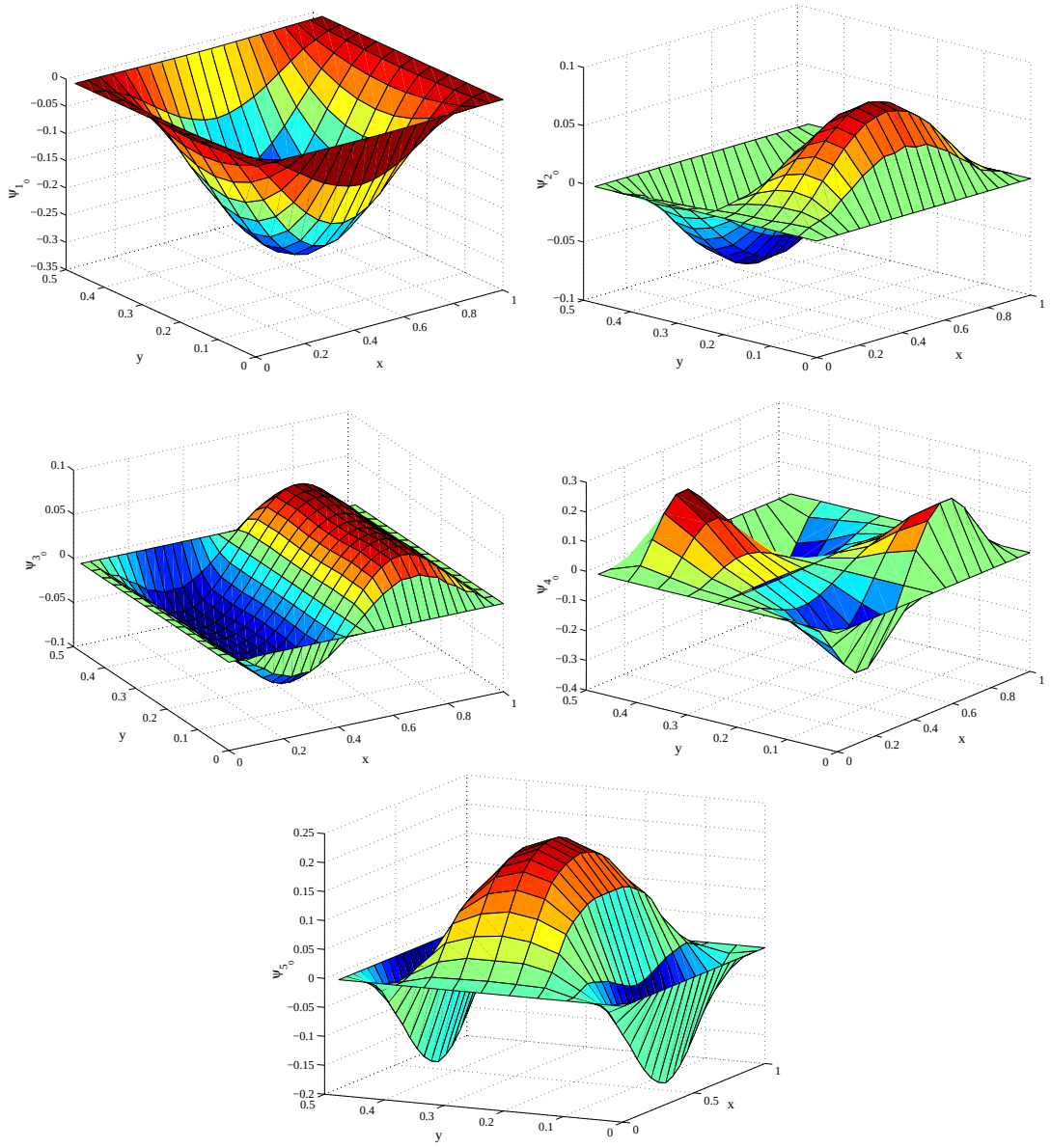

Figure 4.8: The first five pressure mode shapes corresponding to the deflection mode shapes of Figure 4.7.

The boundary conditions for equations (4.52) and (4.54) are

$\underline{y = 0 \text{ and } y = b/\ell}$

$$\phi_{n_j} = 0 \tag{4.55}$$

$$\frac{\partial \phi_{n_j}}{\partial y} = 0 \tag{4.56}$$

$\underline{x = 0 \text{ and } x = 1}$

$$\phi_{n_j} = 0 \tag{4.57}$$

$$\frac{\partial \phi_{n_j}}{\partial x} = 0 \tag{4.58}$$

where $j = 0, 1$.

Substituting equation equation (4.51) into equation (4.52) and equations (4.51) and (4.53) into equation (4.54), we obtain

$$\begin{aligned} &\frac{\partial^4 \phi_{n_0}}{\partial x^4} + 2\frac{\partial^4 \phi_{n_0}}{\partial x^2 \partial y^2} + \frac{\partial^4 \phi_{n_0}}{\partial y^4} - N\frac{\partial^2 \phi_{n_0}}{\partial x^2} + P_{non}\phi_{n_0} - \alpha V_p^2 \phi_{n_0} \\ &\qquad - \omega_{n_0}^2 \phi_{n_0} = 0 \end{aligned} \tag{4.59}$$

$$\begin{aligned} &\frac{\partial^4 \phi_{n_1}}{\partial x^4} + 2\frac{\partial^4 \phi_{n_1}}{\partial x^2 \partial y^2} + \frac{\partial^4 \phi_{n_1}}{\partial y^4} - N\frac{\partial^2 \phi_{n_1}}{\partial x^2} + P_{non}\phi_{n_1} - \alpha V_p^2 \phi_{n_1} - \omega_{n_0}^2 \phi_{n_1} \\ &\qquad = 2\omega_{n_0}\omega_{n_1}\phi_{n_0} + iP_{non}\left(\frac{\partial^2 \phi_{n_0}}{\partial x^2} + \frac{\partial^2 \phi_{n_0}}{\partial y^2}\right) \end{aligned} \tag{4.60}$$

We note that, the homogeneous problem governing ϕ_{n1} is the same as the problem governing ϕ_{n0} and because the latter has nontrivial solutions, the nonhomogeneous problem governing ϕ_{n1} has a solution only if the right-hand side of equation (4.60) is orthogonal to every solution of the adjoint homogeneous problem governing ϕ_{n_1} (solvability condition (Nayfeh, 1981)). Because the problem is self-adjoint, the solvability condition demands that the right-hand side of equation (4.60) be orthogonal to ϕ_{n_0}; that is,

$$\omega_{n_1} = \frac{-iP_{non}\int_0^1 \int_0^{b/\ell} \phi_{n_0}\left(\frac{\partial^2 \phi_{n_0}}{\partial x^2} + \frac{\partial^2 \phi_{n_0}}{\partial y^2}\right) dxdy}{2\omega_{n_0}\int_0^1 \int_0^{b/\ell} \phi_{n_0}^2 dxdy} \tag{4.61}$$

Equation (4.61) gives the imaginary part of the complex natural frequency, which yields the damping of the system.

4.3.2 Results

Figure 4.9 shows a comparison of the calculated fundamental natural frequencies and quality factors for a fully clamped microplate (stars) with those for a clamped-free-clamped-free plate (circles). We used the same device specifications of Figure 4.6 except that the DC loading is set equal to zero. We note that the fully clamped plate has a higher fundamental natural frequency and a higher quality factor (lower damping), as expected because the perturbation analysis for this case predicts a pure spring force to first order and the damping is of higher order. We also note that the shift in the resonance frequency at high pressure is higher for the clamped-free-clamped-free plate. Thus, fully clamped plates have higher resolution and are more stable as transducers than clamped-free-clamped-free plates for the same operating conditions. However, clamped-free-clamped-free plates seem to be more sensitive to external disturbances.

4.4 Clamped Annular and Circular Plates

The perturbation analysis for rectangular plates can also be extended to other geometries provided that ($\epsilon = \frac{1}{\sigma\omega_{n_0}} << 1$). In this section, we outline a theoretical derivation for the damping coefficient ω_{n_1} for clamped annular and circular plates. These plates have been receiving increasing interest in the MEMS community, especially in micropump applications (Saif et al., 1999).

We consider a clamped annular microplate, of outer radius R_1 and inner radius R_2, actuated by an electric load composed of a small DC component V_p and an AC component $v_e(t)$ and subject to a gas pressure $\bar{P}(r)$ per unit area. Assuming small strains and displacements and axisymmetric bending ($w = w(r,t)$), we obtain the following linear equation of motion (Leissa, 1969) governing the transverse deflection

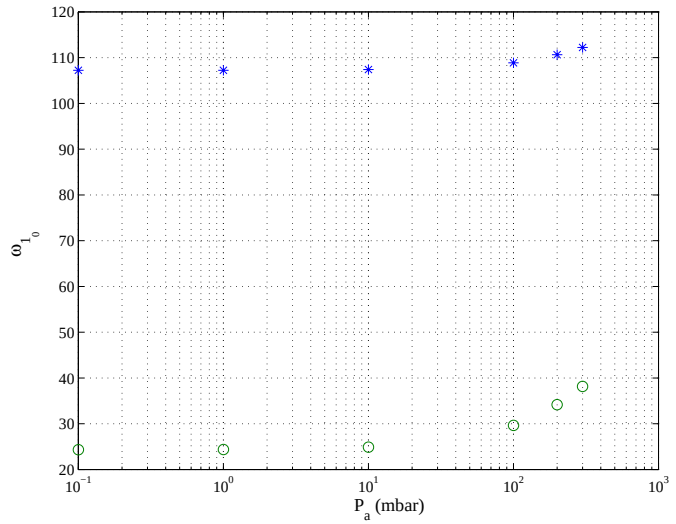

(a) Fundamental natural frequency.

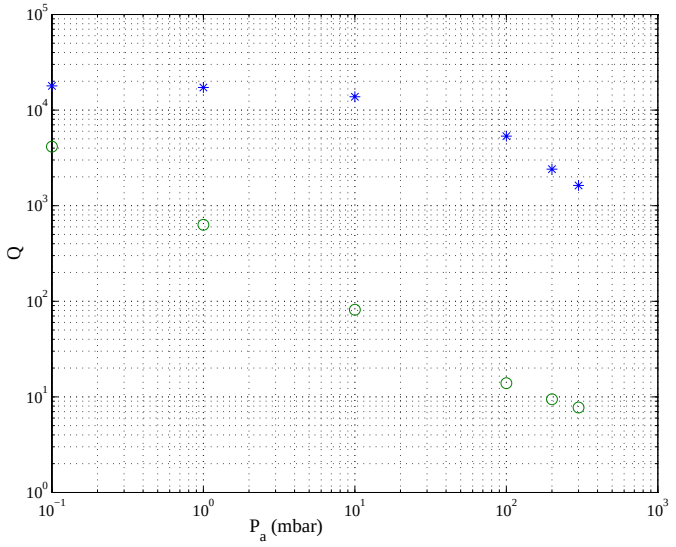

(b) Quality factor.

Figure 4.9: Comparison of the calculated fundamental natural frequencies and quality factors of a fully clamped microplate (stars) with those of a clamped-free-clamped-free plate (circles).

of the microplate:

$$D\left[\frac{1}{r}\frac{\partial}{\partial r}\left(r\frac{\partial}{\partial r}\right)\right]\left[\frac{1}{r}\frac{\partial}{\partial r}\left(r\frac{\partial w}{\partial r}\right)\right]+\rho h\frac{\partial^2 w}{\partial t^2}=-\bar{P}+\frac{\epsilon_0\epsilon_r V_p v_e}{d^2}+\frac{\epsilon_0\epsilon_r V_p^2}{d^3}w \tag{4.62}$$

The rest of the parameters are defined in Section 4.1. The plate boundary conditions are

$$w(R_1,t) = \frac{\partial w}{\partial r}(R_1,t) = 0 \tag{4.63}$$

$$w(R_2,t) = \frac{\partial w}{\partial r}(R_2,t) = 0 \tag{4.64}$$

The pressure $\bar{P}$ is governed by the following axisymmetric polar form of the Reynolds equation:

$$\frac{\partial}{\partial r}\left(rH^3P\frac{\partial P}{\partial r}\right) = 12\eta r\left(H\frac{\partial P}{\partial t} + P\frac{\partial H}{\partial t}\right) \tag{4.65}$$

subject to the boundary conditions

$$\frac{\partial \bar{P}}{\partial r}(R_1,t) = 0 \tag{4.66}$$

$$\frac{\partial \bar{P}}{\partial r}(R_2,t) = 0 \tag{4.67}$$

Following a procedure similar to that used for fully clamped rectangular plates, we obtain the damping coefficient

$$\omega_{n_1} = \frac{-iP_{non}\int_{R_2/R_1}^{R_1}\phi_{n_0}\left[\frac{\partial}{\partial r}\left(r\frac{\partial\phi_{n_0}}{\partial r}\right)\right]dr}{2\omega_{n_0}\int_{R_2/R_1}^{R_1} r\phi_{n_0}^2 dr} \tag{4.68}$$

where ω_{n_0} and ϕ_{n_0} are the nth natural frequency and mode shape of the plate, respectively. The pressure distribution is given to first order by equation (4.35). For clamped circular plates, R_2 is set equal to zero in equation (4.68). Also, in calculating ω_{n_0} and ϕ_{n_0}, the boundary conditions, equations (4.63) and (4.66), are replaced with conditions that require finite values of w and $\bar{P}$ at $r = 0$.

Chapter 5

A Model of Microplates under the Effect of Squeeze-Film Damping and Large Electrostatic Forces

In Chapter 4, we presented a model utilizing a linear plate equation coupled with the compressible Reynolds equation to simulate the dynamic behavior of microstructures under the effect of squeeze-film damping and small DC loading. However, the model does not apply for plates actuated by large electrostatic forces, up to the pull-in instability, or exhibiting large deflections. Such problems are of significant importance for many MEMS applications, such as MEMS-based projection displays, in which a microstructure is electrostatically actuated beyond the pull-in instability under the effect of squeeze-film damping to diffract or reflect incident lights (Senturia, 2000).

In this chapter, we present a model to simulate accurately the dynamics of microplates under the effect of squeeze-film damping and large electrostatic forces using the compressible Reynolds equation coupled with the von Kármán plate equations. We utilize the beam model in Chapter 3 to calculate the static deflection of the microplate under a DC electrostatic force. We then derive analytical expressions for the pressure

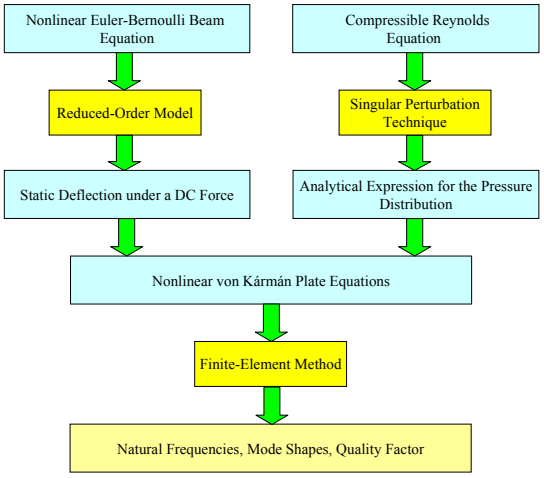

Figure 5.1: A schematic for a computationally efficient approach to simulate microplates under the coupled effect of electrostatic, fluidic, and mechanical forces.

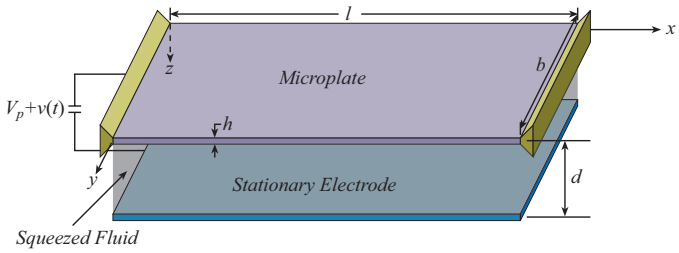

Figure 5.2: Electrically actuated microplate.

distribution in terms of the plate mode shapes around the deflected position, and hence eliminate the pressure as a variable in the solution procedure. We substitute the static deflection and the analytical expression of the pressure in the dynamic von Kármán plate equations, linearized around the deflected position, and then solve the resulting equations using a finite-element method. Figure 5.1 shows a schematic drawing for the procedure of the proposed approach.

5.1 Problem Formulation

We consider a microplate, Figure 5.2, actuated by a DC electrostatic load V_p and subject to a net pressure force $\bar{P}(x, y, t)$ per unit area due to squeeze-film damping.

The electrostatic force deflects the microplate to a new equilibrium position, around which the microplate oscillates. We use the dynamic version of the von Kármán plate equations to represent the microplate motion. Hence, we write the equations of motion as (Chia, 1980; Nayfeh, 2000)

$$u_{,xx} + d_1 u_{,yy} + d_2 v_{,xy} = -w_{,x}(w_{,xx} + d_1 w_{,yy}) - d_2 w_{,y} w_{,xy} \tag{5.1}$$

$$v_{,yy} + d_1 v_{,xx} + d_2 u_{,xy} = -w_{,y}(w_{,yy} + d_1 w_{,xx}) - d_2 w_{,x} w_{,xy} \tag{5.2}$$

$$\begin{aligned} &D\nabla^4 w + \rho h w_{,tt} - \hat{N}_1 w_{,xx} = d_3 \Big[(u_{,x} + \frac{1}{2} w_{,x}^2)(w_{,xx} + \nu w_{,yy}) \\ &+ (v_{,y} + \frac{1}{2} w_{,y}^2)(w_{,yy} + \nu w_{,xx}) + (1-\nu) w_{,xy}(u_{,y} + w_{,x} w_{,y} \\ &+ v_{,x}) \Big] - \bar{P} + \frac{1}{2} \epsilon_0 \epsilon_r \frac{V_p^2}{(d-w)^2} \end{aligned} \tag{5.3}$$

where x and y are the positions along the plate length and width, respectively, u, v, and w are the displacements in the x, y, and z directions, respectively, t is time, ρ is the mass density, d is the gap width, $D = \frac{Eh^3}{12(1-\nu^2)}$ is the flexural rigidity, h is the microplate thickness, E is Young's modulus, ν is Poisson's ratio, $\hat{N}_1$ is the in-plane force per unit length, ϵ_0 is the dielectric constant of vacuum, and ϵ_r is the relative dielectric constant of the gap medium to an air gap. The symbol ∇^4 denotes the biharmonic operator ($\nabla^4 = w_{,xxxx} + 2w_{,xxyy} + w_{,yyyy}$), where a comma denotes partial differentiation with respect to the corresponding coordinate. The parameters d_i are defined as

$$d_1 = \frac{1}{2}(1-\nu), \qquad d_2 = \frac{1}{2}(1+\nu), \qquad d_3 = \frac{Eh}{1-\nu^2} \tag{5.4}$$

The last term in equation (5.3) represents an approximation of the parallel-plate electrostatic force assuming complete overlapping of the microplate area and the stationary electrode. The inertia terms in equations (5.1) and (5.2) have been dropped because the in-plane natural frequencies are much larger than the transverse frequencies.

The boundary conditions associated with equations (5.1-5.3) are

Free edges at $y = 0$ and $y = b$

$$v_{,y} + \nu u_{,x} + \frac{1}{2}(w_{,y}^2 + \nu w_{,x}^2) = 0 \tag{5.5}$$

$$u_{,y} + v_{,x} + w_{,x} w_{,y} = 0 \tag{5.6}$$

$$w_{,yy} + \nu w_{,xx} = 0 \tag{5.7}$$

$$w_{,yyy} + (2 - \nu) w_{,xxy} = 0 \tag{5.8}$$

Clamped edges at $x = 0$ and $x = \ell$

$$u = 0 \tag{5.9}$$

$$v = 0 \tag{5.10}$$

$$w = 0 \tag{5.11}$$

$$w_{,x} = 0 \tag{5.12}$$

The microplate is deflected by a DC electrostatic force, which varies along the length of the plate and is uniform across its width. Because of the symmetric nature of the electrostatic force and the boundary conditions, the plate undergoes cylindrical bending; that is, no variations across its width. Setting the variations with t and y in equations (5.1-5.3) equal to zero, we obtain the following equations governing the static deflection of the plate:

$$u_{s,xx} = -w_{s,x} w_{s,xx} \tag{5.13}$$

$$D w_{s,xxxx} - \hat{N}_1 w_{s,xx} = d_3 w_{s,xx}(u_{s,x} + \frac{1}{2} w_{s,x}^2) + \frac{1}{2}\epsilon_0 \epsilon_r b \frac{V_p^2}{(d - w_s)^2} \tag{5.14}$$

where u_s and w_s are the static in-plane and bending displacements, respectively. Next, we eliminate u_s and rewrite equations (5.13) and (5.14) as

$$\frac{EI}{1 - \nu^2} w_{s,xxxx} = \left(\frac{EA}{2(1 - \nu^2)\ell} \int_0^\ell w_{s,x}^2 dx + b\hat{N}_1 \right) w_{s,xx} + \frac{1}{2}\epsilon_0 \epsilon_r b \frac{V_p^2}{(d - w_s)^2} \tag{5.15}$$

The associated boundary conditions are

$$w_s = 0 \text{ and } w_{s,x} = 0 \text{ at } x = 0 \text{ and } x = \ell \tag{5.16}$$

The integral term in equation (5.15) represents the in-plane strain along the length of the microplate due to the immovable edges (mid-plane stretching). Equations (5.15) and (5.16) can be solved using a shooting technique (Younis, 2001; Younis et al., 2002; Abdel-Rahman et al., 2002) or a reduced-order model (Younis et al., 2003). The in-plane displacement u_s is related to w_s by

$$u_{s,x} = -\frac{1}{2}w_{s,x}^2 + \frac{1}{2\ell}\int_0^\ell w_{s,x}^2 dx$$

The pressure is governed by the nonlinear Reynolds equation

$$\frac{\partial}{\partial x}\left(H^3 P P_{,x}\right) + \frac{\partial}{\partial y}\left(H^3 P P_{,y}\right) = 12\eta_{eff}\left(H P_{,t} + P H_{,t}\right) \tag{5.17}$$

where H is the variable distance between the two plates, P is the total pressure in the gap, and η_{eff} is the effective viscosity of the fluid in the gap, which accounts for the rarefied gas effect by being dependent on the Knudsen number. Here we use the model of Veijola et al. (1995). The pressure boundary conditions are zero flux at the clamped edges and trivial pressure at the free edges.

Next, we express the microplate response as the sum of the static components $w_s(x)$ and $u_s(x)$ and the dynamic components $w_d(x,y,t)$ and $u_d(x,y,t)$; that is,

$$w(x,y,t) = w_s(x) + w_d(x,y,t) \tag{5.18}$$

$$u(x,y,t) = u_s(x) + u_d(x,y,t) \tag{5.19}$$

Also, we consider small dynamic deflections and pressure variation and express H and

P as

$$H(x,y,t) = d - w_s(x) - w_d(x,y,t) \tag{5.20}$$

$$P(x,y,t) = P_a + \bar{P}(x,y,t) \tag{5.21}$$

where P_a is the static pressure. Substituting equations (5.18-5.21) into equations (5.1-5.3), (5.5-5.12), and (5.17), using equations (5.13) and (5.14) to cancel the equilibrium terms, and retaining linear terms, we obtain the following linearized system of equations and boundary conditions governing the motion of an initially deflected microplate under squeeze-film damping:

$$D\nabla^4 w_d + \rho h w_{d,tt} - \hat{N}_1 w_{d,xx} - d_3[u_{s,x}w_{d,xx} + \nu u_{s,x}w_{d,yy} + u_{d,x}w_{s,xx} + \frac{1}{2}w_{s,x}^2 w_{d,xx} + \frac{\nu}{2}w_{s,x}^2 w_{d,yy} + w_{s,x}w_{s,xx}w_{d,x}] = \frac{\epsilon_r \epsilon_0 V_p^2 w_d}{(d-w_s)^3} - \bar{P} \tag{5.22}$$

$$u_{d,xx} + w_{d,x}w_{s,xx} + w_{s,x}w_{d,xx} + \nu v_{,xy} + \frac{1}{2}(1-\nu)(u_{d,yy} + v_{,xy} + w_{s,x}w_{d,yy}) = 0 \tag{5.23}$$

$$v_{,yy} + \nu(u_{d,xy} + w_{s,x}w_{d,xy}) + \frac{1}{2}(1-\nu)(u_{d,xy} + v_{,xx} + w_{s,x}w_{d,xy} + w_{d,y}w_{s,xx}) = 0 \tag{5.24}$$

$$\frac{\partial}{\partial x}\left[(d-w_s)^3 P_a \bar{P}_{,x}\right] + \frac{\partial}{\partial y}\left[(d-w_s)^3 P_a \bar{P}_{,y}\right] = 12\eta_{eff}\left[(d-w_s)\bar{P}_{,t} - P_a w_{d,t}\right] \tag{5.25}$$

At $y = 0$ and $y = b$

$$v_{,y} + \nu u_{d,x} + \nu w_{s,x} w_{d,x} = 0 \tag{5.26}$$

$$u_{d,y} + v_{,x} + w_{s,x} w_{d,y} = 0 \tag{5.27}$$

$$w_{d,yy} + \nu w_{d,xx} = 0 \tag{5.28}$$

$$w_{d,yyy} + (2 - \nu) w_{d,xxy} = 0 \tag{5.29}$$

$$\bar{P}_{,x} = 0 \tag{5.30}$$

At $x = 0$ and $x = \ell$

$$u_d = 0 \tag{5.31}$$

$$v = 0 \tag{5.32}$$

$$w_d = 0 \tag{5.33}$$

$$w_{d,x} = 0 \tag{5.34}$$

$$\bar{P} = 0 \tag{5.35}$$

In the absence of the static deflection, equation (5.22) is decoupled from equations (5.23) and (5.24). In other words, the transverse vibrations are independent from the in-plane motions (Nayfeh and Younis, 2004), which is the case studied in Chapter 4. On the other hand, in the presence of the static deflection, the transverse motion is coupled with the in-plane motions. This is the case considered in this chapter.

For convenience, we introduce the nondimensional variables denoted by astrikes

$$\begin{aligned} &x^* = \frac{x}{\ell}, \qquad y^* = \frac{y}{\ell}, \qquad t^* = t\sqrt{\frac{D}{\rho h \ell^4}}, \\ &\bar{P}^* = \frac{\bar{P}}{P_a}, \qquad w_s^* = \frac{w_s}{d}, \qquad w_d^* = \frac{w_d}{d}, \\ &u_s^* = \frac{u_s}{d}, \qquad u_d^* = \frac{u_d}{d}, \qquad v^* = \frac{v}{d} \end{aligned} \tag{5.36}$$

Substituting equations (5.36) into equations (5.22-5.35) and dropping the astrikes, we

obtain the following nondimensional distributed-parameter system:

$$\nabla^4 w_d + w_{d,tt} - N w_{d,xx} - \alpha_1 u_{d,x} w_{s,xx} - \alpha_2 w_{d,xx} w_{s,x}^2 - \alpha_3 v_{,y} w_{s,xx} - \alpha_4 w_{d,yy} w_{s,x}^2 - \alpha_1 u_{s,x} w_{d,xx} - \alpha_3 u_{s,x} w_{d,yy} - 2\alpha_2 w_{s,x} w_{s,xx} w_{d,x} = \alpha_5 \frac{V_p^2 w_d}{(1-w_s)^3} - P_{non} \bar{P} \tag{5.37}$$

$$u_{d,xx} + \alpha_6 w_{d,x} w_{s,xx} + \alpha_6 w_{s,x} w_{d,xx} + \nu v_{,xy} + \frac{1}{2}(1-\nu)(u_{d,yy} + v_{,xy} + \alpha_6 w_{s,x} w_{d,yy}) = 0 \tag{5.38}$$

$$v_{,yy} + \nu u_{d,xy} + \nu \alpha_6 w_{s,x} w_{d,xy} + \frac{1}{2}(1-\nu)(u_{d,xy} + v_{,xx} + \alpha_6 w_{s,x} w_{d,xy} + \alpha_6 w_{d,y} w_{s,xx}) = 0 \tag{5.39}$$

$$\frac{\partial}{\partial x}\left[(1-w_s)^3 \bar{P}_{,x}\right] + \frac{\partial}{\partial y}\left[(1-w_s)^3 \bar{P}_{,y}\right] = \sigma\left[(1-w_s)\bar{P}_{,t} - w_{d,t}\right] \tag{5.40}$$

At $y = 0$ and $y = b/\ell$

$$v_{,y} + \nu u_{d,x} + \nu \alpha_6 w_{s,x} w_{d,x} = 0 \tag{5.41}$$

$$u_{d,y} + v_{,x} + \alpha_6 w_{s,x} w_{d,y} = 0 \tag{5.42}$$

$$w_{d,yy} + \nu w_{d,xx} = 0 \tag{5.43}$$

$$w_{d,yyy} + (2-\nu) w_{d,xxy} = 0 \tag{5.44}$$

$$\bar{P}_{,x} = 0 \tag{5.45}$$

At $x = 0$ and $x = 1$

$$u_d = 0 \tag{5.46}$$

$$v = 0 \tag{5.47}$$

$$w_d = 0 \tag{5.48}$$

$$w_{d,x} = 0 \tag{5.49}$$

$$\bar{P} = 0 \tag{5.50}$$

The nondimensional parameters appearing in equations (5.37-5.42) are

$$\begin{aligned} &\sigma = \frac{12\eta_{eff}\ell^2}{d^2 P_a T}, \quad N = \frac{\hat{N}_1 \ell^2}{D}, \quad P_{non} = \frac{P_a \ell^4}{dD} \\ &\alpha_1 = \frac{\ell d d_3}{D}, \quad \alpha_2 = \frac{d_3 d^2}{2D}, \quad \alpha_3 = \frac{d_3 \nu \ell d}{D} \\ &\alpha_4 = \frac{\nu d_3 d^2}{2D}, \quad \alpha_5 = \frac{\epsilon_0 \epsilon_r \ell^4}{D d^3}, \quad \alpha_6 = \frac{d}{\ell} \end{aligned} \tag{5.51}$$

5.2 Linear Eigenvalue Problem

We let

$$w_d(x, y, t) = W_n(x, y) e^{i\omega_n t} \tag{5.52}$$

$$u_d(x, y, t) = U_n(x, y) e^{i\omega_n t} \tag{5.53}$$

$$v(x, y, t) = V_n(x, y) e^{i\omega_n t} \tag{5.54}$$

$$\bar{P}(x, y, t) = P_n(x, y) e^{i\omega_n t} \tag{5.55}$$

where $W_n(x, y)$, $V_n(x, y)$, and $U_n(x, y)$ are the nth transverse, lateral, and longitudinal complex mode shapes of the plate, respectively, $P_n(x, y)$ is the corresponding nth pressure mode shape, and ω_n is the nth complex nondimensional eigenvalue. Next, we

substitute equations (5.52-5.55) into equations (5.37-5.50) and obtain

$$\nabla^4 W_n - N W_{n,xx} - \omega_n^2 W_n - \alpha_1 U_{n,x} w_{s,xx} - \alpha_2 W_{n,xx} w_{s,x}^2 - \alpha_3 V_{n,y} w_{s,xx} - \alpha_4 W_{n,yy} w_{s,x}^2 - \alpha_5 \frac{V_p^2 W_n}{(1-w_s)^3} - \alpha_1 u_{s,x} W_{n,xx} - \alpha_3 u_{s,x} W_{n,yy} - 2\alpha_2 w_{s,x} w_{s,xx} W_{n,x} + P_{non} P_n = 0 \tag{5.56}$$

$$U_{n,xx} + \alpha_6 W_{n,x} w_{s,xx} + \alpha_6 w_{s,x} W_{n,xx} + \nu V_{n,xy} + \frac{1}{2}(1-\nu)(U_{n,yy} + V_{n,xy} + \alpha_6 w_{s,x} W_{n,yy}) = 0 \tag{5.57}$$

$$V_{n,yy} + \nu U_{n,xy} + \nu \alpha_6 w_{s,x} W_{n,xy} + \frac{1}{2}(1-\nu)(U_{n,xy} + V_{n,xx} + \alpha_6 w_{s,x} W_{n,xy} + \alpha_6 W_{n,y} w_{s,xx}) = 0 \tag{5.58}$$

$$\frac{\partial}{\partial x}\left[(1-w_s)^3 P_{n,x}\right] + \frac{\partial}{\partial y}\left[(1-w_s)^3 P_{n,y}\right] = i\sigma\omega_n\left[(1-w_s)P_n - W_n\right] \tag{5.59}$$

At $y = 0$ and $y = b/\ell$

$$V_{n,y} + \nu\alpha_6 U_{n,x} + \nu w_{s,x} W_{n,x} = 0 \tag{5.60}$$

$$U_{n,y} + V_{n,x} + \alpha_6 w_{s,x} W_{n,y} = 0 \tag{5.61}$$

$$W_{n,yy} + \nu W_{n,xx} = 0 \tag{5.62}$$

$$W_{n,yyy} + (2-\nu) W_{n,xxy} = 0 \tag{5.63}$$

$$P_n = 0 \tag{5.64}$$

Clamped edges at $x = 0$ and $x = 1$

$$U_n = 0 \tag{5.65}$$

$$V_n = 0 \tag{5.66}$$

$$W_n = 0 \tag{5.67}$$

$$W_{n,x} = 0 \tag{5.68}$$

$$P_{n,x} = 0 \tag{5.69}$$

5.3 Singular-Perturbation Analysis

In this section, we extend the analysis presented in Chapter 4 to the case of initially deflected microplates. Because $|\omega_n|\,\sigma >> 1$ in equation (5.59), we use a perturbation method to express the pressure in terms of the deflection. Then, we substitute this expression into equation (5.56) and solve the resulting equation along with equations (5.57), (5.58), (5.60-5.63), and (5.65-5.68) using a finite-element method. We use the method of matched asymptotic expansions (Nayfeh, 1981) to derive a uniformly valid asymptotic solution for equations (5.59), (5.64), and (5.69). In this method, an outer solution, which is valid everywhere in the domain except close to the boundary layers, is matched with inner solutions, which are valid only in the boundary layers. Then, a composite expansion is formed using the outer and inner expansions.

We derive the outer solution by dividing equation (5.59) by $\omega_n\sigma$, in which case the right-hand side of the resulting equation is very small ($O(\epsilon)$, where $\epsilon = \frac{1}{\omega_n\sigma}$) compared to the left-hand side. Hence, the outer solution is given to the first-order approximation by

$$P_n^o(x,y) = \frac{W_n(x,y)}{1 - w_s(x)} \tag{5.70}$$

where the superscript o denotes an outer solution. This solution satisfies the boundary conditions (5.69) because W_n satisfies similar boundary conditions at $x = 0$ and 1. However, because $\bar{P}_n = 0$ at $y = 0$ and b/ℓ, P_n^o does not satisfy the boundary conditions

(5.64) and hence equation (5.70) is not valid in narrow layers near $y = 0$ and b/ℓ. Therefore, we need to determine two inner expansions valid near these boundaries.

We begin by deriving an inner solution P_n^i valid in the boundary layer near $y = 0$. We introduce an inner variable $\xi = \frac{y}{\epsilon^\alpha}$, where $\alpha > 0$ is to be determined later. Next, we rewrite equation (5.59) in terms of ξ and note that $\alpha = \frac{1}{2}$ corresponds to the distinguished limit (Nayfeh, 1981). Accordingly, we obtain

$$\frac{\partial^2 P_n^i}{\partial \xi^2} - \frac{i P_n^i}{(1-w_s)^2} = \frac{-i W_n}{(1-w_s)^3} \tag{5.71}$$

From equation (5.64), we conclude that

$$P_n^i(x,0) = 0 \tag{5.72}$$

The solution of equation (5.71) that decays away from $y = 0$ can be expressed as

$$P_n^i(x,y) = \frac{W_n(x,0)}{1-w_s} + c_1 e^{-\frac{1+i}{\sqrt{2}}\frac{\xi}{1-w_s}} \tag{5.73}$$

Imposing the boundary condition (5.72), we obtain

$$c_1 = -\frac{W_n(x,0)}{1-w_s} \tag{5.74}$$

To derive the second inner solution P_n^I in the boundary layer near $y = b/\ell$, we introduce an inner variable $\zeta = \frac{b/\ell - y}{\sqrt{\epsilon}}$, repeat the above steps, and obtain

$$P_n^I(x,y) = \frac{W_n(x,b/\ell)}{1-w_s} - \frac{W_n(x,b/\ell)}{1-w_s} e^{-\frac{1+i}{\sqrt{2}}\frac{\zeta}{1-w_s}} \tag{5.75}$$

Combining the outer solution, equation (5.70), with the two inner solutions, equations (5.73) and (5.75), we obtain the following uniformly valid solution, also called composite expansion (Nayfeh, 1981):

$$P_n(x,y) = \frac{1}{1-w_s}\Big[W_n(x,y) - W_n(x,b/\ell)e^{-\frac{1+i}{\sqrt{2}}\frac{b/\ell-y}{\sqrt{\epsilon}(1-w_s)}} - W_n(x,0)e^{-\frac{1+i}{\sqrt{2}}\frac{y}{\sqrt{\epsilon}(1-w_s)}}\Big] \tag{5.76}$$

By setting $w_s = 0$ in equation (5.76), we end up with an equation similar to that of a plate actuated by small DC forces, which is the case in Chapter 4.

5.4 Results

We solve equations (5.15) and (5.16) using the reduced-order model of Younis et al. (2003) for the static deflection of the microplate under the DC forces. We then substitute the result and equation (5.76) into equation (5.56) and solve the resulting equation along with equations (5.57), (5.58), (5.60-5.63), and (5.65-5.68) using a finite-element method (Reddy, 1993; Zienkiewicz and Taylor, 1991). Details of the derivation of the finite-element model is presented in Section 5.6. The finite-element solution gives the complex eigenvalue ω_n and the corresponding eigenvector W_n, V_n, and U_n. The real part of ω_n yields the nth natural frequency, whereas the ratio between its real and twice its imaginary part yields the quality factor. We use equation (5.76) in the post-processing stage to calculate the pressure distribution underneath the plate.

Next, we calculate the natural frequencies and quality factors of electrostatically actuated microplates under the effect of squeeze-film damping. We first consider the microplate designed by Tilmans and Legtenberg (1994) as a resonator, with $\ell = 210\mu m$, $b = 100\mu m$, $h = 1.5\mu m$, $d = 1.18\mu m$, $E = 166GPa$, $\hat{N} = 9.0 \times 10^{-}8Newton$, and $V_p = 6V$.

We first calculate the damped fundamental natural frequency of the microplate under various DC loadings. We estimate that $P_a = 1mbar$ from matching the calculated Q to the measured value 592 reported by Tilmans and Legtenberg (1994). In Figure 5.3, we show a comparison of the normalized damped fundamental natural frequency ω_{nor} calculated using the present model (circles) with the theoretical results (squares) reported by Younis et al. (2002) and Abdel-Rahman et al. (2002), which are based on

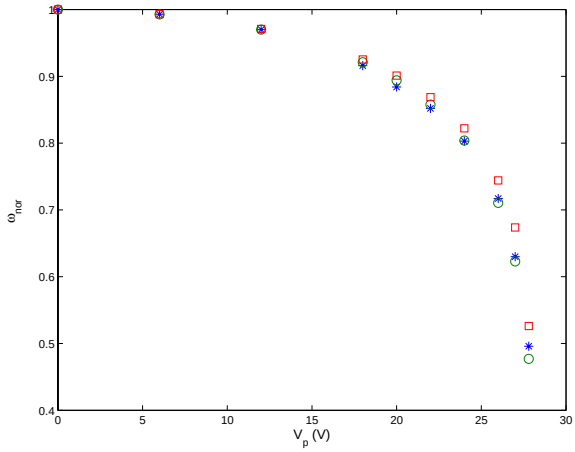

Figure 5.3: A comparison of the normalized fundamental natural frequencies calculated using the 2-D finite-element model (circles) with those obtained theoretically (squares) (Younis et al., 2002; Abdel-Rahman et al., 2002) and experimentally (stars) (Tilmans and Legtenberg, 1994) for a $210\mu m$ length microbeam.

a beam model, and the experimental data (stars) of Tilmans and Legtenberg (1994). We use a mesh of 24×12 in the finite-element program. The agreement between the theoretical and experimental results is excellent, thereby validating the model.

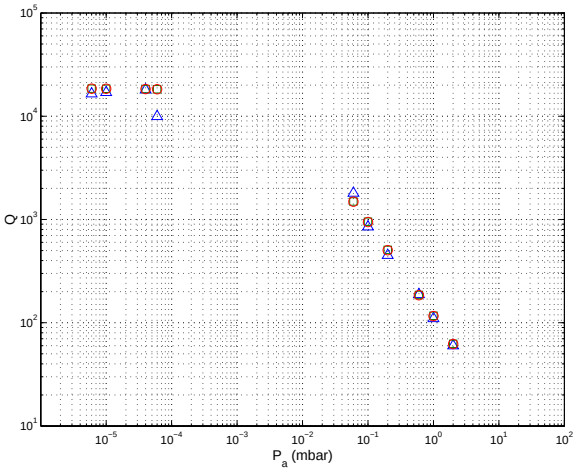

Figure 5.4: A comparison of the quality factors of a microplate calculated using the present model (circles) and a linearized plate model (Nayfeh and Younis, 2004) (squares) with the experimental data (triangles) of Legtenberg and Tilmans (1994).

In Figure 5.4, we show a comparison of the calculated quality factors for a mi-

croplate of length $310\mu m$ using the present model (circles) and a linear plate model (Nayfeh and Younis, 2004) derived in Chapter 4 (squares) with the experimental data (triangles) of Legtenberg and Tilmans (1994). The microbeam is actuated at $V_p = 2V$ and its quality factor near vacuum is $Q_{vacuum} = 18500$. The rest of the specifications are the same as the $210\mu m$ microbeam of Figure 5.3. We note that the model gives results very close to the linear model of Chapter 4 because the plates are actuated by low DC voltages, in which the in-plane deflections are negligible. Therfore, we conclude that the simplified linear model of Chapter 4 produces accurate results at low DC loadings.

The operating conditions of many MEMS devices exceed the range of small DC loadings. Devices, such as capacitive microswitches and projection arrays, involve large deflections, which can exceed the pull-in instability. In such cases, the in-plane displacements become significant, and hence a simple plate model that neglects the in-plane displacements is suspect. In Figure 5.5, we show a comparison of the calculated quality factors and fundamental natural frequencies of the $210\mu m$ microplate of Figure 5.2 using the present model with those calculated using the simplified model in Chapter 4. We note that the simplified model overestimates the quality factors and the natural frequencies at nearly 30% of the pull-in voltage. This is because, as the DC force increases, the static deflection increases, the gap width decreases, and hence the squeeze-film damping increases. Further, the increase in the electrostatic force decreases the natural frequencies. This effect is not represented correctly in the simplified model. We conclude from Figure 5.5a that the use of a single value for the quality factor in the simulation of microdevices involving large bending is inaccurate because it is a strong function of the DC voltage.

Next, we investigate the effect of the DC loading and the gap pressure on the natural frequencies, quality factors, mode shapes, and pressure distribution. We consider the microplate of Figure 5.5. Figure 5.6 shows variation of the real part of ω_1 (i.e., ω_{1r}), which yields the fundamental natural frequency, and the imaginary part of ω_1 (i.e., ω_{1i}), which yields the damping of the first mode with V_p for various values of P_a. We note from Figure 5.6a that damping increases with V_p and grows sharply near the

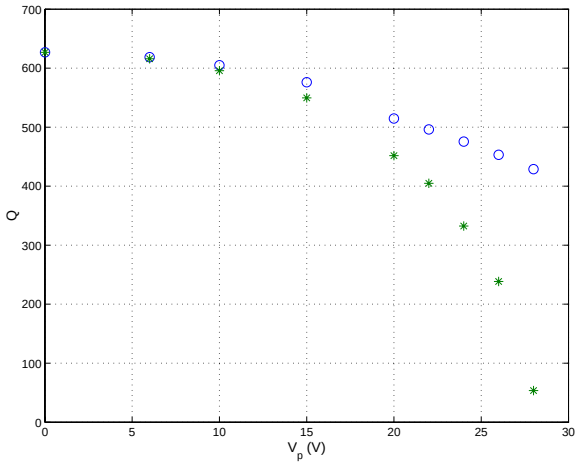

(a) Quality factors.

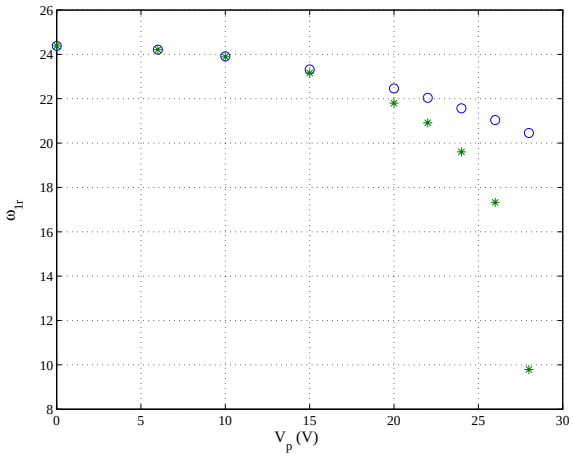

(b) Fundamental natural frequencies.

Figure 5.5: A comparison of the quality factors and natural frequencies of a $210\mu m$ length microplate calculated using the present model (circles) and a linearized plate model (Nayfeh and Younis, 2004) (stars) for various values of the DC voltage.

pull-in, where the microplate is highly deflected. Figure 5.6 shows a slight effect of the pressure on ω_{1r}. We conclude from Figure 5.6 that the quality factor, which is the ratio between ω_{1r} and twice ω_{1i}, decreases as V_p increases because of two factors: an increase in the viscous damping due to the decrease in the gap spacing and a decrease in the natural frequency as a result of the negative spring effect of the DC loading.

Figure 5.7 shows variation of the quality factor with V_p for various values of P_a.

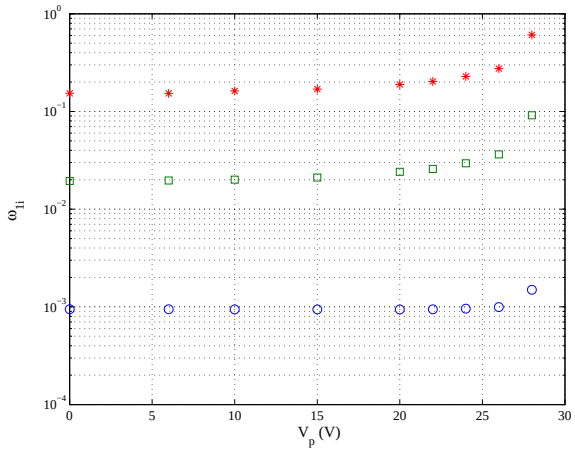

(a) Damping coefficient ω_{1i}.

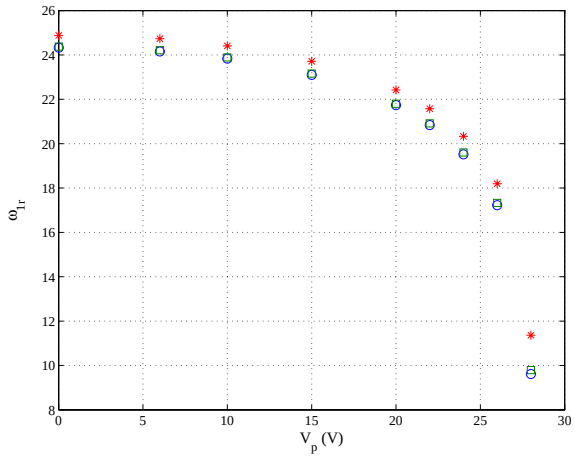

(b) Fundamental natural frequencies ω_{1r}.

Figure 5.6: Variation of the calculated ω_{1i} and ω_{1r} with V_p for $P_a = 0.01mbar$ (circles), $P_a = 1mbar$ (squares), and $P_a = 10mbar$ (stars).

Figure 5.8 shows the spatial variation of the first-mode shape for various values of the electrostatic force and gap pressure. The mode shape is normalized such that its integral over the area of the plate is unity. We note that the pressure has no effect on W_{1r}. The electrostatic force on the other hand influences W_{1r} in the y direction. Figure 5.9 shows the spatial variation of the pressure distribution corresponding to

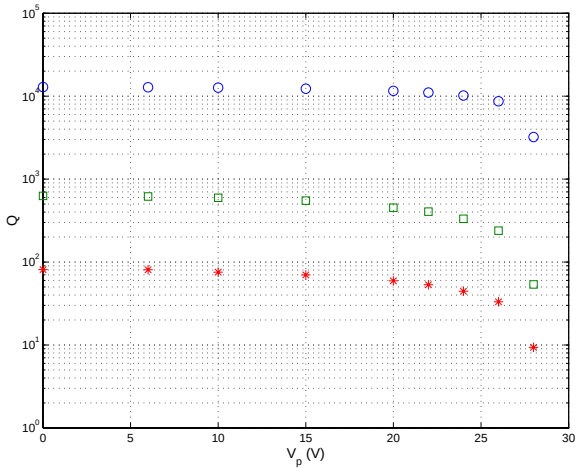

Figure 5.7: Variations of the quality factor with V_p for $P_a = 0.01mbar$ (circles), $P_a = 1mbar$ (squares), and $P_a = 10mbar$ (stars).

Figure 5.8. The function P_{1r} is normalized as W_{1r}. We note that varying the pressure has a slight effect on P_{1r} and that increasing the electrostatic loading has a much significant effect.

5.5 Damping Coefficient for Fully Clamped Microplates

We end up this chapter with the derivation of a damping coefficient, which can be used in reduced-order models, for the case of deflected fully clamped microplates due to large electrostatic forces under the effect of squeeze-film damping. Unlike the case of fixed-free-fixed-free plates, the static deflection w_s is a function of x and y. Hence, the calculation of $w_s(x, y)$ of fully clamped plates requires the use of a plate model rather than a beam model. One way of achieving this is to use a microplate reduced-order model (Zhao et al., 2004).

The structural boundary conditions for fully clamped microplates are

Clamped edges at $y = 0$ and $y = b/\ell$

$$U_n = V_n = W_n = W_{n,x} = 0 \tag{5.77}$$

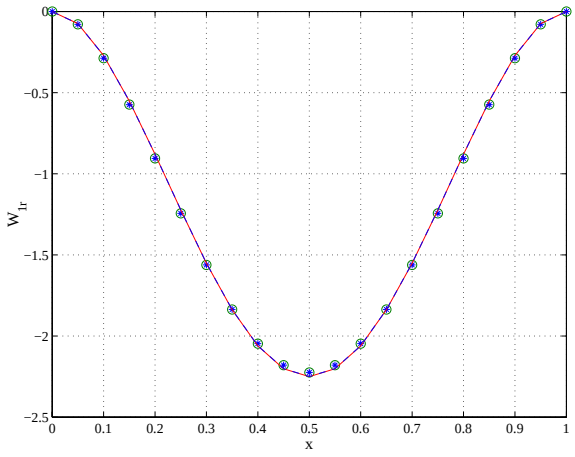

(a) W_{1r} at $y = b/2\ell$.

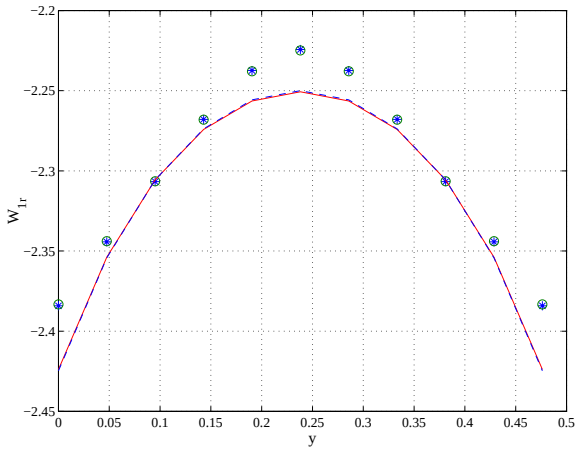

(b) W_{1r} at $x = 1/2$.

Figure 5.8: The spatial variation of W_{1r} when $V_p = 6V$ (discrete points) and $V_p = 28V$ (solid and dashes lines). The data shown in circles and dashed line correspond to $P_a = 0.01mbar$ and the data in stars and solid line correspond to $P_a = 2mbar$.

Clamped edges at $x = 0$ and $x = 1$

$$U_n = V_n = W_n = W_{n,x} = 0 \tag{5.78}$$

The pressure boundary conditions are

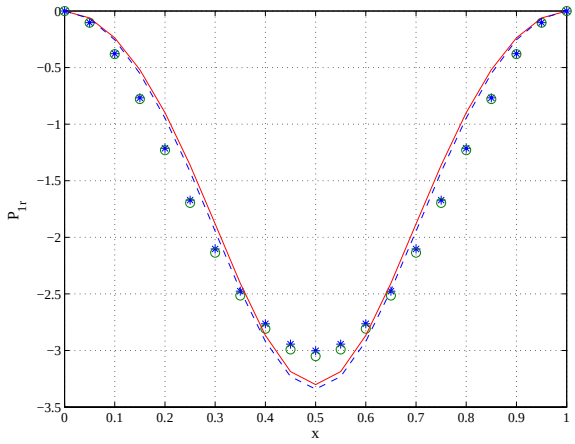

(a) P_{1r} at $y = b/2\ell$.

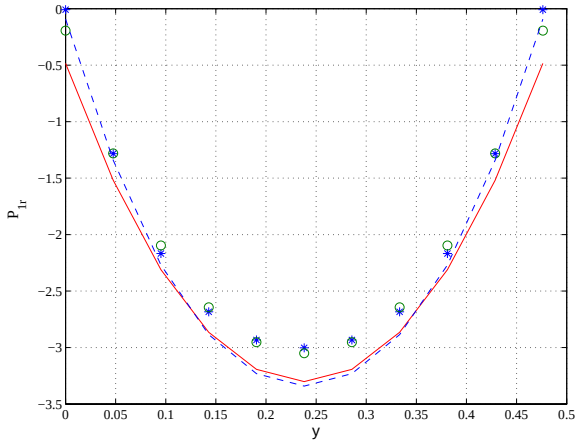

(b) P_{1r} at $x = 1/2$.

Figure 5.9: The spatial variation of P_{1r} when $V_p = 6V$ (discrete points) and $V_p = 28V$ (solid and dashes lines). The data shown in circles and dashed line correspond to $P_a = 0.01mbar$ and the data in stars and solid line correspond to $P_a = 2mbar$.

$$P_{n,x}(x, 0, t) = P_{n,y}(x, b/\ell, t) = 0 \tag{5.79}$$

$$P_{n,x}(0, y, t) = P_{n,y}(1, y, t) = 0 \tag{5.80}$$

It follows from equations (5.77-5.80) that there are no boundary layers in this case to the first approximation because the pressure boundary conditions are satisfied to first order according to equation (5.68). To derive an expression for the damping coefficient, we need to proceed to higher orders in the perturbation analysis. To this end, we apply the method of strained parameters (Nayfeh, 1981) and seek a first-order solution to equations (5.56-5.59) and (5.77-5.80) in the form

$$W_n = W_{n_0} + \epsilon W_{n_1} + ... \tag{5.81}$$

$$U_n = U_{n_0} + \epsilon U_{n_1} + ... \tag{5.82}$$

$$V_n = V_{n_0} + \epsilon V_{n_1} + ... \tag{5.83}$$

$$P_n = P_{n_0} + \epsilon P_{n_1} + ... \tag{5.84}$$

$$\omega_n = \omega_{n_0} + \epsilon \omega_{n_1} + ... \tag{5.85}$$

where $\epsilon = \frac{1}{\sigma \omega_{n_0}}$. Substituting equations (5.81-5.85) into equations (5.56-5.59) and (5.77-5.80), we obtain

$\underline{O(\epsilon_0)}$

$$P_{n_0} = \frac{W_{n_0}}{1 - w_s} \tag{5.86}$$

$$\begin{aligned}
&\mathcal{L}_1(P_{n_0}, U_{n_0}, V_{n_0}, W_{n_0}) = \nabla^4 W_{n_0} - N W_{n_0,xx} \\
&- \alpha_1 U_{n_0,x} w_{s,xx} - \alpha_2 W_{n_0,xx} w_{s,x}^2 - \alpha_3 V_{n_0,y} w_{s,xx} \\
&- \alpha_1 u_{s,x} W_{n,xx} - \alpha_3 u_{s,x} W_{n,yy} - 2\alpha_2 w_{s,x} w_{s,xx} W_{n,x} \\
&- \alpha_4 W_{n_0,yy} w_{s,x}^2 - \alpha_5 \frac{V_p^2 W_{n_0}}{(1 - w_s)^3} + P_{non} P_{n_0} = \omega_{n_0}^2 W_{n_0}
\end{aligned} \tag{5.87}$$

$$\begin{aligned}
&\mathcal{L}_2(P_{n_0}, U_{n_0}, V_{n_0}, W_{n_0}) = U_{n_0,xx} + \alpha_6 W_{n_0,x} w_{s,xx} \\
&+ \alpha_6 w_{s,x} W_{n_0,xx} + \nu V_{n_0,xy} + \frac{1}{2}(1 - \nu)(U_{n_0,yy} + V_{n_0,xy} \\
&+ \alpha_6 w_{s,x} W_{n_0,yy}) = 0
\end{aligned} \tag{5.88}$$

$$\mathcal{L}_3(P_{n_0}, U_{n_0}, V_{n_0}, W_{n_0}) = V_{n_0,yy} + \nu U_{n_0,xy} + \nu\alpha_6 w_{s,x} W_{n_0,xy} + \frac{1}{2}(1-\nu)(U_{n_0,xy} + V_{n_0,xx} + \alpha_6 w_{s,x} W_{n_0,xy} + \alpha_6 W_{n_0,y} w_{s,xx}) = 0 \tag{5.89}$$

$\underline{O(\epsilon_1)}$

$$P_{n_1} = \frac{1}{1-w_s}\Big\{ -i\Big(\frac{\partial}{\partial x}\Big[(1-w_s)^3 \frac{\partial}{\partial x}(\frac{W_{n_0}}{1-w_s})\Big] + \frac{\partial}{\partial y}\Big[(1-w_s)^3 \frac{\partial}{\partial y}(\frac{W_{n_0}}{1-w_s})\Big]\Big) + \phi_1\Big\} \tag{5.90}$$

$$\mathcal{L}_1(P_{n_1}, U_{n_1}, V_{n_1}, W_{n_1}) - \omega_{n_0}^2 W_{n_1} = 2\omega_{n_0}\omega_{n_1} W_{n_0} \tag{5.91}$$

$$\mathcal{L}_2(P_{n_1}, U_{n_1}, V_{n_1}, W_{n_1}) = 0 \tag{5.92}$$

$$\mathcal{L}_3(P_{n_1}, U_{n_1}, V_{n_1}, W_{n_1}) = 0 \tag{5.93}$$

The boundary conditions for equations (5.86-5.93) are

$\underline{\text{At } y = 0 \text{ and } y = b/\ell}$

$$U_{n_j} = V_{n_j} = W_{n_j} = W_{n_j,x} = 0 \tag{5.94}$$

$\underline{\text{At } x = 0 \text{ and } x = 1}$

$$U_{n_j} = V_{n_j} = W_{n_j} = W_{n_j,x} = 0 \tag{5.95}$$

where $j = 0, 1$. Substituting equation (5.86) into equation (5.87) and equations (5.86) and (5.90) into equation (5.91), we obtain

$$\nabla^4 W_{n_0} - N W_{n_0,xx} - \alpha_1 U_{n_0,x} w_{s,xx} - \alpha_2 W_{n_0,xx} w_{s,x}^2 - \alpha_1 u_{s,x} W_{n_0,xx} - \alpha_3 u_{s,x} W_{n_0,yy} - 2\alpha_2 w_{s,x} w_{s,xx} W_{n_0,x} - \alpha_3 V_{n_0,y} w_{s,xx} - \alpha_4 W_{n_0,yy} w_{s,x}^2 - \alpha_5 \frac{V_p^2 W_{n_0}}{(1-w_s)^3} + P_{non} \frac{W_{n_0}}{1-w_s} - \omega_{n_0}^2 W_{n_0} = 0 \tag{5.96}$$

$$\nabla^4 W_{n_1} - N W_{n_1,xx} - \alpha_1 U_{n_1,x} w_{s,xx} - \alpha_2 W_{n_1,xx} w_{s,x}^2$$
$$- \alpha_1 u_{s,x} W_{n_1,xx} - \alpha_3 u_{s,x} W_{n_1,yy} - 2\alpha_2 w_{s,x} w_{s,xx} W_{n_1,x}$$
$$- \alpha_3 V_{n_1,y} w_{s,xx} - \alpha_4 W_{n_1,yy} w_{s,x}^2 - \alpha_5 \frac{V_p^2 W_{n_1}}{(1-w_s)^3}$$
$$+ P_{non} \frac{W_{n_1}}{1-w_s} - \omega_{n_1}^2 W_{n_0} = 2\omega_{n_0}\omega_{n_1} W_{n_0}$$
$$+ \frac{iP_{non}}{1-w_s}\Big\{\frac{\partial}{\partial x}\left[(1-w_s)^3 \frac{\partial}{\partial x}(\frac{W_{n_0}}{1-w_s})\right]$$
$$+ \frac{\partial}{\partial y}\left[(1-w_s)^3 \frac{\partial}{\partial y}(\frac{W_{n_0}}{1-w_s})\right]\Big\} \tag{5.97}$$

We note that the homogeneous second-order problem, equations (5.94), (5.95), and (5.97), is the same as the first-order problem, equations (5.94-5.96). Hence, the first-order problem has a solution only if the right-hand side of equation (5.97) is orthogonal to every solution of the adjoint homogeneous problem governing W_{n_1} (solvability condition (Nayfeh, 1981)). Noting that the system is self-adjoint, we impose the solvability conditions on equation (5.97) by multiplying its right-hand side with the adjoint of W_{n_1} and integrating the result over the plate area. The result is

$$\omega_1 = \frac{-iP_{non}}{2\omega_{n_0}\int_0^1\int_0^{b/\ell} W_{n_0}^2 dxdy}\int_0^1\int_0^{b/\ell}\Big\{\frac{W_{n_0}}{1-w_s}\Big(\frac{\partial}{\partial x}\Big[(1-w_s)^3\frac{\partial}{\partial x}(\frac{W_{n_0}}{1-w_s})\Big]$$
$$+ \frac{\partial}{\partial y}\Big[(1-w_s)^3\frac{\partial}{\partial y}(\frac{W_{n_0}}{1-w_s})\Big]\Big)\Big\}dxdy \tag{5.98}$$

Equation (5.98) yields the damping coefficient of the microplate due to squeeze-film damping and large electrostatic forces.

5.6 Finite-Element Formulation

This section gives some details on the finite-element formulation, which is the basis of the finite-element code used in this chapter and Chapter 4.

5.6.1 Weak Form

The first step in generating the finite-element model is to derive the weak form (Reddy, 1993) associated with equations (5.56-5.58), (5.60-5.63), and (5.65-5.68). The weak

form can be constructed using the principle of virtual displacements. Alternatively, we follow Reddy (1993) and multiply equations (5.56-5.58) by the weight functions $\hat{W}$, $\hat{U}$, and $\hat{V}$, respectively, integrate by parts over the area Ω_e of an arbitrary element to distribute the differentiation equally between the weight functions and the dependent variables, and obtain the following weak form:

$$\begin{aligned}
&\int_{\Omega_e} \Big\{ \hat{W}_{,xx}[W_{n,xx} + \nu W_{n,yy}] + \hat{W}_{,yy}[W_{n,yy} + \nu W_{n,xx}] \\
&+ 2(1-\nu)\hat{W}_{,xy} W_{n,xy} + N\hat{W}_{,x} W_{n,x} - \hat{W}\big[\alpha_1 U_{n,x} w_{s,xx} \\
&+ \alpha_2 w_{s,x}^2 W_{n,xx} + \alpha_3 w_{s,xx} V_{n,y} + \alpha_4 w_{s,x}^2 W_{n,yy} + \\
&\alpha_1 u_{s,x} W_{n,xx} + \alpha_3 u_{s,x} W_{n,yy} + 2\alpha_2 w_{s,x} w_{s,xx} W_{n,x} + \\
&\omega_n^2 W_n + \alpha_5 \frac{V_p^2 W}{(1-w_s)^3} - P_{non} F\left(W_n, w_s\right) \big] \Big\} dxdy \\
&+ \oint_{\Gamma_e} \hat{W} q_1 ds + \oint_{\Gamma_e} \hat{W}_{,x} q_2 ds + \oint_{\Gamma_e} \hat{W}_{,y} q_3 ds = 0
\end{aligned} \tag{5.99}$$

$$\begin{aligned}
&\int_{\Omega_e} \Big[\hat{U}_{,x}\big(U_{n,x} + \alpha_6 w_{s,x} W_{n,x} + \nu V_y\big) + \frac{1}{2}(1-\nu)\hat{U}_{,y}\big(U_{n,y} \\
&+ V_{n,x} + \alpha_6 w_{s,x} W_{n,y}\big) \Big] dxdy - \oint_{\Gamma_e} \hat{U} q_4 ds = 0
\end{aligned} \tag{5.100}$$

$$\begin{aligned}
&\int_{\Omega_e} \Big[\frac{1}{2}(1-\nu)\hat{V}_{,x}\big(U_{n,y} + V_{n,x} + \alpha_6 w_{s,x} W_{n,y}\big) + \hat{V}_{,y}\big(\nu U_{n,x} \\
&+ \alpha_6 w_{s,x} W_{n,x} + V_y\big) \Big] dxdy - \oint_{\Gamma_e} \hat{V} q_5 ds = 0
\end{aligned} \tag{5.101}$$

where

$$
\begin{aligned}
q_1 &= \big(W_{n,xxx} + \nu W_{n,xyy}\big)n_x + \big[W_{n,yyy} + (2-\nu)W_{n,xxy}\big]n_y \\
q_2 &= -\big(W_{n,xx} + \nu W_{n,yy}\big)n_x \\
q_3 &= -\big(W_{n,yy} + \nu W_{n,xx}\big)n_y \\
q_4 &= \big(U_{n,x} + \alpha_6 w_{s,x} W_{n,x} + \nu V_y\big)n_x + \frac{1}{2}(1-\nu)\big(U_{n,y} \\
&\quad + V_{n,x} + \alpha_6 w_{s,x} W_{n,y}\big)n_y \\
q_5 &= \frac{1}{2}(1-\nu)\big(U_{n,y} + V_{n,x} + \alpha_6 w_{s,x} W_{n,y}\big)n_x \\
&\quad + \big(\nu U_{n,x} + \alpha_6 w_{s,x} W_{n,x} + V_y\big)n_y
\end{aligned}
$$

The functional $F(W_n, w_s)$ denotes the right-hand side of equation (5.76), n_x and n_y are the unit normal vectors of an element boundary Γ_e, and ds is the arclength of a line element along the boundary.

5.6.2 Finite-Element Model

We use a rectangular element (Reddy, 1993; Zienkiewicz and Taylor, 1991) to discretize the plate. The element has four nodes, with five unknowns (W_n, $W_{n,x}$, $W_{n,y}$, U_n, V_n) at each node. We express W_n in terms of the Hermite interpolation functions Φ_j (Reddy, 1993; Zienkiewicz and Taylor, 1991) of a nonconforming rectangular element as

$$
W_n(x,y) = \sum_{j=1}^{m} \Delta_j^e \Phi_j(x,y), \qquad m = 12 \tag{5.102}
$$

where the Δ_j^e are the nodal values of W_n and its derivatives. We use the linear Lagrangian interpolation functions Ψ_j (Reddy, 1993; Zienkiewicz and Taylor, 1991) to express U_n and V_n as

$$
U_n(x,y) = \sum_{j=1}^{n} U_j^e \Psi_j(x,y), \qquad n = 4 \tag{5.103}
$$

$$
V_n(x,y) = \sum_{j=1}^{n} V_j^e \Psi_j(x,y), \qquad n = 4 \tag{5.104}
$$

where the U_j^e and V_j^e are the nodal values of U_n and V_n, respectively.

Next, we substitute equations (5.102-5.104) into equations (5.99-5.101), put $\hat{W} = \Phi_i$, $\hat{U} = \Psi_i$, and $\hat{V} = \Psi_i$, and obtain the following finite-element model for an element e:

$$
\begin{aligned}
&-\omega_n^2 \begin{bmatrix} [M^{11}]_{12\times12} & [0]_{12\times4} & [0]_{12\times4} \\ & [0]_{4\times4} & [0]_{4\times4} \\ \text{symmetric} & & [0]_{4\times4} \end{bmatrix} \begin{Bmatrix} \{\Delta^e\} \\ \{U^e\} \\ \{V^e\} \end{Bmatrix} \\
&+ \begin{bmatrix} [K^{11}]_{12\times12} & [K^{12}]_{12\times4} & [K^{13}]_{12\times4} \\ [K^{21}]_{4\times12} & [K^{22}]_{4\times4} & [K^{23}]_{4\times4} \\ [K^{31}]_{4\times12} & [K^{32}]_{4\times4} & [K^{33}]_{4\times4} \end{bmatrix} \begin{Bmatrix} \{\Delta^e\} \\ \{U^e\} \\ \{V^e\} \end{Bmatrix} \\
&= \begin{Bmatrix} \{F^1\}_{12\times1} \\ \{F^2\}_{4\times1} \\ \{F^3\}_{4\times1} \end{Bmatrix}
\end{aligned} \tag{5.105}
$$

where

$$M_{ij}^{11} = \int_{\Omega_e} \Phi_i \Phi_j dxdy \tag{5.106}$$

$$F_i^1 = \oint_{\Gamma_e} \Big\{ \Phi_i q_1 + \Phi_{i,x} q_2 + \Phi_{i,y} q_3 \Big\} ds \tag{5.107}$$

$$F_i^2 = \oint_{\Gamma_e} \Psi_i q_4 ds \tag{5.108}$$

$$F_i^3 = \oint_{\Gamma_e} \Psi_i q_5 ds \tag{5.109}$$

$$
\begin{aligned}
K_{ij}^{11} = \int_{\Omega_e} \Big\{ & \Phi_{i,xx}[\Phi_{j,xx} + \nu\Phi_{j,yy}] + \Phi_{i,yy}[\Phi_{j,yy} + \nu\Phi_{j,xx}] \\
& + 2(1-\nu)\Phi_{i,xy}\Phi_{j,xy} + N\Phi_{i,x}\Phi_{j,x} - \Phi_i \big[\alpha_2 w_{s,x}^2 \Phi_{j,xx} \\
& \alpha_1 u_{s,x}\Phi_{j,xx} + \alpha_3 u_{s,x}\Phi_{j,yy} + 2\alpha_2 w_{s,x} w_{s,xx}\Phi_{j,x} + \\
& + \alpha_4 w_{s,x}^2 \Phi_{j,yy} + \alpha_5 \frac{V_p^2 \Phi_j}{(1-w_s)^3} - P_{non} F(\Phi_j, w_s) \big] \Big\} dxdy
\end{aligned} \tag{5.110}
$$

$$K_{ij}^{12} = -\alpha_1 \int_{\Omega_e} w_{s,xx} \Phi_i \Psi_{j,x} dxdy \tag{5.111}$$

$$K_{ij}^{13} = -\alpha_3 \int_{\Omega_e} w_{s,xx} \Phi_i \Psi_{j,y} dxdy \tag{5.112}$$

$$K_{ij}^{21} = \alpha_6 \int_{\Omega_e} \Big[w_{s,x} \Psi_{i,x} \Phi_{j,x} + \frac{1}{2}(1-\nu) w_{s,x} \Psi_{i,y} \Phi_{j,y} \Big] dxdy \tag{5.113}$$

$$K_{ij}^{22} = \int_{\Omega_e} \Big[\Psi_{i,x} \Psi_{j,x} + \frac{1}{2}(1-\nu) \Psi_{i,y} \Psi_{j,y} \Big] dxdy \tag{5.114}$$

$$K_{ij}^{23} = \int_{\Omega_e} \Big[\nu \Psi_{i,x} \Psi_{j,y} + \frac{1}{2}(1-\nu) \Psi_{i,y} \Psi_{j,x} \Big] dxdy \tag{5.115}$$

$$K_{ij}^{31} = \alpha_6 \int_{\Omega_e} \Big[w_{s,x} \Psi_{i,y} \Phi_{j,x} + \frac{1}{2}(1-\nu) w_{s,x} \Psi_{i,y} \Phi_{j,x} \Big] dxdy \tag{5.116}$$

$$K_{ij}^{32} = \int_{\Omega_e} \Big[\nu \Psi_{i,y} \Psi_{j,x} + \frac{1}{2}(1-\nu) \Psi_{i,x} \Psi_{j,y} \Big] dxdy \tag{5.117}$$

$$K_{ij}^{33} = \int_{\Omega_e} \Big[\Psi_{i,y} \Psi_{j,y} + \frac{1}{2}(1-\nu) \Psi_{i,x} \Psi_{j,x} \Big] dxdy \tag{5.118}$$

$$\{\Delta^e\} = \Big\{ \; W_{n_1} \quad W_{n_1,x} \quad W_{n_1,y} \quad ... \quad W_{n_4,y} \; \Big\}^T \tag{5.119}$$

$$\{U^e\} = \Big\{ \; U_{n_1} \quad U_{n_2} \quad U_{n_3} \quad U_{n_4} \; \Big\}^T \tag{5.120}$$

$$\{V^e\} = \Big\{ \; V_{n_1} \quad V_{n_2} \quad V_{n_3} \quad V_{n_4} \; \Big\}^T \tag{5.121}$$

Chapter 6

A Model for Thermoelastic Damping in Microplates

In the absence of squeeze-film damping, other energy losses limit the quality factors of microplates. The majority of these losses are extrinsic, and hence can be minimized by a proper design of devices. Thermoelastic damping however is an intrinsic source of energy dissipation, which can affect the quality factor significantly. Thermoelastic damping has been shown recently to be a dominant source of intrinsic damping in MEMS. Thermoelastic damping results from the irreversible heat flow generated by the compression and decompression of an oscillating structure.

In this chapter, we present a model and analytical expressions for the quality factors of microplates due to thermoelastic damping. We solve the heat equation for the thermal flow across the microplate, and hence decouple the thermal equation from the plate equation. We utilize a perturbation method to derive an analytical expression for the quality factor of microplates, of general boundary conditions, under electrostatic loading and residual stresses in terms of their structural mode shapes. For the special case of no electrostatic and in-plane loadings, we derive a simple analytical expression for the quality factor, which is independent of the mode shapes. We verify the model by specializing it to a microbeam and comparing the resulting quality factor to that obtained using microbeam models in the literature. We present several results

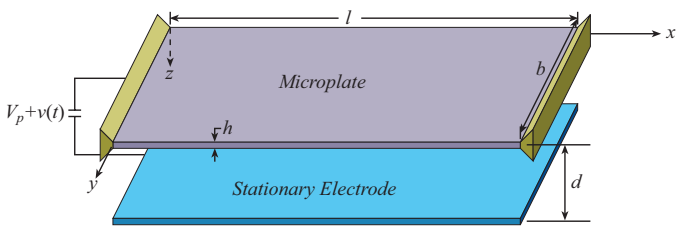

Figure 6.1: Electrically actuated microplate.

for various modes of microplates with various boundary conditions.

6.1 Problem Formulation

We consider a microplate (Figure 6.1) actuated by an electric load composed of a DC component V_p and an AC component $v_e(t)$. We assume that all forms of extrinsic damping, such as viscous damping, can be neglected. Assuming small strains and displacements, we obtain the following linear equation of motion governing the transverse deflection of the microplate including the effect of thermoelastic damping (Leissa, 1969; Boley and Weiner, 1960):

$$D\nabla^4 w - N_1^* \frac{\partial^2 w}{\partial x^2} + \rho h \frac{\partial^2 w}{\partial t^2} = \frac{\epsilon V_p v_e}{d^2} + \frac{\epsilon V_p^2}{d^3} w - \nabla^2 w N^T - \nabla^2 M^T \qquad (6.1)$$

where $w(x, y, t)$ is the transverse deflection of the plate at the position x and y at time t, ρ is the plate material density, d is the initial gap width, $D = \frac{Eh^3}{12(1-\nu^2)}$ is the plate flexural rigidity, h is the microplate thickness, E is Young's modulus, ν is Poisson's ratio, N_1^* is the axial force per unit length in the x direction, ϵ is the dielectric constant of the gap medium, and N^T and M^T are the thermal in-plane axial force and bending moment, respectively. The operators ∇^2 and ∇^4 are the Laplacian and biharmonic operators, respectively. The first two terms on the right-hand side of equation (6.1) represent an approximation of the parallel-plate electrostatic forces assuming a small DC loading and complete overlapping of the microplate and the stationary electrode.

The thermal axial force and bending moment are defined as

$$N^T = \frac{E\alpha_t}{1-\nu}\int_{-h/2}^{h/2}(T-T_0)dz \tag{6.2}$$

$$M^T = \frac{E\alpha_t}{1-\nu}\int_{-h/2}^{h/2}z(T-T_0)dz \tag{6.3}$$

where $T(x,y,z,t)$ is the temperature distribution, T_0 is the stress-free temperature, and α_t is the coefficient of thermal expansion.

The temperature distribution is governed by the heat conduction equation (Boley and Weiner, 1960)

$$k\nabla^2 T + q = \rho C_p\frac{\partial T}{\partial t} + \frac{E\alpha_t T}{1-2\nu}\frac{\partial e}{\partial t} \tag{6.4}$$

where C_p is the heat capacity coefficient at constant pressure, q is the heat flux, and e is the dilatation strain due to the thermal effect defined as (Boley and Weiner, 1960)

$$e = -\frac{1-2\nu}{1-\nu}z\nabla^2 w + \frac{1+\nu}{1-\nu}\alpha_t(T-T_0) \tag{6.5}$$

In most application, T on the right-hand side of equation (6.4) can be replaced by T_0 to yield a linear equation for the temperature. Substituting equation (6.5) into equation (6.4) results in the following linearized version of the heat equation:

$$k\nabla^2 T + q = \left(\rho C_p + \frac{E\alpha_t^2 T_0(1+\nu)}{(1-2\nu)(1-\nu)}\right)\frac{\partial T}{\partial t} - \frac{E\alpha_t T_0}{1-\nu}\frac{\partial}{\partial t}(z\nabla^2 w) \tag{6.6}$$

6.1.1 Linear Eigenvalue Problem

For the linear damped eigenvalue problem, we let

$$w(x,y,t) = \phi_n(x,y)e^{i\omega_n t} \tag{6.7}$$

$$T(x,y,z,t) - T_0 = \theta_n(x,y,z)e^{i\omega_n t} \tag{6.8}$$

where $\phi_n(x,y)$ and $\theta_n(x,y,z)$ are the nth complex mode shapes of the plate and the associated temperature variation, respectively, and ω_n is the nth complex eigenvalue.

Substituting equations (6.7) and (6.8) into equations (6.1) and (6.6), dropping q and the forcing term v_e, and noting that the temperature variation across the plate thickness is much larger than its variation across the plane of the plate, we obtain

$$\nabla^4\phi_n - N_1^*\frac{\partial^2\phi_n}{\partial x^2} + \frac{E\alpha_t}{1-\nu}\nabla^2\phi_n\int_{-h/2}^{h/2}\theta_n dz + \frac{E\alpha_t}{1-\nu}\int_{-h/2}^{h/2}z\nabla^2\theta_n dz - \frac{\epsilon V_p^2}{d^3}\phi_n = \omega_n^2\phi_n \tag{6.9}$$

$$k\frac{\partial^2\theta_n}{\partial z^2} = i\omega_n\Big[\rho C_p + \frac{E\alpha_t^2(1+\nu)T_0}{(1-\nu)(1-2\nu)}\Big]\theta_n - i\omega_n\frac{E\alpha_t T_0}{1-\nu}z\nabla^2\phi_n \tag{6.10}$$

The temperature conditions are zero-heat flux from the plate to the ambient (Zener, 1937); that is,

$$\frac{\partial\theta_n}{\partial z} = 0 \qquad \text{at} \qquad z = \frac{1}{2}h \qquad \text{and} \qquad z = -\frac{1}{2}h \tag{6.11}$$

The general solution of equation (6.10) can be expressed as

$$\theta_n = \frac{E\alpha_t T_0}{(1-\nu)\chi}z\nabla^2\phi_n + c_1\sin(K_p z) + c_2\cos(K_p z) \tag{6.12}$$

where

$$\chi = \rho C_p + \frac{E\alpha_t^2(1+\nu)T_0}{(1-\nu)(1-2\nu)}, \qquad K_p = (1-i)\sqrt{\frac{\omega_n\chi}{2k}}$$

Next, we impose the boundary conditions, equation (6.11), on equation (6.12) and obtain

$$\theta_n = \frac{E\alpha_t T_0}{(1-\nu)\chi}\nabla^2\phi_n\left(z - \frac{\sin(K_p z)}{K_p\cos(\frac{1}{2}K_p h)}\right) \tag{6.13}$$

Substituting equation (6.13) into equation (6.9), carrying out the integrations, and

retaining the linear terms, we obtain

$$D^T \nabla^4 \phi_n - N_1^* \frac{\partial^2 \phi_n}{\partial x^2} - \frac{\epsilon V_p^2}{d^3} \phi_n = \omega_n^2 \phi_n \tag{6.14}$$

where $D^T = D + D_t$ and D_t is given by

$$D_t = \frac{E^2 \alpha_t^2 T_0}{(1-\nu)^2 \chi} \Big(\frac{h^3}{12} + \frac{h}{K_p^2} - \frac{2 \tan(K_p h/2)}{K_p^3} \Big) \tag{6.15}$$

Equations (6.14) and (6.15) can be used, along with any appropriate set of boundary conditions, to simulate the behavior of an electrostatically actuated microplate accounting for thermoelastic damping.

6.1.2 Perturbation Analysis

Next, we derive an analytical expression for the quality factors of microplates due to thermoelastic damping. Because $D_t << D$, we apply the method of strained parameters (Nayfeh, 1981) to equation (6.14). The analysis is general for any boundary conditions. To this end, we seek a first-order solution to equation (6.14) and associated boundary conditions in the form

$$\phi_n \approx \phi_{n_0} + \varepsilon_1 \phi_{n_1} \tag{6.16}$$

$$\omega_n \approx \omega_{n_0} + \varepsilon_1 \omega_{n_1} \tag{6.17}$$

$$D^T \approx D + \varepsilon_1 D_t \tag{6.18}$$

where ε_1 is a small nondimensional bookkeeping parameter. Substituting equations (6.16-6.18) into equation (6.14) and separating terms of different order in ε_1 yields

$\underline{O(\varepsilon_1^0)}$

$$D \nabla^4 \phi_{n_0} - N_1^* \frac{\partial^2 \phi_{n_0}}{\partial x^2} - \frac{\epsilon V_p^2}{d^3} \phi_{n_0} - \omega_{n_0}^2 \phi_{n_0} = 0 \tag{6.19}$$

$\underline{O(\varepsilon_1)}$

$$D\nabla^4\phi_{n_1} - N_1^*\frac{\partial^2\phi_{n_1}}{\partial x^2} - \frac{\epsilon V_p^2}{d^3}\phi_{n_1} - \omega_{n_0}^2\phi_{n_1} = 2\omega_{n_0}\omega_{n_1}\phi_{n_0} - D_t\nabla^4\phi_{n_0} \tag{6.20}$$

We note that the homogeneous problem governing ϕ_{n1} is the same as the problem governing ϕ_{n0} and, because the latter has nontrivial solutions, the nonhomogeneous problem governing ϕ_{n1} has a solution only if the right-hand side of (6.20) is orthogonal to every solution of the adjoint homogeneous problem governing ϕ_{n_1} (solvability condition (Nayfeh, 1981)). Because the problem is self-adjoint, the solvability condition demands that the right-hand side of equation (6.20) be orthogonal to ϕ_{n_0}. Next, we solve for $\nabla^4\phi_{n_0}$ from equation (6.19), substitute it into equation (6.20), impose the solvability condition, and obtain

$$\omega_{n_1} = \frac{D_t}{2\omega_{n_0}D}\Big[N_1^*\int_0^1\int_0^{b/\ell}\phi_{n_0}\frac{\partial^2\phi_{n_0}}{\partial x^2}dxdy + \frac{\epsilon V_p^2}{d^3} + \omega_{n_0}^2\Big] \tag{6.21}$$

where ϕ_{n_0} is assumed to be normalized such that $\int_0^1\int_0^{b/\ell}\phi_{n_0}^2 dxdy = 1$. The result of equation (6.21) is a complex-valued number. The magnitude of the real part is a small perturbation to the natural frequency ω_{n_0}, which is negligible, while the magnitude of the imaginary part yields the damping of the system. The quality factor is related to ω_{n_0} and ω_{n_1} by

$$Q = \frac{\omega_{n_0} + \mathrm{Re}(\omega_{n_1})}{2\mathrm{Imag}(\omega_{n_1})} \tag{6.22}$$

where Re and Imag denote the real and imaginary parts, respectively.

For the special case of $N_1^* = 0$, equation (6.22) reduces to the following simple analytical expression for the quality factor, which is independent of the plate mode shapes:

$$Q = \frac{D\omega_{n_0}^2}{\mathrm{Imag}(D_t)\Big(\frac{\epsilon V_p^2}{d^3} + \omega_{n_0}^2\Big)} \tag{6.23}$$

where $\mathrm{Re}(\omega_{n_1})$ is neglected. We note from equation (6.23) that the electrostatic load

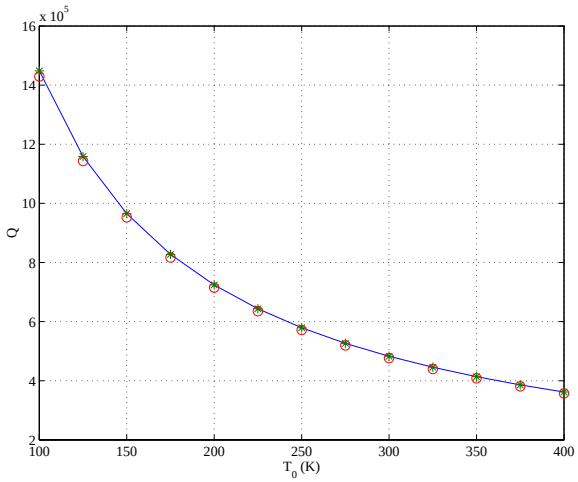

Figure 6.2: Comparison of the quality factors calculated using the present model (solid line) to those of Lifshitz and Roukes (2000) (stars) and Zener (1937) (circles) for various values of T_0.

amplifies the effect of thermoelastic damping.

Another case of interest is when $V_p = 0$, in which case the analytical expression for the quality factor reduces to the following simple expression:

$$Q = \frac{D}{\text{Imag}(D_t)} \tag{6.24}$$

which can be rewritten as

$$Q = \frac{h^3 \chi (1-\nu)}{12(1+\nu) E \alpha_t^2 T_0 \text{Imag}\left(\frac{h^3}{12} + \frac{h}{K_p^2} - \frac{2\tan(K_p h/2)}{K_p^3}\right)} \tag{6.25}$$

6.2 Results

We present numerical results for the quality factors of silicon plates due to thermoelastic damping for the special case of $V_p = 0$ and $N_1^* = 0$. We start with a plate clamped across its length and free across it width. In Figure 6.2, we set $\nu = 0$ in equation (6.25) (to approximate the case of a beam), calculate Q for various values of the temperature T_0, and compare the results (solid line) to those of Lifshitz and Roukes (2000) (stars) and Zener (1937) (circles). The results shown are for a microbeam with $\ell = 200\mu m$,

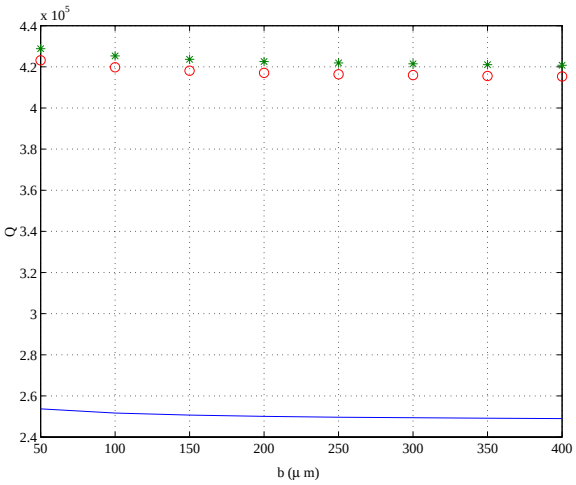

Figure 6.3: Comparison of the quality factors of the first mode calculated using the present model (solid line) to those of Lifshitz and Roukes (2000) (stars) and Zener (1937) (circles) for various values of b.

$b = 20\mu m$, and $h = 2\mu m$. We note full agreement among the results.

Figures 6.3 and 6.4 show the effect of varying the width of the plate on Q of the first and second modes, respectively. The plate specifications are $\ell = 200\mu m$, $h = 2\mu m$, $\nu = 0.3$, and $T_0 = 300K$. Figure 6.3 shows a comparison between the results of the plate model (solid line) to the models of Lifshitz and Roukes (2000) (stars) and Zener (1937) (circles). Clearly, the plate model predicts less quality factors than the beam model. Figure 6.3 shows that Q of the first mode changes slightly with the plate width. On the other hand, Figure 6.4 shows that Q of the second mode depends directly on the width of the plate. This is expected because, unlike the first eigenvalue, the second eigenvalue varies with the plate aspect ratio. Similar to Figure 6.3, the calculations show that the quality factor of the first mode using a plate model does not vary with the length of the plate. However, the quality factor is found to depend on Poisson's ratio ν. Figure 6.5 shows variation of the ratio of the quality factor, corresponding to the fundamental mode, of the beam model to that of the plate model with ν for a plate with $\ell = 200\mu m$, $b = 100\mu m$, $h = 5\mu m$, and $T_0 = 300K$.

Next, we consider thermoelastic damping in clamped plates. These plates cannot be simulated using a beam model, and hence the beam models (Zener, 1937; Lifshitz

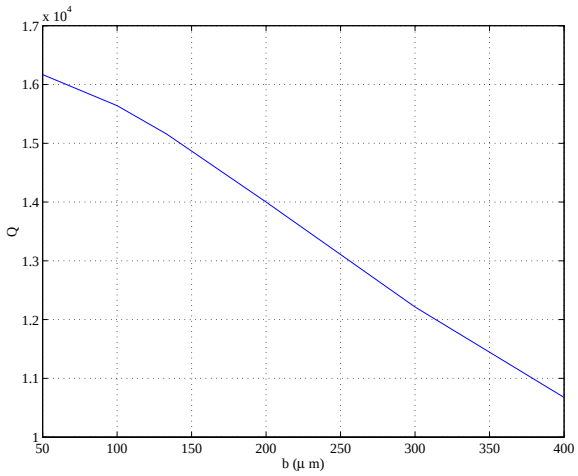

Figure 6.4: Variation of the quality factor of the second mode of a plate for various values of b.

and Roukes, 2000) for thermoelastic damping might not yield accurate results. Figures 6.6 and 6.7 show variation of Q of the first mode of a plate with T_0 and h, respectively. The plate specifications are $\ell = 200\mu m$, $b = 100\mu m$, and $\nu = 0.25$. We use $h = 1.5\mu m$ in Figure 6.6 and $T_0 = 300K$ in Figure 6.7. Figure 6.8 shows variation of Q of the first (circles) and second (stars) vibration modes with ℓ for the same microplate of Figure 6.7. Here we note that the quality factors of both modes are strong functions of the plate length because the corresponding natural frequencies are dependent on the plate aspect ratio.

6.2.1 Effect of the Electrostatic Forces and Residual Stresses

Next, we show the effect of electrostatic forces and residual stresses on the quality factor. We study the microplate of Figure 6.3. In Figure 6.9, we set the DC voltage equal to zero and calculate the quality factor for various values of the applied axial force. The figure shows that increasing the residual stresses increases the quality factor. In Figure 6.10, we set the axial force equal to zero, assume $d = 1.2\mu m$, and calculate the quality factor for various values of the DC voltage. The figure shows that increasing the electrostatic force decreases the quality factor, which is expected from equation (6.23). It shows a slight decrease in Q. However, as the value of V_p increases further

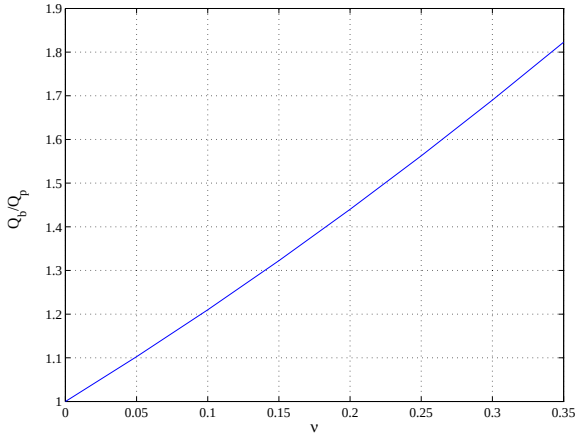

Figure 6.5: Variation of the ratio between the quality factor of the beam model (Zener, 1937; Lifshitz and Roukes, 2000) to that of the plate model for various values of ν.

toward the pull-in, the natural frequency approaches zero, and hence the quality factor vanishes. This is not seen in the figure because the present model assumes linearized electrostatic forces, and hence it is valid up to a voltage equal or less than 30% of the pull-in voltage (for the present case, the pull-in voltage is at $V_p \approx 44V$).

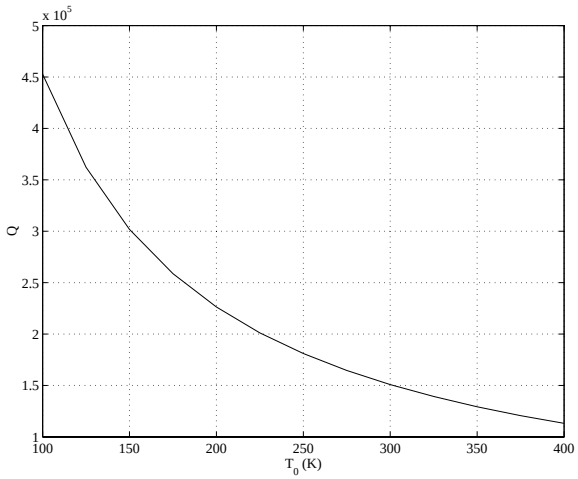

Figure 6.6: Variation of Q of the first mode of a fully clamped plate with T_0.

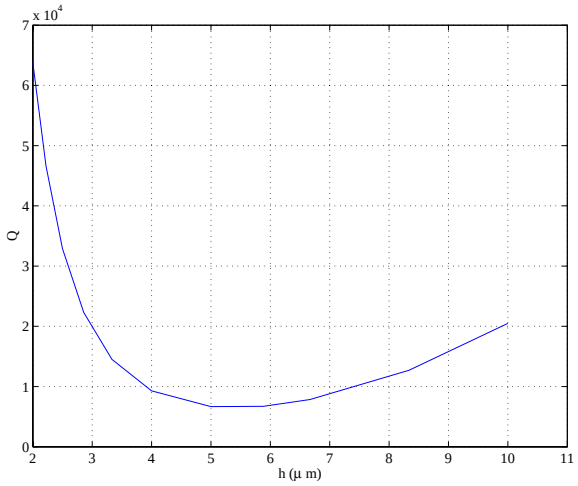

Figure 6.7: Variation of Q of the first mode of a fully clamped plate with h.

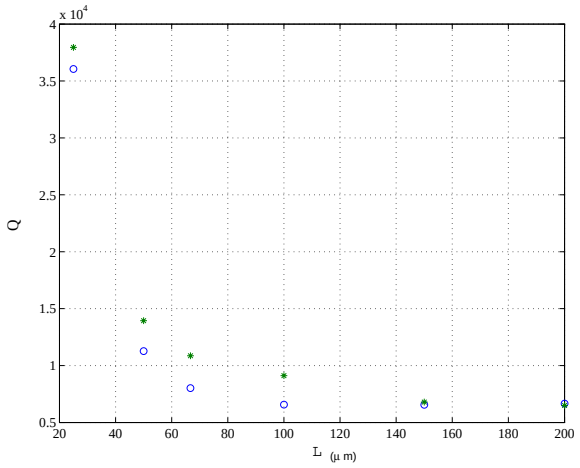

Figure 6.8: Variation of Q of the first (circles) and second (stars) modes with various values of ℓ.

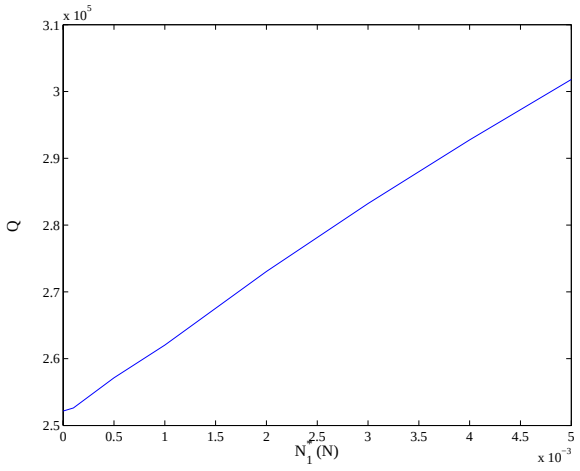

Figure 6.9: Variation of Q of the microplate of Figure 6.3 with N_1^*.

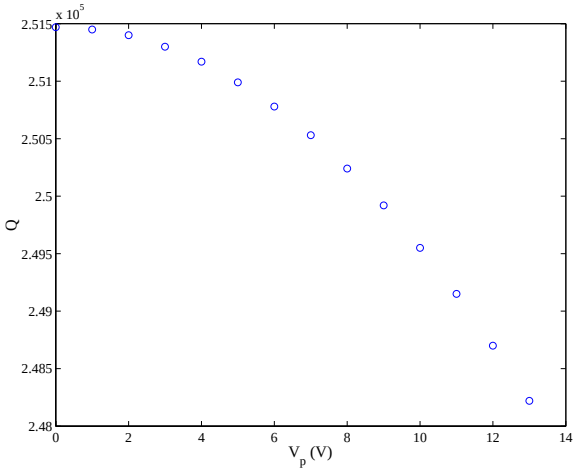

Figure 6.10: Variation of Q of the microplate of Figure 6.3 with V_p.

Chapter 7

Dynamics of MEMS Resonators and Switches under Primary-Resonance Excitation

In this chapter, we present a dynamic analysis and simulation of MEMS resonators and novel RF MEMS switches employing resonant microbeams. The resonators are excited near their fundamental natural frequencies (primary-resonance excitation). We study the dynamic pull-in instability and formulate safety criteria for the design of MEMS sensors and RF filters. We also utilize this phenomenon to design a low-voltage RF MEMS switch actuated with a combined DC and AC loading. The new switch uses a voltage much lower than the traditionally used DC voltage. Either the frequency or the amplitude of the AC loading can be adjusted to reduce the driving voltage and switching time. The new actuation method has the potential of solving the problem of high driving voltages of RF MEMS switches.

7.1 Problem Formulation

We consider a clamped-clamped microbeam, Figure 7.1, subject to a viscous damping with coefficient $\hat{c}$ per unit length and actuated by an electric load $v(t) = V_{DC} + V_{AC}\cos(\Omega t)$, where V_{DC} is the DC polarization voltage, V_{AC} is the amplitude of the

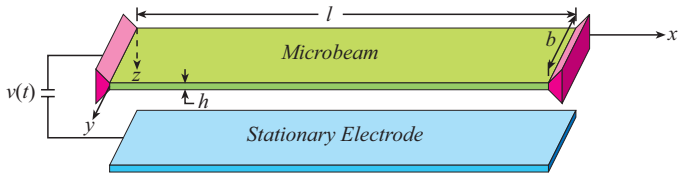

Figure 7.1: A schematic of an electrically actuated microbeam.

applied AC voltage, and Ω is the excitation frequency. The equation of motion that governs the transverse deflection $w(x,t)$ is written as

$$EI\frac{\partial^4 w}{\partial x^4}+\rho bh\frac{\partial^2 w}{\partial t^2}+\hat{c}\frac{\partial w}{\partial t}= \left[\frac{EA}{2\ell}\int_0^\ell\left(\frac{\partial w}{\partial x}\right)^2 dx+\hat{N}\right]\frac{\partial^2 w}{\partial x^2}+\frac{\epsilon b[V_{DC}+V_{AC}\cos(\Omega t)]^2}{2\left(d-w\right)^2} \tag{7.1}$$

where x is the position along the microbeam length, A and I are the area and moment of inertia of the cross section, E is Young's modulus, $\hat{N}$ is the applied tensile axial force, t is time, ρ is the material density, h is the microbeam thickness, d is the capacitor gap width, and ϵ is the dielectric constant of the gap medium. The last term in equation (7.1) represents an approximation of the electric force assuming a complete overlap of the area of the microbeam and the stationary electrode. The boundary conditions are

$$w(0,t)=w(\ell,t)=0, \qquad \frac{\partial w(0,t)}{\partial x}=\frac{\partial w(\ell,t)}{\partial x}=0 \tag{7.2}$$

For convenience, we introduce the nondimensional variables (denoted by hats)

$$\hat{w}=\frac{w}{d}, \quad \hat{x}=\frac{x}{\ell}, \quad \hat{t}=\frac{t}{T} \tag{7.3}$$

where $T=\sqrt{\frac{\rho bh\ell^4}{EI}}$. Substituting equation (7.3) into equations (7.1) and (7.2) and dropping the hats, we obtain

$$\frac{\partial^4 w}{\partial x^4}+\frac{\partial^2 w}{\partial t^2}+c\frac{\partial w}{\partial t}=\left[\alpha_1\Gamma(w,w)+N\right]\frac{\partial^2 w}{\partial x^2}+\frac{\alpha_2\left[V_{DC}+V_{AC}\cos(\Omega t)\right]^2}{\left(1-w\right)^2} \tag{7.4}$$

$$w(0,t)=w(1,t)=0, \quad \frac{\partial w}{\partial x}(0,t)=\frac{\partial w}{\partial x}(1,t)=0 \tag{7.5}$$

where the functional Γ is given by

$$\Gamma\left(f_1(x,t), f_2(x,t)\right) = \int_0^1 \frac{\partial f_1}{\partial x}\frac{\partial f_2}{\partial x} dx \tag{7.6}$$

The parameters appearing in equation (7.4) are

$$c = \frac{\hat{c}\ell^4}{EIT},\ \alpha_1 = 6\left(\frac{d}{h}\right)^2,\ N = \frac{\hat{N}\ell^2}{EI},\ \alpha_2 = \frac{6\epsilon\ell^4}{Eh^3d^3} \tag{7.7}$$

Next, we generate a reduced-order model (Younis et al., 2003) by discretizing equations (7.4) and (7.5) into a finite-degree-of-freedom system consisting of ordinary-differential equations in time. We use the undamped linear mode shapes of the straight microbeam as basis functions in the Galerkin procedure. To this end, we express the deflection as

$$w(x,t) = \sum_{i=1}^{M} u_i(t)\phi_i(x) \tag{7.8}$$

where $u_i(t)$ is the ith generalized coordinate and $\phi_i(x)$ is the ith linear undamped mode shape of the straight microbeam, normalized such that $\int_0^1 \phi_i\phi_j dx = \delta_{ij}$ and governed by

$$\phi_i^{iv} = N\phi_i'' + \omega_i^2\phi_i \tag{7.9}$$

$$\phi_i = 0 \text{ and } \phi_i' = 0 \quad \text{at} \quad x = 0 \text{ and } x = 1 \tag{7.10}$$

Here, ω_i is the ith natural frequency of the microbeam.

We multiply equation (7.4) by $\phi_n(x)(1-w)^2$, substitute equations (7.8) into the resulting equation, use equations (7.9) to eliminate ϕ_i^{iv}, integrate the outcome from $x = 0$ to 1, and obtain

$$\ddot{u}_n - 2\sum_{i,j=1}^{M} \ddot{u}_i u_j \int_0^1 \phi_i\phi_j\phi_n dx + \sum_{i,j,k=1}^{M} \ddot{u}_i u_j u_k \int_0^1 \phi_i\phi_j\phi_k\phi_n dx - c\dot{u}_n - \omega_n^2 u_n$$
$$= \alpha_2[V_{DC} + V_{AC}\cos(\Omega t)]^2 \int_0^1 \phi_n dx + 2\sum_{i,j=1}^{M} u_i u_j \omega_i^2 \int_0^1 \phi_i\phi_j\phi_n dx$$
$$- \sum_{i,j,k,=1}^{M} u_i u_j u_k \omega_i^2 \int_0^1 \phi_i\phi_j\phi_k\phi_n dx + 2\sum_{i,j=1}^{M} \dot{u}_i u_j \int_0^1 c\phi_i\phi_j\phi_n dx$$
$$- \sum_{i,j,k=1}^{M} \dot{u}_i u_j u_k \int_0^1 c\phi_i\phi_j\phi_k\phi_n dx + \alpha_1 \sum_{i,j,k=1}^{M} u_i u_j u_k \Gamma(\phi_i,\phi_j) \int_0^1 \phi_n\phi_k'' dx$$
$$- 2\alpha_1 \sum_{i,j,k,l=1}^{M} u_i u_j u_k u_l \Gamma(\phi_i,\phi_j) \int_0^1 \phi_k\phi_l''\phi_n dx$$
$$+ \alpha_1 \sum_{i,j,k,l,m=1}^{M} u_i u_j u_k u_l u_m \Gamma(\phi_i,\phi_j) \int_0^1 \phi_k''\phi_l\phi_m\phi_n dx$$
$$\text{for } n = 1, 2, \ldots, M \tag{7.11}$$

Equations (7.11) represent a discretized system of M coupled nonlinear ordinary-differential equations describing the dynamic behavior of an electrically actuated microbeam. Using three or more modes in equation (7.11) was shown (Younis et al., 2003) to give good convergence for the stable equilibria. Here, we use four modes in generating the results unless noted otherwise.

7.2 Results

We utilize three modes in the reduced-order model, equations (7.11), to calculate the equilibria of a microbeam under DC loading when $\ell = 510\mu m$, $h = 1.5\mu m$, $b = 100\mu m$, $d = 1.18\mu m$, and the nondimensional axial load $N = 8.7$. Details of the calculations are presented by Younis et al. (2003). Figure 7.2 shows the microbeam mid-point deflection W_{Max} versus the DC voltage. The stable (lower) branch and the unstable (upper) branch collide in a saddle-node bifurcation at the static pull-in instability $V_{DC} \approx 4.8V$, resulting in the destruction of both branches. This static analysis shows that MEMS resonators should be designed to operate below this value to ensure stability, while MEMS switches should be actuated by a DC voltage larger than this value to trigger

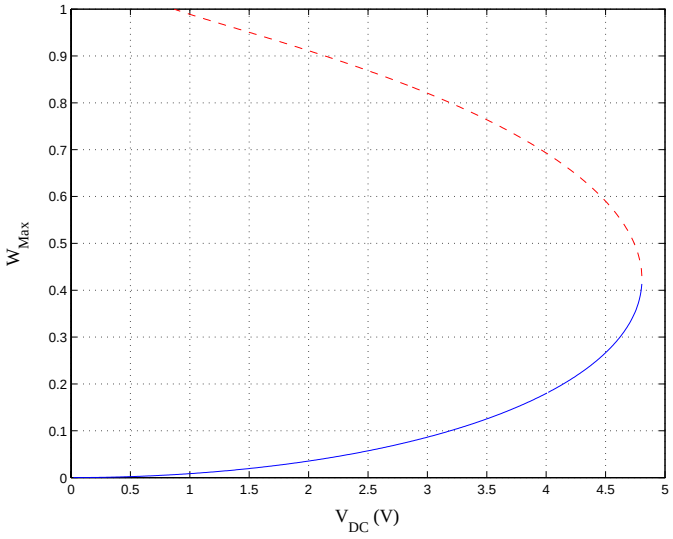

Figure 7.2: Equilibria of an electrostatically actuated microbeam, solid line: stable, dashed line: unstable.

pull-in.

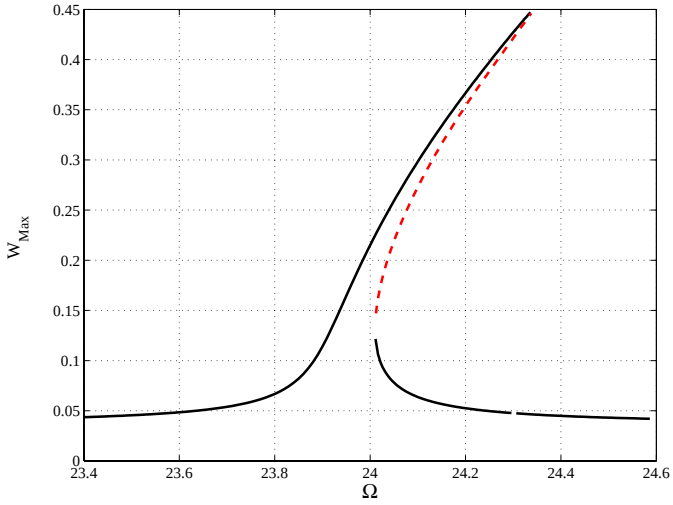

Figure 7.3: Frequency-response curves below the dynamic pull-in instability: $V_{DC} = 2V$ and $V_{AC} = 0.01V$.

Next, we study the dynamic behavior of the microbeam under an AC harmonic excitation near its fundamental natural frequency $\omega_1 = 23.9$. We assume a quality factor $Q = 1000$, which is related to the damping coefficient by $c = \omega_1/Q$. We use a

shooting method (Nayfeh and Balachandran, 1995) to find periodic solutions of equations (7.11) and study their stability using Floquet theory (Nayfeh and Balachandran, 1995). Because this method is valid for general initial conditions and excitations, we refer to it, in conjunction with the direct integration of the equations of motion, as a global approach. In Figure 7.3, we show variation of the dynamic response amplitude W_{Max} of the microbeam with the frequency of excitation when $V_{DC} = 2V$ and $V_{AC} = 0.01V$. The solid curves denote stable branches and the dashed curve denotes an unstable branch. It follows from Figure 7.3 that the nonlinear resonance frequency is near 24.337, where one of the Floquet multipliers approaches unity. There is no indication in the figure of a dynamic pull-in.

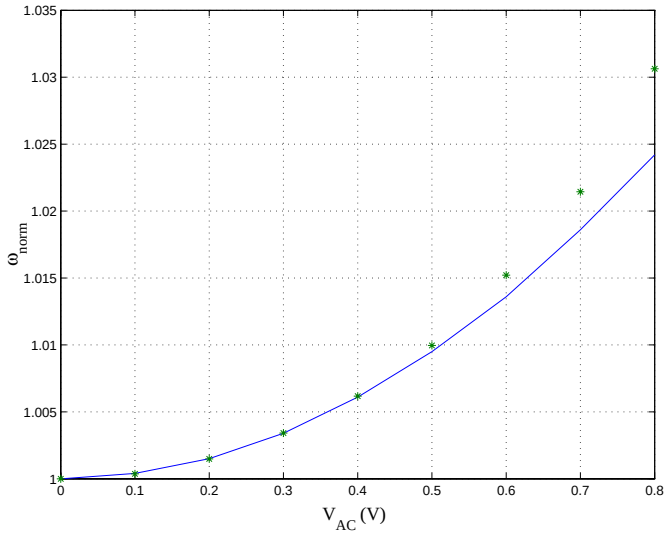

Figure 7.4: Variation of the normalized nonlinear resonance frequency with the amplitude of AC loading, solid curve: perturbation approach, stars: global approach.

In Figure 7.4, we show variation of the nonlinear resonance frequency normalized with respect to the natural frequency $\omega_1 = 26.9523$ of a microbeam of $\ell = 310\mu m$ with the excitation amplitude V_{AC}. The quality factor is $Q = 151$ and the rest of specifications are the same as those used in Figure 7.3. The solid line is calculated using the perturbation-based model (Younis and Nayfeh, 2003) and the stars are calculated using the global approach. Figure 7.4 shows that there is good agreement for AC excitation amplitudes up to $V_{AC} = 0.4V$.

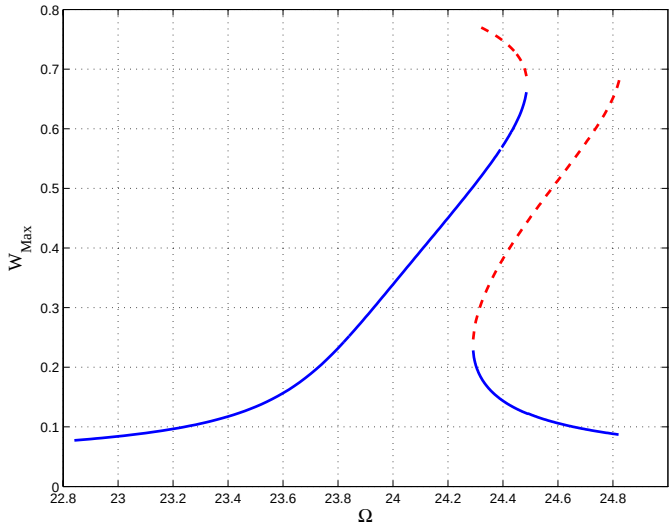

Figure 7.5: Frequency-response curves showing the onset of the dynamic pull-in.

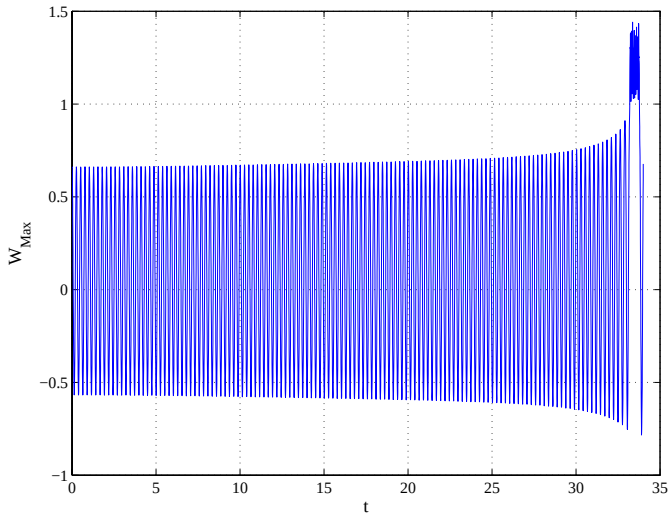

Figure 7.6: Long-time integration results near the upper saddle-node bifurcation of Figure 7.5.

Next, we study the device of Figure 7.2 actuated by a DC loading $V_{DC} = 2V$. Figure 7.5 shows variation of W_{Max} with Ω when $V_{AC} = 0.1V$ and $Q = 1000$. The solid curves denote stable branches and the dashed curves denote unstable branches. The dynamic pull-in instability is characterized by a slope approaching infinity, where a Floquet multiplier approaches unity. We note from the figure that the dynamic pull-in

corresponds to a saddle-node bifurcation at $\Omega = 24.4857$, where a stable branch collides with an unstable branch leading to their destruction. Therefore, if the frequency of excitation is swept from low values to beyond the above value, so that the response follows the upper stable branch, the system will go to pull-in. As an example, we show in Figure 7.6 long-time integration of equations (7.11) for a set of initial conditions near the saddle-node bifurcation with $\Omega = 24.4897$, which exceeds slightly the bifurcation threshold. It is clear that the system stays for a while around the previous stable solution (its "ghost" (Nayfeh and Balachandran, 1995)) before it undergoes the pull-in instability.

Figure 7.5 shows another saddle-node bifurcation at $\Omega \approx 24.2917$, where also a Floquet multiplier approaches unity. This bifurcation can lead to undesirable phenomena, such as jumps and hysteresis, in devices like resonant microsensors. The present global approach can be used to predict the location of the jump and hysteretic points. If the solution jumps from the lower branch it either goes directly to a pull-in instability or settles down on the upper stable branch corresponding to a stable periodic motion of larger amplitude. This depends on the transient dynamics of the system, which in turn depends on several factors, such as the sweeping rate of Ω, the ramping rate of V_{AC}, and any external disturbances in the system. In Figures 7.7a and 7.7b, we show time-history evolutions for a point that is initially close to the lower saddle-node bifurcation of Figure 7.5 ($\Omega \approx 24.2917$, $W_{Max} = 0.23$). The time is nondimensionalized with respect to $T = 7.1195 \times 10^{-5} s$. The figures are generated from a long-time integration of equations (7.11). In Figure 7.7a, $\dot{u}_1 = 0.2$ and in Figure 7.7b $\dot{u}_1 = 0.23$. We note from Figure 7.7a that the time integration yields a stable solution corresponding to a point on the lower stable branch of Figure 7.5, and hence the system does not exhibit any jumps. On the other hand, Figure 7.7b shows that the system jumps to the pull-in instability. As mentioned previously, a third possibility exists in which the system settles down on the upper stable branch of Figure 7.5. However, in the present case, the domain of attraction of the stable upper branch is very small (because W_{Max} at $\Omega \approx 24.2917$ is very large), and hence it is hard for the system to jump to this state physically.

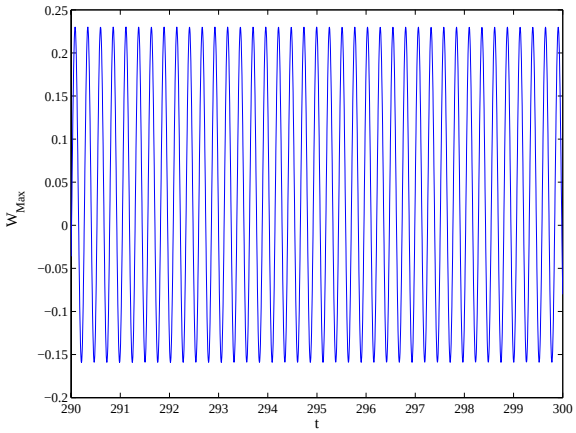

(a) $\dot{u}_1 = 0.2$.

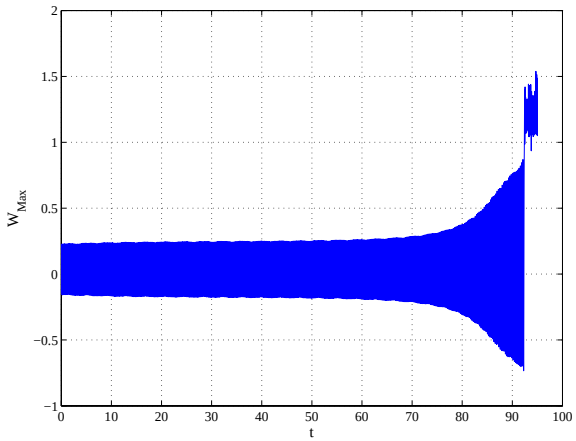

(b) $\dot{u}_1 = 0.23$.

Figure 7.7: Long-time integration results for the lower saddle-node bifurcation of Figure 7.5 and two different initial velocities.

Figure 7.8 shows variation of W_{Max} with V_{AC} when $V_{DC} = 2V$, $\Omega = 24.16$, and $Q = 1000$. The dashed curves denote unstable branches. Here there is a dynamic pull-in at $V_{AC} \approx 0.2819V$, where the slope of the curve approaches infinity and a Floquet multiplier approaches unity. We note that the magnitude of the Floquet multiplier can be used as a pull-in criterion only for force sweep cases, like that in Figure 7.8, because a Floquet multiplier tends to unity as the curve in a frequency sweep reaches

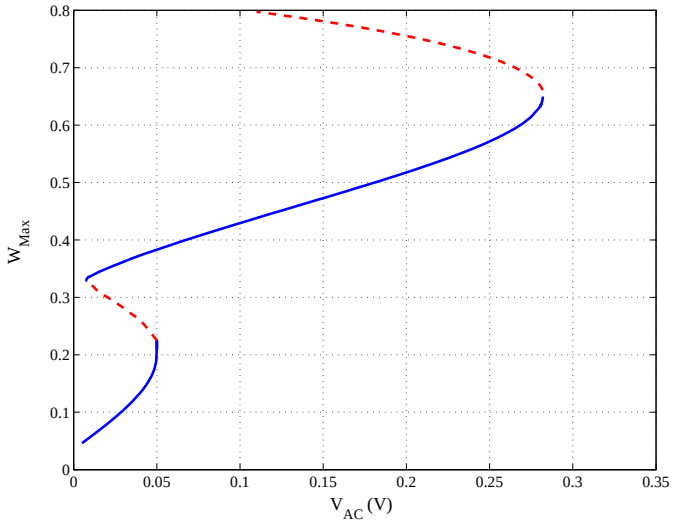

Figure 7.8: Force-response curves showing the onset of the dynamic pull-in when $Q = 1000$.

a maximum value, regardless of whether there is a pull-in (Figure 7.5) or a cyclic-fold bifurcation (Figure 7.3).

Figure 7.8 shows two other saddle-node bifurcations at $V_{AC} = 0.0498070V$ and $V_{AC} = 0.00738V$, where also a Floquet multiplier approaches unity. These bifurcations can lead to undesirable phenomena, such as jumps and hysteresis. Figures 7.9a and 7.9b show examples of two possible jump scenarios for these bifurcations. The excitation amplitudes are $V_{AC} = 0.05V$ and $V_{AC} = 0.00732V$, which are slightly different from the above bifurcation thresholds. It is obvious that the ensuing motion after the jump experiences a transient behavior, after which the system settles to a totally different motion from the one before the jump. Therfore, devices like resonant microsensors have to be designed to operate away from these bifurcations. Further, these jumps may lead to pull-in due to external distrubances (as in the case of Figure 7.7b).

Figures 7.5 and 7.8 show that the dynamic pull-in instability occurs at a voltage much lower than the static pull-in voltage 4.8 V. The maximum dynamic pull-in voltage is less than 2.3 V. This result illustrates the importance of designing RF MEMS filters and resonant sensors based on a dynamic analysis to avoid the possibility of dynamic failures of these devices. Also, the results suggest a novel dynamic actuation method

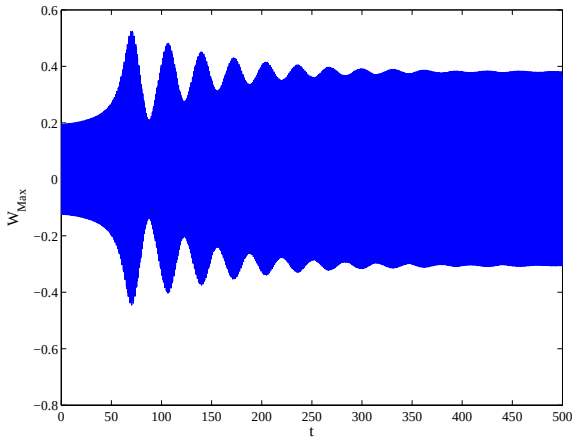

(a) $V_{AC} = 0.05V$, $\dot{u}_1 = 0.213207$.

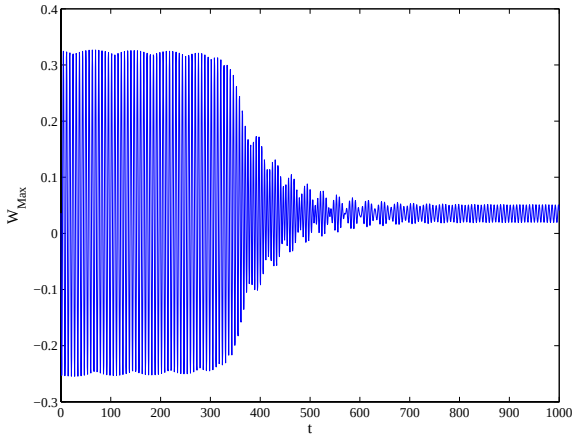

(b) $V_{AC} = 0.00732V$, $\dot{u}_1 = 4.448$.

Figure 7.9: Long-time integration results for the two lower saddle-node bifurcations of Figure 7.8.

for RF MEMS switches, in which the pull-in voltage is much less than the static pull-in voltage. This is a very promising result in the search to reduce the actuation level of RF MEMS switches.

Figure 7.10 shows variation of W_{Max} with V_{AC} for the same parameters of Figure 7.8 but with $Q = 100$. It shows that decreasing the quality factor by an order of magnitude eliminates the unstable branch and the undesirable nonlinear phenomena

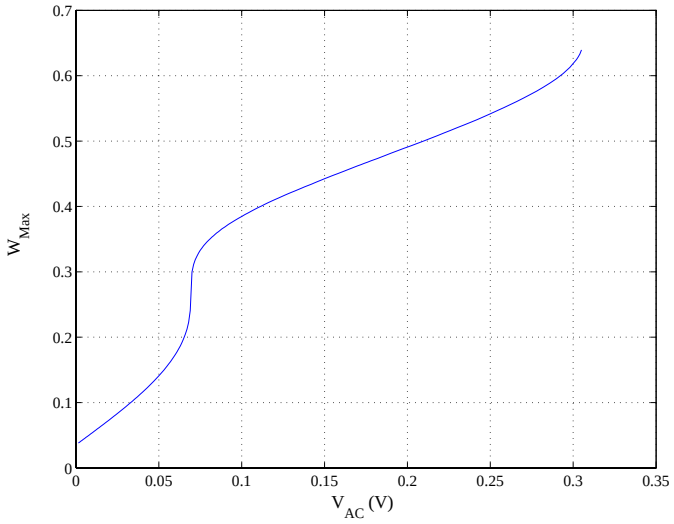

Figure 7.10: Force-response curves for the parameters of Figure 7.8 with $Q = 100$.

(the hysteresis and jumps). We note from Figures 7.10 and 7.8 that packaging requirements of the switch can be relaxed significantly at the expense of a slight increase in the electric loading, which triggers pull-in.

Next, we illustrate another pull-in scenario. Figures 7.11a and 7.11b show a time-history evolution and a phase portrait for the parameters of Figure 7.8 when $V_{AC} = 0.09V$. We note that dynamic pull-in occurs below $V_{AC} \approx 0.2819V$, resulting from a saddle-node bifurcation. We note that the initial conditions of Figures 7.11 are different from those used in Figure 7.8. Further, the results of Figure 7.8 represent steady-state responses to a harmonic excitation, and hence the transient effects are not accounted for. For the case of Figure 7.11, the dynamic pull-in occurs when the stable periodic orbit around the stable equilibrium collides with the saddle (the unstable equilibrium solution) and its stable manifold, which is at $W_{Max} \approx 0.91$ (compare the location of the saddle in Figures 7.2, 7.11a, and 7.11b). Figures 7.12a and 7.12b are generated from the same data of Figures 7.11 except that the sign of one initial condition is changed from positive to negative. We note that the motion is stable, which indicates a fractal dynamical behavior that is sensitive to initial conditions (Nayfeh and Balachandran, 1995).

In light of the above results, we make the following remarks about the dynamic pull-

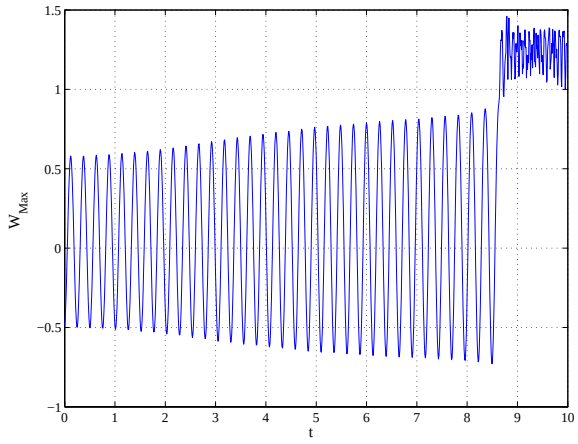

(a) Time history.

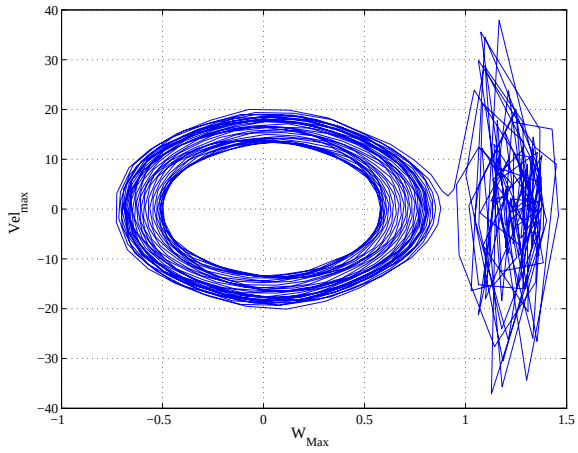

(b) Phase portrait.

Figure 7.11: Long-time integration results showing the onset of dynamic pull-in.

in phenomenon. There are at least three scenarios for the dynamic pull-in instability. The first scenario is for the case of steady-state response, in which pull-in occurs due to a saddle-node bifurcation, as in Figures 7.5 and 7.8. Because in this scenario no transient effects or abrupt changes in the initial conditions are taken into account, the stability limits predicted by this scenario represent upper limits to the dynamic pull-in, beyond which no stable motion can exist. The other two scenarios are more

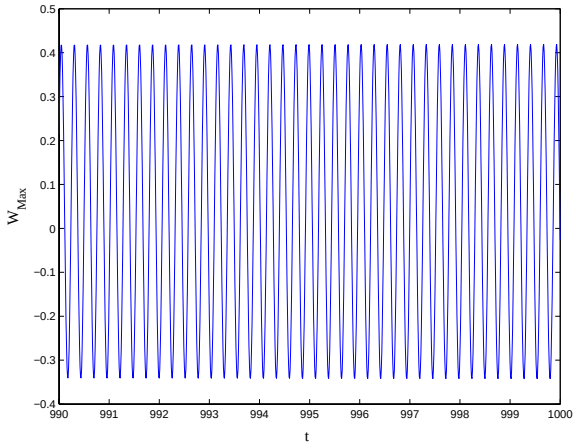

(a) Time history.

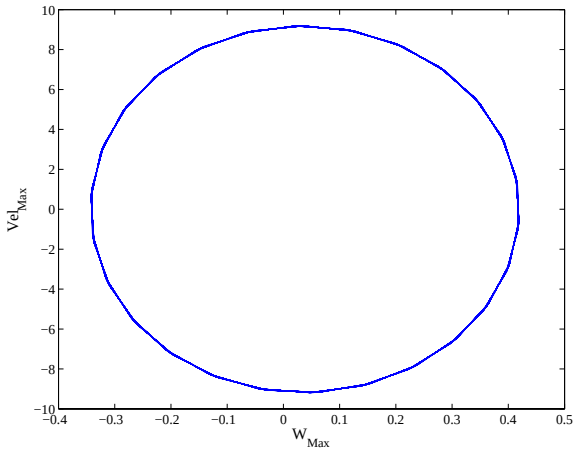

(b) Phase portrait.

Figure 7.12: Long-time integration results for the same parameters of Figures 7.8 and different initial conditions.

subtle and depend strongly on the initial conditions of the device, such as in Figures 7.7, 7.11, and 7.12. In the second scenario, the system jumps directly from a lower stable branch to the pull-in instability (like the case of Figure 7.7b).

To explain the third scenario, we consider first the free vibration of a microbeam deflected under a DC loading. In the absence of forcing and damping, a homoclinic orbit (Nayfeh and Balachandran, 1995) in the state plane representing the midpoint of

the beam, which starts and ends at the saddle, encircles the stable fixed point (center). This orbit is composed of a stable manifold and an unstable manifold that intersect nontransversely away from the saddle. Any initial conditions inside the closed orbit result in a stable oscillatory motion and any initial conditions outside it result in an unstable motion (and hence such an orbit is called a seperatix (Nayfeh and Balachandran, 1995) because it separates different kinds of behaviors). In the presence of damping, the center becomes a stable focus, the saddle remains a saddle, and the homoclinic orbit is destroyed. Here, the stable and unstable manifolds do not intersect. If the system is excited by an AC force in the stable regime near the stable focus, the motion will be a stable periodic motion. As the AC forcing and thus the amplitude of excitation increases, the stable manifold approaches the unstable manifold. Eventually, both manifolds intersect transversally infinitely many times, resulting in a complex dynamic behavior called homoclinic tangles (Nayfeh and Balachandran, 1995). One implication of this complex behavior is the sensitivity to initial conditions or the unpredictability of motion. Increasing the amplitude of excitation further results in an erosion of the basin of attraction of bounded motions; and the possibility of finding a set of initial conditions that leads to a stable motion decreases. It is worth noting that the dynamic pull-in instability is to a great extent similar to the problem of capsizing of ships (Nayfeh and Balachandran, 1995; Nayfeh and Sanchez, 1988).

Next, we generate the stability map for the microbeam as a function of V_{DC}, V_{AC}, and the frequency detuning parameter $\sigma = \Omega - \omega_1$. For the device of Figure 7.2, the sign of the system 'effective' nonlinearity (Younis and Nayfeh, 2003) changes from positive, corresponding to a hardening behavior, to negative, corresponding to a softening behavior near $V_{DC} = 3.25V$. We use the force-sweep approach to determine the onset of pull-in, which corresponds to a saddle-node bifurcation. Figure 7.13 shows the stability map, any voltage combination above a constant σ line will cause pull-in. For example, when $\sigma = 0.5$, Figure 7.13 indicates that no stable motion can exist beyond $V_{DC} = 2.2V$ for any value of V_{AC}. The stability limits should be taken with caution because of the aforementioned sensitivity to initial conditions, which might result in pull-in earlier than predicted here (as in Figures 7.7a, 7.11a, and 7.11b).

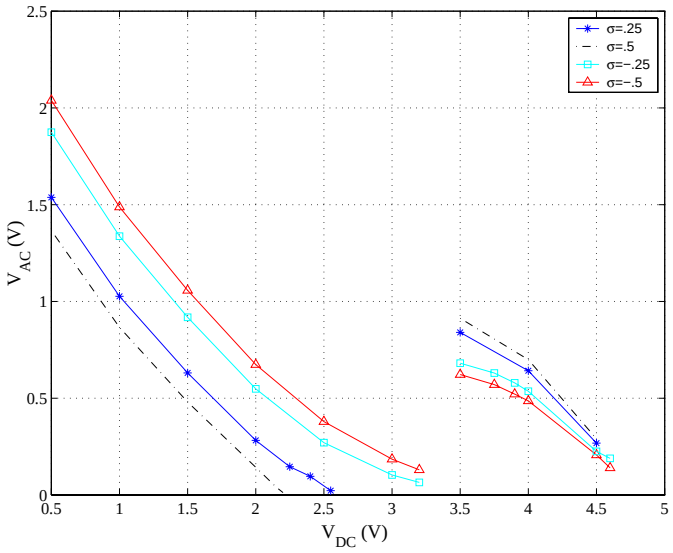

Figure 7.13: The stability map, any load above a constant σ line will cause pull-in.

The discontinuity seen in the figure is a result of the change in the sign of the effective nonlinearity. The results on the right side of the figure are for the case of softening-type effective nonlinearity. The dynamic pull-in mechanism in this case differs from that in the case of the hardening-type effective nonlinearity. Here, as the pull-in is approached, we found that a Floquet multiplier exits the unit circle through -1, indicating a period-doubling bifurcation. The new period-two motion immediately looses stability through a cyclic-fold bifurcation, with a Floquet multiplier exiting the unit circle along the real axis through +1. Similar behaviors were reported in the problem of capsizing of ships (Nayfeh and Balachandran, 1995). An example of a case with a softening-type effective nonlinearity is shown in Figure 7.14 for $V_{DC} = 4V$ and $\sigma = -0.5$.

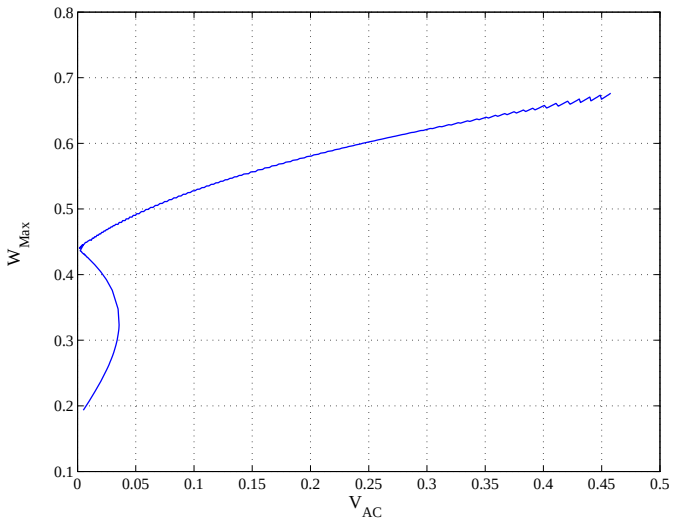

Figure 7.14: A force-response curve for a case with a softening-type effective nonlinearity.

Chapter 8

Dynamics of MEMS Resonators under Superharmonic and Subharmonic Excitations

This chapter is an extension to the previous chapter, which deals with primary-resonance excitation of an electrically actuated microbeam. Here, we consider secondary-resonance excitations. We simulate the dynamics of microbeams excited near half their fundamental natural frequencies (superharmonic excitation) and twice their fundamental natural frequencies (subharmonic excitation). For the superharmonic case, we present results showing the effect of varying the DC bias, the damping, and the AC excitation amplitude on the frequency-response curves. We show that the dynamic pull-in phenomenon can occur for a superharmonic excitation at an electric load much lower than that predicted based on static analysis. For the subharmonic case, we show that all frequency-response curves reach pull-in regardless of the magnitude of the AC forcing.

8.1 Superharmonic Excitation

We first study the case of a superharmonic excitation. We consider a clamped-clamped microbeam (see Figure 7.1) actuated by an electric load ($V_{DC} + V_{AC}\cos\Omega t$), where

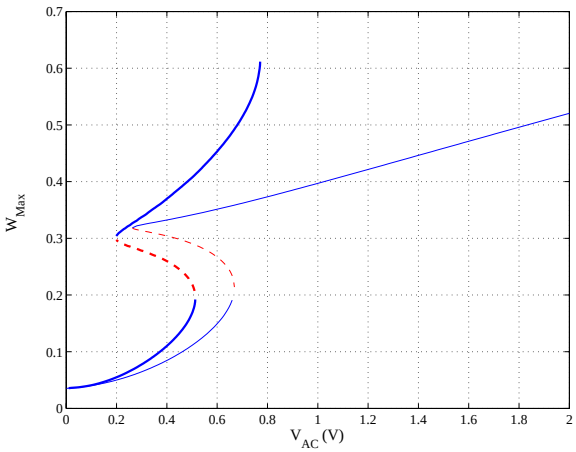

Figure 8.1: Force-response curves obtained using the global approach (heavy curves) and the perturbation-based approximation (thin curves).

$\Omega \approx \frac{1}{2}\omega_1$. We study a microbeam with $\ell = 510\mu m$, $h = 1.5\mu m$, $b = 100\mu m$, $d = 1.18\mu m$, subject to a nondimensional axial load of $N = 8.7$. According to the static analysis in Chapter 7, the pull-in voltage for this beam is $V_{DC} \approx 4.8V$. We apply a shooting method to the reduced-order mode, equation (7.11), to find the steady-state motions (periodic solutions) and study their stability using Floquet theory (Nayfeh and Balachandran, 1995).

In Figure 8.1, we show variation of the response amplitude W_{Max} of the microbeam mid-point ($\hat{x} = \frac{1}{2}\ell$) with the amplitude of excitation V_{AC} at $\Omega = 12.15$. A DC voltage $V_{DC} = 2.0$ is applied to bias the beam, as a result its fundamental natural frequency was found to be $\omega_1 = 23.9$. We assume a quality factor $Q = 1000$, where Q is related to the damping coefficient by $c = \omega_1/Q$. In all figures, the solid curves denote stable solutions and the dashed curves denote unstable solutions. The results of the reduced-order model (global approach) are shown in heavy curves wheres the results of the perturbation-based approximate solution (Abdel-Rahman and Nayfeh, 2003) are shown in thin curves. The analytical solution yields results in good agreement with those obtained from the reduced-order model for small motions. The dynamic pull-in instability is characterized by a slope approaching infinity, at which we found a Floquet multiplier approaching unity. Pull-in can be observed in the results of the

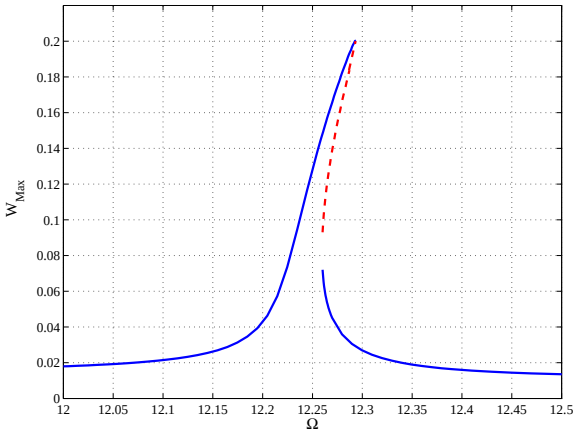

Figure 8.2: Frequency-response curve when $V_{DC} = 1.0V$, $V_{AC} = 0.2V$, and $Q = 1000$.

reduced-order model, at $V_{AC} = 0.79V$, but not in the approximate solution. Under dynamic loading (AC voltage), the instability occurs at a much lower voltage than under static loading (DC voltage) conditions. It is worth noting that for the case of a primary-resonance excitation $\Omega \approx \omega_1$, we found in Chapter 7 that the dynamic pull-in occurs at $V_{DC} = 2.0V$, $V_{AC} = 0.28V$, and $\Omega = 24.16$. So, while the amplitude of the AC voltage corresponding to dynamic pull-in is larger for a superharmonic excitation than it is for a primary excitation, they are of the same order of magnitude.

In Figure 8.2, we show variation of W_{Max} with the frequency of excitation (frequency-response curve) when $V_{DC} = 1.0V$, $V_{AC} = 0.2V$, and $Q = 1000$. The fundamental natural frequency of the microbeam was found to be $\omega_1 = 24.448$ in this case. Figure 8.2 shows a nonlinear resonance frequency $\Omega_r \approx 12.2937$ and a corresponding maximum deflection $W_{Max} \approx 0.2$, where we found that one of the Floquet multipliers approaches unity.

We obtained the frequency-response curve, Figure 8.3, at a higher bias voltage $V_{DC} = 2.0V$ and for the same parameters in Figure 8.2. The increase in the bias voltage resulted in a decrease in the fundamental natural frequency to $\omega_1 = 23.9$ and the nonlinear resonance frequency to $\Omega_r \approx 12.06$. Meanwhile, the static deflection of the microbeam is increased slightly, from 0.0084 to 0.035, while the maximum amplitude of the response is increased significantly from $W_{Max} \approx 0.20$ to $W_{Max} \approx 0.30$. These

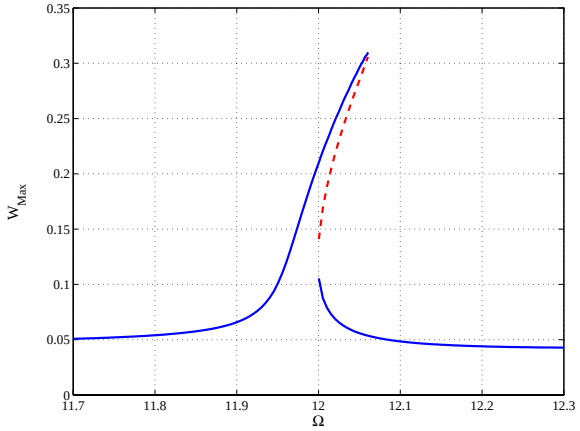

Figure 8.3: Frequency-response curve when $V_{DC} = 2.0V$, $V_{AC} = 0.2V$, and $Q = 1000$.

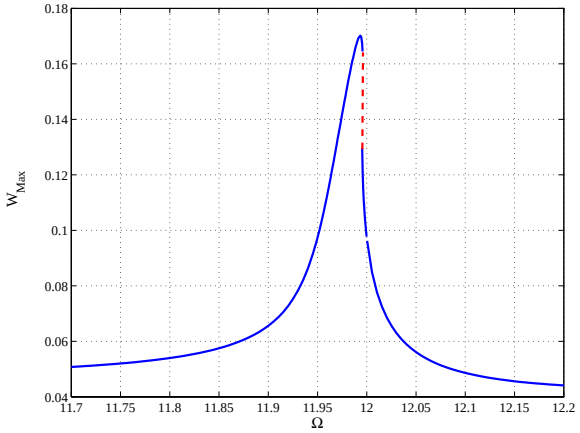

Figure 8.4: Frequency-response curves when $V_{DC} = 2.0V$, $V_{AC} = 0.2V$, and $Q = 500$.

results indicate that increasing V_{DC} leads not only to a decrease in the microbeam stiffness, and thus ω_1 and an increase in its static deflection, but also to an amplification of the effect of V_{AC}.

To examine the effect of changes in the quality factor on the microbeam response, we obtained, in Figure 8.4, the frequency-response curve for the same parameters in Figure 8.3 with $Q = 500$. Doubling the damping lowered the maximum amplitude from $W_{Max} \approx 0.30$ to 0.17 and the resonance frequency from $\Omega_r \approx 12.06$ to 11.99.

We demonstrate in Figure 8.5 the dynamic pull-in during a frequency sweep. The parameters in Figure 8.5 are the same as those in Figure 8.3 with the exception of

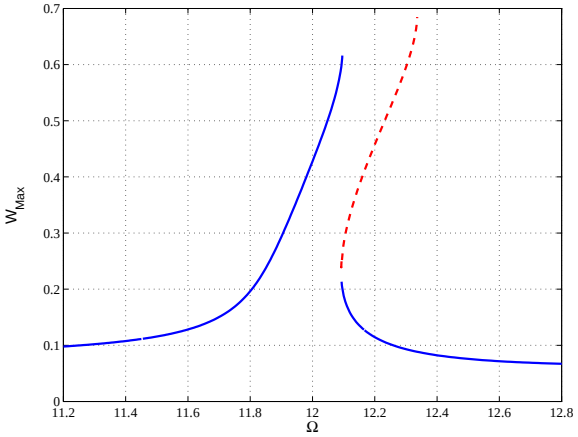

Figure 8.5: Frequency-response curve exhibiting dynamic pull-in.

$V_{AC} = 0.7V$. There is a gap in the frequency-response curve because both of the stable and unstable branches terminate as W_{Max} exceeds 0.6 and pull-in develops. As in Figure 8.1, the dynamic pull-in instability here is characterized by a slope approaching infinity and a Floquet multiplier approaching unity.

In Figures 8.6-8.8, we show the phase portraits (plots of the velocity Vel_{Max} versus deflection W_{Max} of the microbeam mid-point) for selected points on Figure 8.5. Figure 8.6 shows periodic orbits of three points on the stable upper branch of Figure 8.5. The size of the orbit increases as the excitation frequency increases until it reaches a maximum value $W_{Max} \approx 0.64$ at $\Omega = 12.0905$. Beyond this point, the upper branch disappears because the orbit size becomes so large that it triggers pull-in. Figure 8.7 shows periodic orbits of two points on the unstable branch of Figure 8.5. The orbit size increases from $W_{Max} \approx 0.235$ at the bifurcation point to $W_{Max} \approx 0.68$. Beyond this point, the unstable branch disappears due to pull-in. Figure 8.8 shows periodic orbits of two points on the stable lower branch of Figure 8.5. The size of the orbit decreases, from $W_{Max} \approx 0.2$ near the bifurcation point, as the excitation frequency Ω increases. Beyond $\Omega = 12.4$, the orbit size $W_{Max} \approx 0.08$ becomes almost constant as the excitation frequency Ω increases.

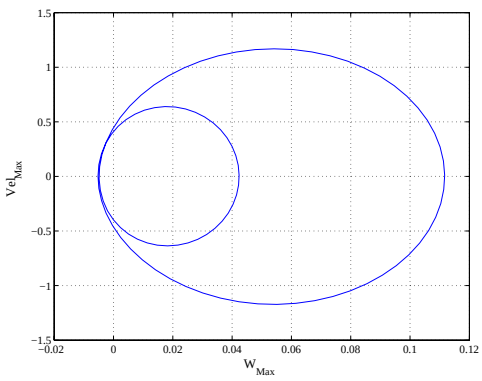

(a) $\Omega = 11.4500$.

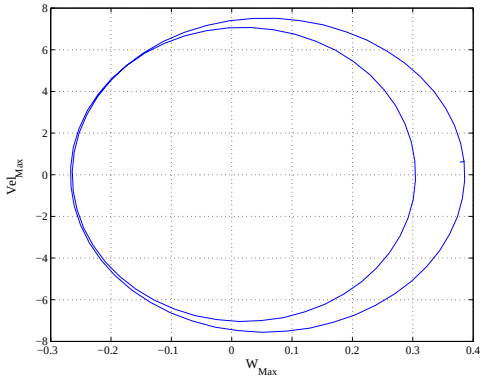

(b) $\Omega = 11.9650$.

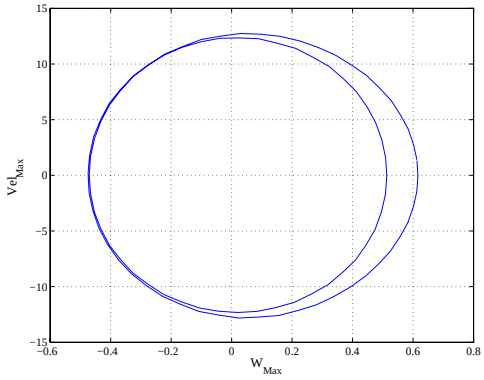

(c) $\Omega = 12.0905$.

Figure 8.6: Phase portraits for three points on the upper stable branch of Figure 8.5.

8.2 Subharmonic Excitation

In this section, we study the response of an electrically actuated microbeam under a subharmonic excitation. We consider the same clamped-clamped microbeam of Section 8.1 with a frequency of excitation $\Omega \approx 2\omega_1$. In all figures, the solid curves denote stable solutions and the dashed curves denote unstable solutions. Figures 8.9 show frequency-response curves when $V_{AC} = 0.2V$ obtained using the global approach (Figure 8.9a) and the analytical approximation (Figure 8.9b) of Abdel-Rahman and Nayfeh (2003). The analytical solution yields results close to those obtained from the reduced-order

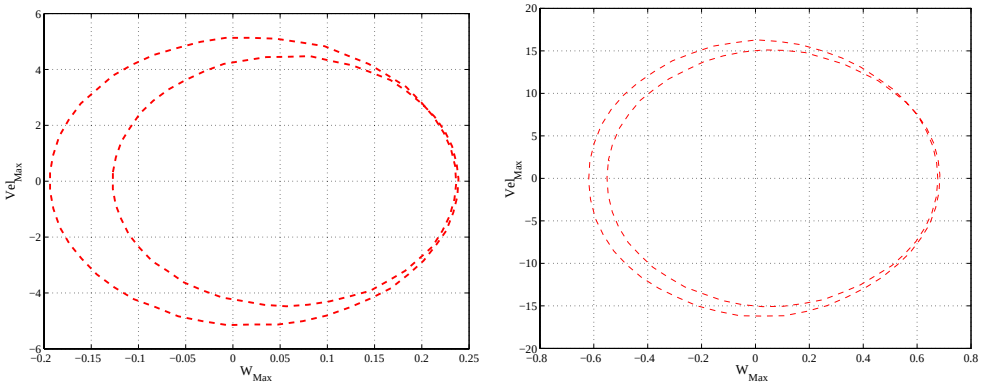

(a) $\Omega = 12.0870$. (b) $\Omega = 12.3310$.

Figure 8.7: Phase portraits for two points on the unstable branch of Figure 8.5. Dashed curves denote unstable orbits.

model for small motions. The dynamic pull-in instability is observed only in the global approach results (Figure 8.9a). It is characterized by a slope approaching infinity at $\Omega \approx 49$, at which we found a Floquet multiplier approaching unity.

Figure 8.10 shows a frequency-response curve when $V_{AC} = 0.1V$. Although the AC forcing is reduced to half the value of Figure 8.9, we note that the curve is terminated by the pull-in instability. The frequency at pull-in in this case shifts slightly to $\Omega \approx 49.16$.

Based on perturbation analysis (Nayfeh, 1981; Abdel-Rahman and Nayfeh, 2003), for this example, the subharmonic resonance is activated when $V_{AC} \geq 0.068V$. Figure 8.11 shows another frequency-response curve when $V_{AC} = 0.07V$, which is slightly above the activation threshold. We observe that the pull-in instability occurs at $\Omega \approx 49.21$. We conclude from the above results that all frequency-response curves of an electrically actuated microbeam excited at subharmonic resonance of order 2 exhibit pull-in regardless of the magnitude of the AC forcing.

Figure 8.12 shows a force-response curve at a frequency of excitation $\Omega = 47.85$. We note that pull-in occurs at $V_{AC} = 0.86V$, where we found a Floquet multiplier approaching unity. The value of the AC forcing is relatively high compared to the primary resonance and superharmonic cases. The reason for this is because Ω for this case is very close to twice the linear natural frequency $\Omega = 47.8$. Hence, according to

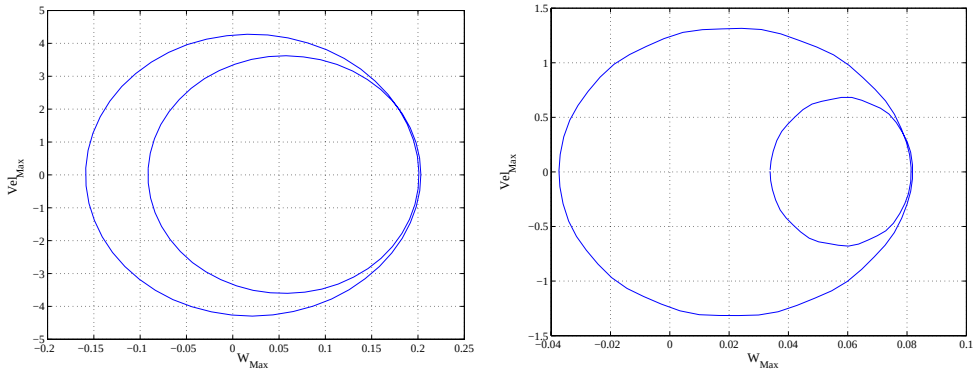

(a) $\Omega = 12.09$. (b) $\Omega = 12.40$.

Figure 8.8: Phase portraits for two points on the lower stable branch of Figure 8.5.

Figures 8.9-8.11, W_{Max} at Ω is small, which means that it requires a large value of V_{AC} to trigger pull-in. However, if we increase the value of Ω and regenerate the force-response curve, we will find that pull-in is triggered at lower values. For examples, we found pull-in occurs at $V_{AC} = 0.74V$, $V_{AC} = 0.296V$, and $V_{AC} = 0.178V$ for $\Omega = 48.05$, $\Omega = 48.8$, and $\Omega = 49$, respectively.

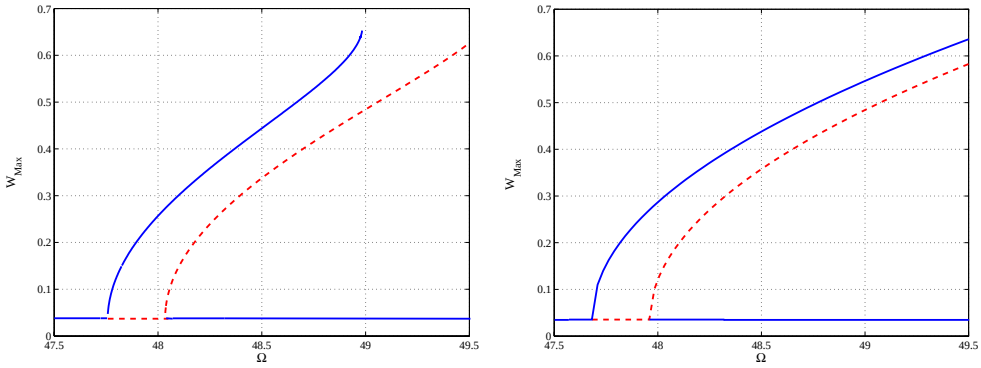

(a) Global approach.

(b) Perturbation approach.

Figure 8.9: Frequency-response curves when $V_{DC} = 2.0V$, $Q = 1000$, and $V_{AC} = 0.2V$.

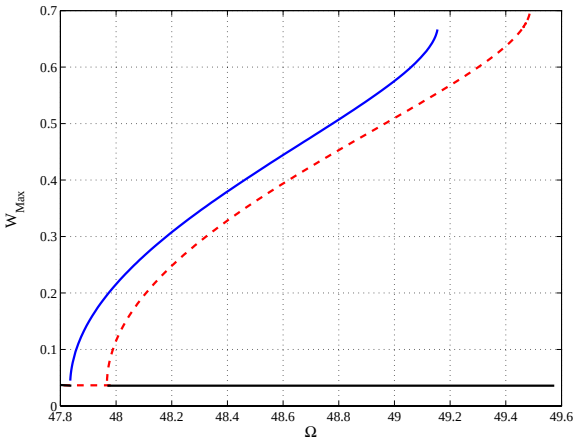

Figure 8.10: Frequency-response curve when $V_{DC} = 2.0V$, $Q = 1000$, and $V_{AC} = 0.1V$.

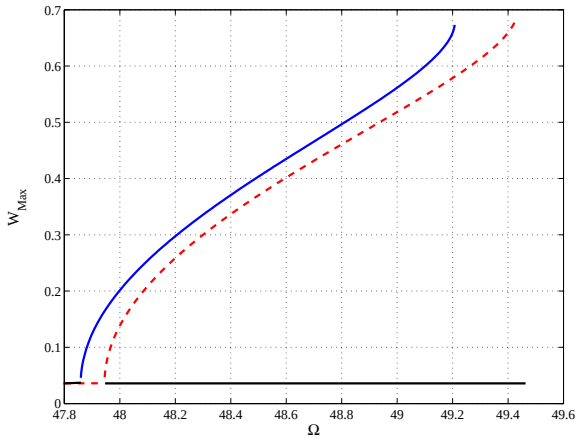

Figure 8.11: Frequency-response curve when $V_{DC} = 2.0V$, $Q = 1000$, and $V_{AC} = 0.07V$.

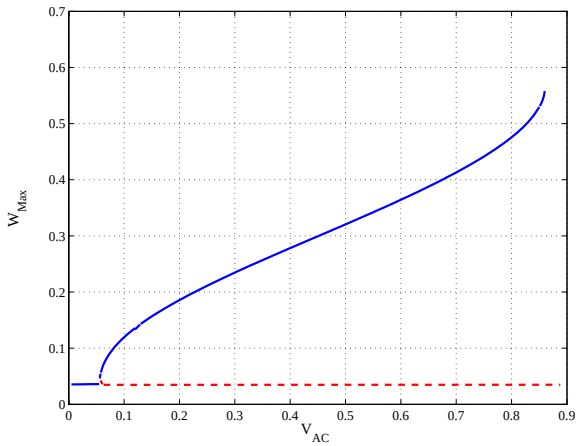

Figure 8.12: Force-response curve exhibiting dynamic pull-in when $Q = 1000$ and $\Omega = 47.85$.

Chapter 9

Summary, Conclusions, and Future Work

In this chapter, we summarize the dissertation and present concluding remarks and recommendations for the future work.

9.1 Summary and Conclusions

9.1.1 A Model of Microplates under the Effect of Squeeze-Film Damping and Small Electrostatic Forces

We presented a new approach to the modeling and simulation of flexible microstructures under the effect of squeeze-film damping. We applied perturbation methods to the compressible Reynolds equation to express the pressure distribution in terms of the structural mode shape, which was substituted into a plate equation. The resulting equation was solved using a finite-element method for the natural frequencies, the structural mode shapes, the corresponding pressure distribution, and the quality factors. The calculated quality factors were found to be in good agreement with experimental data.

The analytical expressions for the pressure reduce the simulation time for this class of MEMS devices. The analytical expressions can be implemented in a variety

of numerical schemes, such as finite-difference methods, finite-element methods, and reduced-order models, to simulate accurately the coupled structural-fluidic problem and to predict damping. The new approach however is limited to devices with high natural frequencies and squeeze numbers. This approach needs to be extended to a broader class of MEMS devices.

9.1.2 A Model of Microplates under the Effect of Squeeze-Film Damping and Large Electrostatic Forces

We presented a model for the dynamic behavior of microplates under the coupled effects of squeeze-film damping, electrostatic actuation, and mechanical forces. The model simulates the dynamics of microplates and predicts their quality factors under a wide range of gas pressures and applied electrostatic forces. The model presents a novel approach to the simulation of coupled-energy systems, which reduces the computational cost.

We investigated the effect of the pressure and the DC electrostatic forcing on the structural mode shapes, the pressure distributions, the natural frequencies, and the quality factors. The results show that the electrostatic force has more influence on the mode shapes and the natural frequencies than the encapsulation pressure. The quality factor, on the other hand, is strongly dependent on the encapsulation pressure. The results show a direct relation between the electrostatic force and the quality factor, which indicates that the use of a single value for the quality factor in modeling this class of devices for different DC loadings might lead to erroneous results.

9.1.3 A Model for Thermoelastic Damping in Microplates

We derived an analytical expression for the quality factors of microplates due to thermoelastic damping. We solved the heat equation for the thermal flux through the microplate thickness and utilized a perturbation method to derive an analytical expression for the quality factors of microplates with general boundary conditions under electrostatic loading and residual stresses in terms of their structural mode shapes. For the special case of no electrostatic and in-plane loadings, we derived a simple ana-

lytical expression for the quality factor, which is independent of the plate mode shape and natural frequency. Comparing the calculated quality factors of plates using our model to those obtained with beam models shows that beam models overestimate the quality factors. We found that the difference between predictions of the plate and beam models is proportional to the plate Poisson's ratio. The results show that the residual stresses decrease the effect of thermoelastic damping while the electrostatic forces amplify its effect.

9.1.4 Dynamics of MEMS Resonators under Primary-Resonance Excitation

We presented a dynamic analysis of MEMS resonators and proposed a novel approach to the design of low-voltage RF MEMS switches. We studied the dynamic pull-in instability and showed the need to take into account the static and dynamic stabilities in a device design. We showed that the dynamic pull-in phenomenon can be used to advantage to solve a challenging dilemma in the design of RF MEMS switches, namely the high deriving voltage requirement. Furthermore, our approach holds the promise of realizing fast-response switches by choosing the AC excitation amplitude to be higher than the pull-in limit while keeping the excitation frequency to be as close as possible to the resonance frequency. Experimental work is planned to investigate the feasibility of the new switch design.

9.1.5 Dynamics of MEMS Resonators under Secondary-Resonance Excitations

We simulated the dynamics of microbeams excited near half their fundamental natural frequencies (superharmonic excitation) and twice their fundamental natural frequencies (subharmonic excitation). For the superharmonic case, we presented results showing the effect of varying the DC bias, the damping, and the AC excitation amplitude on the frequency-response curves. We showed that the dynamic pull-in phenomenon can occur for a superharmonic excitation at an electric load much lower than that predicted based on static analysis. For the subharmonic case, we showed that all

frequency-response curves reach pull-in regardless of the magnitude of the AC forcing.

9.2 Recommendations for Future Work

The following is a list of recommendations and notes for future work.

- The singular perturbation approach, which is the basis of the analysis of flexible microstructures under the effect of squeeze-film damping, has to be extended and modified for beams and narrow plates. This is because the boundary layer in a beam becomes large compared to its width, and hence the singular perturbation analysis of microplates might not be applicable.

- The new approaches of simulating the effect of squeeze-film damping on microstructures need to be extended to include broader class of devices, such as perforated microstructures and torsional mirrors.

- The analysis of thermoelastic-damping in Chapter 6 needs to be extended to include thick beams and plates. This is particularly important because thick structures are being actively implemented in new MEMS and NEMS applications, in addition to the fact that thermoelastic damping of a structure depends directly on its thickness.

- Experimental work needs to be conducted to test the new proposed actuation method for RF MEMS switches, which is based on the dynamic pull-in phenomenon.

- Various structural elements (microbeams, membranes, microplates, and disks) need to be analyzed under the effect of coupled physics fields, such as squeeze-film damping, electrostatic forces, thermal loads, and residual stresses. Then, a Galerkin procedure or an assumed-modes approach need to be used to simulate the transient behavior, free vibration, and forced vibration of MEMS devices.

- A mode-synthesis approach is recommended to simulate the behavior of MEMS devices employing combinations of structural elements, such as microaccelerometer, which are composed of beams and plates.

References

1. Abdel-Rahman, E. M., Younis, M. I., and Nayfeh, A. H., "Characterization of the mechanical behavior of an electrically actuated microbeam," Journal of Micromechanics and Microengeering, Vol. 12, 2002, pp. 795–766.

2. Abdel-Rahman, E. M. and Nayfeh, A. H., "Secondary resonances of electrically actuated resonant microsensors, Vol. 13, 2003, pp. 491–501.

3. Abdel-Rahman, E. M., Younis, M. I., and Nayfeh, A. H., "A nonlinear reduced-order model for electrostatic MEMS," in Proceedings of the 19th Biennial Conference in Mechanical Vibration and Noise (VIB), Chicago, IL, 2003 (a), paper DETC2003/VIB-48517.

4. Abdel-Rahman, E. M., Nayfeh, A. H., and Younis, M. I., "Dynamics of an electrically actuated resonant microsensor," in Proceedings of the International Conference of MEMS, NANO and Smart Systems, Banff, Canada, 2003 (b), pp. 188–196.

5. Andrews, M., Harris, I., and Turner, G., "A comparison of squeeze-film theory with measurements on a microstructure," Sensors and Actuators A, Vol. 36, 1993, pp. 79–87.

6. Ananthasuresh, G. K., Gupta, R. K., and Senturia, S. D., "An approach to macromodeling of MEMS for nonlinear dynamic simulation," in Proceedings of the ASME International Conference of Mechanical Engneering Congress and Exposition (MEMS), Atlanta, GA, 1996, pp. 401–407.

7. Artz, B. E. and Cathey, L. W., "A finite element method for determining structural displacements resulting from electrostatic forces," in in Proceedings of the IEEE Solid-State Sensor and Actuator Workshop, Hilton Head Island, South Carolina, 1992, pp. 190–193.

8. Bao, M., Yang, H., Yin, H., and Sun, Y., "Energy transfer model for squeeze-film air damping in low vacuum," Journal of Micromechanics and Microengineering, Vol. 12, 2002, pp. 341–346.

9. Beskok, A. and Karniadakis, G. E., " A model for rarefied internal gas flows, " Journal of Fluid Mechanics, Vol. X, 1996, pp. 1-37.

10. Blech J. J., "On isothermal squeeze films," Journal of Lubrication Technology A, Vol. 105, 1983, pp. 615–620.

11. Boley, B. A. and Weiner, J. H., *Theory of Thermal Stresses,* Wiley, New York, 1960.

12. Burgdorfer, A., " The influence of the molecular mean free path on the performance of hydrodynamic gas lubricated bearing, " Journal of Basic Engineering, Vol. 81, 1959, pp. 94–99.

13. Chia, C. Y., *Nonlinear Analysis of Plates,* McGraw-Hill, New York, 1980.

14. Christian, R. G., "The theory of oscillating-vane vacuum gauges," Vacuum, Vol. 16, 1966, pp. 175–178.

15. Chu, P. B., Nelson, P. R., Tachiki, M. L., and Pister, K. S. J., "Dynamics of polysilicon parallel-plate electrostatic actuators," Sensors and Actuators A, Vol. 52, 1996, pp. 216–220.

16. Clark, J. R., Bannon, F. D. III, Ark-Chew, W., and Nguyen, C. T.-C., "Parallel-resonator HF micromechanical bandpass filters," in Proceedings of the Conference on Solid State Sensors and Actuators: TRANSDUCERS '97, Chicago, Illinois, Vol. 2, 1997, pp. 1161–1164.

17. Darling, R. B., Hivick, C. and, Xu, J., "Compact analytical modeling of squeeze film damping with arbitrary venting conditions using a Green's function approach," Sensors and Actuators A, Vol. 70, 1998, pp. 32–41.

18. Duemling, M., Modeling and characterization of nanoelectromechanical systems, Master Thesis, Virginia Polytechnic Institute and State University, Blacksburg, Virginia, 2002.

19. Duwel, A., Gorman, J., Weinstein, M., Borenstein, J., and Ward, P., "Experimental study of thermoelastic damping in MEMS gyros," Sensors and Actuators A, Vol. 103, 2003, pp. 70–75.

20. Elwespoek, M. and Wiegerink R., *Mechanical Microsensors* Springer, Berlin, 2001.

21. Evoy, S., Oikhovets, A., Sekaric, L., Parpia, J. M., Craighead, H. G., and Carr, D. W., "Temperature-dependent internal friction in silicon nanoelectromechanical systems," Applied Physics Letter, Vol. 77, 2000, pp. 2397–2399

22. Fukui, S. and Kaneko, R., "Analysis of ultra-thin gas film lubrication based on linearized Boltzman equation: first report- derivation of a generalized lubrication equation including thermal creep flow," Journal of Tribology, Vol. 253-262, 1988, pp. 299–303.

23. Gillbert, J. R., Legtenberg, R., and Senturia, S. D., "3D coupled electro-mechanics for MEMS: applications of CoSolve-EM," in Proceedings of the IEEE Micro Electro Mechanical Systems, MEMS '95, 1995, pp. 122–127.

24. Gui, C., Legtenberg, R., Elwenspoek, M., and Fluitman, J. H., "Q-factor dependence of one-port encapsulated polysilicon resonator on reactive sealing pressure," Journal of Micromechanics and Microengineering, Vol. 5, 1995, pp. 183–185.

25. Gui, C., Legrenberg, R., Tilmans, H. A., Fluitman, J. H. J., and Elwenspoek,

M., "Nonlinearity and hysteresis of resonant strain gauges," Journal of Microelectromechanical Systems, Vol. 7, 1998, pp. 122–127.

26. Gupta, M. C, *Statistical Thermodynamics,* Wiley, New Delhi, 1990.

27. Harmrock, B. J., *Fundamentals of Fluid Film Lubrication,* McGraw-Hill, New York, 1994.

28. Hung, E. S. and Senturia, S. D., "Generating efficient dynamical models for microelectromechanical systems from a few finite-element simulations runs," Journal of Microelectromechanical Systems, Vol. 8, 1999, pp. 280–289.

29. Jin, Z. and Wang, Y., "Electrostatic resonator with second superharmonic resonance," Sensors and Actuators A, Vol. 64, 1998, pp. 273–279.

30. Kàdàr, Z., Kindt, W., Bossche, A., and Mollinger, J., "Quality factor of torsional resonators in the low-pressure region," Sensors and Actuators A, Vol. 53, 1996, pp. 299–303.

31. Khonsari, M. M. and Booser, E. R., *Applied Tribology.* Wiley, New York, 2001.

32. Krylov, S. and Maimon, R., "Pull-in dynamics of an elastic beam actuated by distributed electrostatic force," in Proceedings of the 19th Biennial Conference in Mechanical Vibration and Noise (VIB), Chicago, IL, 2003, paper DETC2003/VIB-48518.

33. Legtenberg, R. and Tilmans, H. A., "Electrostatically driven vacuum-encapsulated polysilicon resonators. Part I. Design and fabrication," Sensors and Actuators A, Vol. 45, 1994, pp. 57–66.

34. Leissa, A. W., *Vibration of Plates,* NASA, Washington DC, 1969.

35. Li, B., Wu, H., Zhu, C., and Liu, J., "The theoretical analysis on damping characteristics of resonant microbeam in vacuum," Sensors and Actuators A, Vol. 77, 1999, pp. 191–194.

36. Li, G. and Hughes, H., "Review of viscous damping in micro-machined structures," in Proceedings of SPIE in micromachined devices and components VI, Bellingham, Washington, Vol. 4176, 2000, pp. 30–46.

37. Lifshitz, R. and Roukes, M. L., "Thermoelastic damping in micro- and nanomechanical systems," Physical Review B, Vol. 61, 2000, pp. 5600–5609.

38. Mccarthy, B., Adams, G., McGruer, N., and Potter, D., "A dynamic model, including contact bounce of an electrostatically actuated microswitch," Journal of Microelectromechanical Systems, Vol. 11, 2002, pp. 276–283.

39. Nayfeh, A. H., and Mook, D., *Nonlinear Oscillations,* Wiley, New York, 1979.

40. Nayfeh, A. H., *Introduction to Perturbation Techniques,* Wiley, New York, 1981.

41. Nayfeh, A. H., and Sanchez, N. E., "Chaos and dynamic instability in the rolling motion of ships," in Proceedings of the 17th Symposium on Naval Hydrodynamics, Hague, Netherlands, 1988, pp. 617–631.

42. Nayfeh, A. H., and Balachandran, B., *Applied Nonlinear Dynamics,* Wiley, New York, 1995.

43. Nayfeh, A. H., *Nonlinear Interactions,* Wiley, New York, 2000.

44. Nayfeh, A. H. and Younis, M. I., "A new approach to the modeling and simulation of flexible microstructures under the effect of squeeze-film damping," Journal of Micromechanics and Microengineering, Vol. 14, 2004, pp. 170–181.

45. Newell, W. E., "Miniaturization of tuning forks," Science, Vol. 161, 1968, pp. 1320–1326.

46. Pan, F., Kubby, J., Peeters, E., Tran, A. T., and Mukherjee, S., "Squeeze film damping effect on the dynamic response of a MEMS torsion mirror," Journal of Micromechanics and Microengineering, Vol. 8, 1998, pp. 200–208.

47. Randall, R. H., Rose, F. C., and Zener, C., "Intercrystalline thermal currents as a source of internal friction," Physical Review, Vol. 56, 1939, pp. 343–348.

48. Reddy, J. N., *An Introduction to the Finite Element Mehtod,* McGraw-Hill, New York, 1993.

49. Reddy, J. N., *Theory and Analysis of Elastic Plates,* Taylor and Francis, Philadelphia, 1999.

50. Reuther, H. M., Weinmann, M., Fischer, M., Münch, W., and Abumus, F., "Modeling electrostatically delectable microstructures and air damping effects," Sensors and Materials, Vol. 8, 1996, pp. 251–269.

51. Roszhart, T. V., "The effect of thermoelastic internal friction on the Q of micromachined silicon resonators," in Proceedings of the IEEE technical Digest of Solid-State Sensors and Actuators Workshop, Hilton Head, South Carolina, 1990, pp. 13–16.

52. Saif, M. T. A., Alaca, E. B., and Sehitoglu, H., "Analytical modeling of electrostatic membrane actuator for micro pumps," Journal of Microelectromechanical Systems, Vol. 8, 1999, pp. 335–345.

53. Seidel, H., Riedel, R., Kolbeck, Mück, G., Kupke, W., and Königer, M., "Capacitive silicon accelerometer with highly symmetric design," Sensors and Actuators A, Vol. 23, 1990, pp. 312–315.

54. Senturia, S. D., Azuru, N., and White, J., "Simulating the behavior of MEMS devices: Computational methods and needs," in Proceedings of the IEEE Computational Science and Engineering, Vol. 4, 1997, pp. 30–43.

55. Senturia, S. D., *Microsystem Design,* Boston, Kulwer Academic Publishers, 2000.

56. Schrag, G. and Wachutka, G., "Physically based modelling of squeeze film damping by mixed-level system simulation," Sensors and Actuators A, Vol. 97, 2002, pp. 193–200.

57. Starr, J. B., "Squeeze-film damping in solid-state accelerometers," in Proceeding of the IEEE Solid-State Sensor and Actuator Workshop, Hilton Head Island, South Carolina, 1990, pp. 44–47.

58. Tilmans, H. A., Elwespoek, M., and Fluitman, J. H., "Micro resonant force gauges," Sensors and Actuators A, Vol. 30, 1992, pp. 35–53.

59. Tilmans, H. A. and Legtenberg, R., "Electrostatically driven vacuum-encapsulated polysilicon resonators. Part II. Theory and performance," Sensors and Actuators A, Vol. 45, 1994, pp. 67–84.

60. Tilmans, H. A., Raedt, W. D., and Beyne, E., "MEMS for wireless communications: 'from RF-MEMS components to RF-MEMS-Sip', " Journal of Micromechanics and Microengineering, Vol. 13, 2003, pp. 139–163.

61. Timoshenko, S. P. and Woinowsky-Krieger, S., *Theory of Plates and Shells,* McGraw-Hill, New York, 1970.

62. Varadan, V. M., Vinoy, K. J., and Jose, K. A., *RF MEMS And Their Applications,* New York, Wiley, 2003.

63. Veijola, T., Kuisma, H., Lahdenperä, J., and Ryhänen, T., "Equivalent-circuit model of the squeezed gas film in a silicon accelerometer," Sensors and Actuators A, Vol. 48, 1995, pp. 239–248.

64. Veijola, T., Kuisma, H., and Lahdenpera, J., "Model for gas film damping in a silicon accelerometer," in Proceeding of the International Conference on Solid State Sensors and Actuators, TRANSDUCERS '97, Chicago, Illinois, Vol. 2, 1997, pp. 1097–1100.

65. Veijola, T., Ruokonen, K., and Tittonen, I., "Compact model for the squeezed-film damping including the open border effects," in Proceeding of the Forth Conference on Modelling and Simulation of Microsystems, MSM'01, Hilton Head Island, South Carolina, 2001, pp. 76–79.

66. Vemuri, S., Fedder, G. K., and Mukherjee, T., "Low-order squeeze film model for simulation of MEMS devices," in Proceeding of the Third Conference on Modelling and Simulation of Microsystems, MSM'00, San Diego, 2000, pp. 205–208.

67. Wachutka, G., "Coupled-field modeling of microdevices and microsystems," in Proceeding of the International Conference on Simulation of Semiconductor Processes and Devices, SISPAD 2002, Germany, 2002, pp. 9–14.

68. Zhao, X., Abdel-Rahman, E. M., and Nayfeh, A. H., "A reduced-order model for electrically actuated microplates," Journal of Micromechanics and Microengineering, Vol. 14, 2004, pp. 900–906.

69. Yang, Y. J., Gretillat, M. A., and Senturia, S. D., "Effect of air damping on the dynamics of nonuniform deformations of microstructures," International Conference on Solid State Sensors and Actuators, TRANSDUCERS '97, Chicago, Illinois, Vol. 2, 1997, pp. 1093–1096.

70. Yang, Y. J., *Squeeze-film damping for MEMS structures*, Master Thesis, Massachusetts Institute of Technology, Boston, Massachusetts, 1998.

71. Younis, M. I., *Investigation of the Mechanical Behavior of Microbeam-based MEMS Devices,* Master Thesis, Virginia Polytechnic Institute and State University, Blacksburg, Virginia, 2001.

72. Younis, M. I., Abdel-Rahman, E. M., and Nayfeh, A. H., "Static and dynamic behavior of an electrically excited resonant microbeam," in Proceeding of the 43rd AIAA Structures, Structural Dynamics, and Materials Conference, Denver, Colorado, 2002, AIAA Paper 2002-1305.

73. Younis, M. I., Abdel-Rahman, E. M., and Nayfeh, A. H., "A Reduced-order model for electrically actuated microbeam-based MEMS," Journal of Microelectromechanical Systems, Vol. 12, 2003, pp. 672–680.

74. Younis, M. I. and Nayfeh, A. H., "A study of the nonlinear response of a resonant microbeam to an electric actuation," Nonlinear Dynamics, Vol. 31, 2003, pp. 91–117.

75. Zener, C., "Internal friction in solids: I. Theory of internal friction in reeds," Physical Review, Vol. 52, 1937, pp. 230–235.

76. Zienkiewicz, O. C. and Taylor, R. L., *The Finite Element Method, Vol. 2: Nonlinear Problems,* McGraw-Hill, New York, 1991.

77. Zook, J. D., Burns, D. W., Guckel, H., Sniegowski, J. J., Engelstad, R. L., and Feng, Z., "Characteristics of polysilicon resonant microbeams," Sensors and Actuators A, Vol. 35, 1992, pp. 290–294.

Vita

Mohammad Ibrahim Younis received a B.S. in Mechanical Engineering (with honors) from Jordan University of Science and Technology, Irbid, Jordan, in 1999, and M.S. and Ph.D. degrees in Engineering Mechanics in 2001 and 2004 from Virginia Tech. Mohammad Younis worked at a private company as a design engineer in the field of pumps and water sector in the period from Jun-December, 1999. In January 2000, he joined the Department of Mechanical Engineering at King Fahad University of Petroleum and Minerals (KFUPM), Dhahran, Saudi Arabia, where he worked as a teaching and research assistant. In August 2000, he joined the Department of Engineering Science and Mechanics at Virginia Tech. Henceforth; he has been working under the supervision of Professor Ali Nayfeh in the areas of nonlinear dynamics and vibrations, MEMS, their modeling, characterization, and optimization.

Mohammad Younis is the recipient of the Paul E. Torgersen Graduate Research Excellence Award of the College of Engineering at Virginia Tech, 2002. He is a member of the American Society of Mechanical Engineers (ASME), the Jordan Engineers Association, and the Outstanding Student Honor Society (highest honor). His research interests are in MEMS; linear/nonlinear dynamics and vibrations; structural dynamics, and perturbation methods.